Available online at www.sciencedirect.com
ScienceDirect
Icarus 184 (2006) 121–157
ICARUS
www.elsevier.com/locate/icarus

Detection and discrimination of sulfate minerals using reflectance spectroscopy

Edward A. Cloutis [a,*], Frank C. Hawthorne [b], Stanley A. Mertzman [c], Katherine Krenn [a], Michael A. Craig [a], Dionne Marcino [a], Michelle Methot [a], Johnathon Strong [a], John F. Mustard [d], Diana L. Blaney [e], James F. Bell III [f], Faith Vilas [g]

[a] *Department of Geography, University of Winnipeg, 515 Portage Avenue, Winnipeg, MB, R3B 2E9, Canada*
[b] *Department of Geological Sciences, 335 Wallace Building, University of Manitoba, Winnipeg, MB, R3T 2N2, Canada*
[c] *Department of Geosciences, Franklin and Marshall College, Lancaster, PA 17604-3003, USA*
[d] *Department of Geological Sciences, Box 1846, Brown University, Providence, RI 02912, USA*
[e] *Jet Propulsion Laboratory, 4800 Oak Grove Drive, MS183-501, Pasadena, CA 91009, USA*
[f] *Department of Astronomy, Cornell University, 402 Space Sciences Building, Ithaca, NY 14853-6801, USA*
[g] *NASA Johnson Space Center, 2101 NASA Parkway, Code SR, Houston, TX 77058-3696, USA*

Received 8 April 2005; revised 29 March 2006

Available online 24 May 2006

Abstract

A suite of sulfate minerals were characterized spectrally, compositionally, and structurally in order to develop spectral reflectance–compositional–structural relations for this group of minerals. Sulfates exhibit diverse spectral properties, and absorption-band assignments have been developed for the 0.3–26 μm range. Sulfate absorption features can be related to the presence of transition elements, OH, H_2O, and SO_4 groups. The number, wavelength position, and intensity of these bands are a function of both composition and structure. Cation substitutions can affect the wavelength positions of all major absorption bands. Hydroxo-bridged Fe^{3+} results in absorption bands in the 0.43, 0.5, and 0.9 μm regions, while the presence of Fe^{2+} results in absorption features in the 0.9–1.2 μm interval. Fundamental S–O bending and stretching vibration absorption bands occur in the 8–10, 13–18, and 19–24 μm regions (1000–1250, 550–770, and 420–530 cm^{-1}). The most intense combinations and overtones of these fundamentals are found in the 4–5 μm (2000–2500 cm^{-1}) region. Absorption features seen in the 1.7–1.85 μm interval are attributable to H–O–H/O–H bending and translation/rotation combinations, while bands in the 2.1–2.7 μm regions can be attributed to H_2O- and OH-combinations as well as overtones of S–O bending fundamentals. OH- and H_2O-bearing sulfate spectra are fundamentally different from each other at wavelengths below ~6 μm. Changes in H_2O/OH content can shift S–O band positions due to change in bond lengths and structural rearrangement. Differences in absorption band wavelength positions enable discrimination of all the sulfate minerals used in this study in a number of wavelength intervals. Of the major absorption band regions, the 4–5 μm region seems best for identifying and discriminating sulfates in the presence of other major rock-forming minerals.

Keywords: Asteroids, composition; Europa; Mars, surface; Meteorites; Mineralogy; Spectroscopy

1. Introduction

Sulfates are important minerals for understanding the geologic and climatic evolution of a number of planetary bodies, because many of them form only under restricted conditions and remain stable over a narrow range of environmental conditions. Therefore, an ability to discriminate different sulfate minerals can provide important insights into the geologic and climatic history of sulfate-bearing targets (e.g., Buckby et al., 2003; Jerz and Rimstidt, 2003; Murad and Rojík, 2003; Burt et al., 2004; Feldman et al., 2004; Vaniman et al., 2004a). We have systematically examined the relations between spectral reflectance, composition, and structure of an extensive suite of sulfate minerals, with an emphasis on iron-bearing species, in

* Corresponding author. Fax: +1 (204) 774 4134.
E-mail address: e.cloutis@uwinnipeg.ca (E.A. Cloutis).

0019-1035/$ – see front matter
doi:10.1016/j.icarus.2006.04.003

order to determine the extent to which reflectance spectroscopy can be used to detect the presence of sulfate minerals and identify specific species.

While the spectroscopic properties of some sulfates have been examined by a number of investigators, a comprehensive examination of the relations between spectral variations, composition, and structure across a wide wavelength range is lacking. Such an approach is necessary if remote sensing identification of specific sulfate minerals is to be realized. Sulfates appear to be widely present on a number of Solar System bodies.

A number of lines of evidence indicate that sulfates occur widely on the surface of Mars. Sulfur was detected in martian surface fines by the Viking (Baird et al., 1976; Clark et al., 1982) and Pathfinder landers (McSween et al., 1999), and the Mars Exploration Rovers (Morris et al., 2004), and is widely presumed to be present as sulfates, perhaps a sulfate cement (e.g., Baird et al., 1976; McSween and Keil, 2000), as sulfate cementation is commonly seen in deposits resulting from terrestrial weathering of sulfide precursors (e.g., Jeong and Lee, 2003). Interstitial gypsum and anhydrite (Bridges and Grady, 1999, 2000; Pauli and Vicenzi, 2004), as well as Mg-sulfates (Wentworth et al., 2002), and possibly Fe-sulfates (Rao et al., 2004), have been directly detected in martian meteorites. In some of these meteorites, the specific sulfate species have not been determined (Gooding et al., 1988; Sawyer et al., 2000).

Data from the Mars Exploration Rovers, including Mössbauer, mini-TES, and APXS data, suggest that sulfates are present at both the Gusev crater and Meridiani sites (Bishop et al., 2005a; Lane et al., 2004; Klingelhöfer et al., 2004). Earth-based telescopic observations have attributed an absorption feature near 4.5 μm to an, as yet, unidentified sulfate mineral (Blaney and McCord, 1995; Blaney, 2001). Other Earth-based telescopic spectra of Mars suggest the presence of low symmetry sulfates or bisulfates, on the basis of absorption features located near 8.7 μm (1150 cm^{-1}) and 9.8 μm (1020 cm^{-1}) (Pollack et al., 1990). An absorption feature near 8.93 μm (1120 cm^{-1}) in Mars Global Surveyor TES data is correlated with areas of high sulfur abundance (Gendrin and Mustard, 2004). Bandfield (2002) tentatively identified a few areas in Acidalia that may contain sulfate minerals (type unknown but probably a Ca-sulfate) just above the detection limit (∼10%) using TES data. The Omega instrument on Mars Express has detected a number of sulfate species across some portions of Mars (Bibring et al., 2005; Gendrin et al., 2005), in particular kieserite, gypsum, and an as yet unconstrained polyhydrated sulfate (Arvidson et al., 2005; Gendrin et al., 2005; Langevin et al., 2005).

Martian sulfate minerals have been modeled as resulting from a number of mechanisms, including: progressive evaporation of acidic brines (Clark and Van Hart, 1981; Bridges and Grady, 2000); basalt–water interactions under martian atmospheric conditions (Bullock et al., 2004); aqueous eruption (Gaidos and Marion, 2003); hydrothermal and epithermal activity (Newsom et al., 1999; Bishop et al., 2005b; Hurowitz et al., 2005); acidic groundwater alteration (Burns, 1987; Burns and Fisher, 1990); impact-generated weathering (Knauth and Burt, 2004); soil–atmosphere interactions (Lammer et al., 2003; Tosca et al., 2004); and interaction of volcanic aerosols with surface materials (Settle, 1979). The source of the sulfur is widely believed to be volcanic aerosols or sulfides in basaltic rocks (Burns, 1992; Newsom et al., 1999). Weathering models and terrestrial analogues suggest that the alteration products of basalts on Mars would be largely composed of calcium and magnesium sulfates (e.g., Banin et al., 1997), similar to the sulfates identified in martian meteorites and from orbital data (e.g., Arvidson et al., 2005; Gendrin et al., 2005; Langevin et al., 2005). The presence of sulfates on Mars would also likely preclude the formation of contemporaneous carbonates (He and Morse, 1993; Lane et al., 2004).

In terms of thermodynamic stability, simple anhydrous or low water content iron sulfates, if present, are expected to be stable under current martian surface conditions (Gooding, 1978; Marion et al., 2003; Bonello et al., 2005; King et al., 2005; Marion and Kargel, 2005; Navrotsky et al., 2005; Tosca et al., 2005), although laboratory studies of sulfate stability under current martian and other planetary surface conditions are sparse (e.g., Mukhin et al., 1996; Forray et al., 2004; Vaniman et al., 2004b; Hasenmueller and Bish, 2005; Hogenboom et al., 2005; Jänchen et al., 2005; Moore et al., 2005; Vaniman et al., 2005). However, some photodecomposition of sulfates is expected under current martian surface conditions (Mukhin et al., 1996). Laboratory experiments and thermodynamic calculations suggest that chemical weathering and oxidation of iron from either iron sulfides or iron oxides will proceed under a wide range of martian surface conditions (Burns, 1988, 1993a; Burns and Fisher, 1993; Arlauckas et al., 2004), and will result in the production of either ferric or ferrous iron-bearing sulfates (Gooding, 1978; Burns, 1988, 1993a; Burns and Fisher, 1990, 1993; Lammer et al., 2003; Tosca et al., 2004). Experimental hydrothermal and lower-temperature alteration of terrestrial basalts and Mars analogs, under a variety of experimental conditions including CO_2-saturated aqueous fluids, normally result in the production of sulfate-bearing phases, even in short-duration experiments (Burns and Fisher, 1990; Moore and Bullock, 1999; Baker et al., 2000; Bullock et al., 2004; Tosca et al., 2004). Experimental weathering of altered and unaltered terrestrial volcanic tephra, using a variety of acidic solutions and vapors, also results in formation of sulfate minerals, precipitated largely as crusts (Banin et al., 1997; Golden et al., 2004). Natural terrestrial chemical weathering of rocks in cold deserts can also result in surficial/near-surface concentrations of sulfates (Berkley, 1981; Gibson et al., 1983; Burns and Fisher, 1990; Dickinson and Rosen, 2003).

Ca-, Mg-, and Na-bearing sulfates (gypsum, bloedite, epsomite) have been identified in CI carbonaceous chondrite meteorites (Burgess et al., 1991) as vein fillings and as isolated grains (Brearley and Jones, 1998). Ca-bearing sulfates have also been detected as vein filling (Brearley, 1993) and as alteration products in calcium–aluminum inclusions (Brearley and Jones, 1998) in CM chondrites. Telescopic spectra of a number of C-, P-, and G-class asteroids exhibit an absorption feature near 0.43 μm, which has been attributed to an Fe^{3+} spin–forbidden crystal field transition (Vilas et al., 1993); candidate minerals

for this feature include jarosite, as well as serpentine and chlorite.

Absorption features in Galileo NIMS spectra of Europa have been attributed to the presence of some form of heavily hydrated magnesium and/or sodium sulfates (McCord et al., 1999). Laboratory studies of the spectral properties and stabilities of candidate sulfates are ongoing to better constrain Europa's surface composition (McCord et al., 2001; Chou and Seal, 2003; Dalton, 2003; Dalton et al., 2005).

Iron sulfates are important terrestrial minerals. They are often indicative of acidic mine water pollution, and determining the specific species that are present and mapping their areal extent can help to delineate the severity of this pollution (e.g., Nordstrom et al., 2000). Variations in the areal extent of different iron sulfates can be used to reconstruct changes in acidity of groundwater flow (Alpers and Blowes, 1994). Naturally occurring surficial deposits of iron sulfates are also a useful tool in mineral exploration because they may be indicative of subsurface mineral deposits of potential economic importance (Blain and Andrew, 1977; Nickel and Daniels, 1985). The types of iron-bearing sulfate minerals that form terrestrially (due to oxidative weathering of exposed sulfides) are sensitive to pH, Eh, relative humidity, oxygen activity, microbial activity, and host media (Brady et al., 1986; Bigham et al., 1990, 1992, 1996; Alpers and Blowes, 1994; Singh et al., 1999; Garcia-Gonzalez et al., 2000; Kawano and Tomita, 2001; Buckby et al., 2003; Jerz and Rimstidt, 2003; Bishop et al., 2005a; Vaniman et al., 2004a; Greenwood et al., 2005), and can be used to constrain the conditions prevalent at the time of their formation (Murad and Rojík, 2003).

Iron-free sulfate minerals can also be related to specific conditions of formation. For example, formation of gypsum is commonly associated with arid conditions and high evaporation rates, although it can also form diagenetically via oxidation of sulfides by calcium-rich oxidizing ground water (Bain, 1990), and as a result of biomineralization (Thompson and Ferris, 1990). In contrast to iron sulfates, aluminum sulfates (alunite group) can form in a wide range of metamorphic, sedimentary, and igneous environments. In some cases, the sulfates can provide more petrogenetic information than the rock-forming minerals of a host rock (Hladky and Slansky, 1981; Dill, 2001).

2. Structural properties of sulfate minerals

There are over 350 natural sulfate minerals (Hawthorne et al., 2000). In order to provide a basis for spectral classification and comparison, we have adopted the structural and formulaic classification system of Hawthorne et al. (2000). For the ensuing discussion, M refers to a metal cation, octahedra generally involve an MO_6 or $M(H_2O)_6$ cluster, and tetrahedra involve an SO_4 cluster. Round and curly brackets denote a polyhedron or group, e.g., (SO_4), while square brackets denote linked polyhedra, e.g., $[M(SO_4)_2O_4]$. Ideal formulas of the sulfates included in this study are provided in Table 1. This approach to describing ideal sulfate compositions provides discrimination between polyhedra and groups versus linked polyhedra. These formulas can be "collapsed" into more familiar and compact standard formulaic representations. As an example, the fact that hexahydrite consists of unconnected SO_4 tetrahedra and $Mg + 6H_2O$ octahedra is better reflected in the currently used representation—$\{Mg(H_2O)_6\}(SO_4)$ than in the "standard" representation—$MgSO_4{\cdot}6H_2O$.

2.1. Structures with unconnected SO_4 groups

In this group, sulfate tetrahedra (SO_4) and (MO_6) octahedra are linked together by hydrogen bonding; this involves linkages from donor ligands of the octahedra to acceptor ligands of tetrahedra, together with weak hydrogen bonding between ligands of different octahedra. This group includes hexahydrite and melanterite, the latter containing additional H_2O beyond that required for linkage of (MO_6) octahedra and (SO_4) tetrahedra.

2.2. Structures with finite clusters of polyhedra

Minerals in this group include romerite, pickeringite, apjohnite, rozenite, and coquimbite/paracoquimbite. Romerite, pickeringite, and apjohnite are based on an $[M(SO_4)_2O_4]$ cluster. In addition to this cluster, romerite contains isolated $\{Fe^{2+}(H_2O)_6\}$ octahedra, and these elements are linked by hydrogen bonding both between unconnected octahedra and tetrahedra, and between octahedra and tetrahedra of the same $[M(SO_4)_2O_4]$ cluster. Rozenite is based on an $[Fe_2^{2+}(SO_4)_2O_8]$ cluster linked by hydrogen bonds both within and between adjacent clusters. Coquimbite and its polytype, paracoquimbite, are based on an $[Fe_3^{3+}(SO_4)_6]$ cluster, isolated $\{Fe^{3+}(H_2O)_6\}$ octahedra, and (H_2O) groups. The $\{Fe^{3+}(H_2O)_6\}$ octahedra are connected into sheets by hydrogen bonding.

2.3. Structures with infinite chains

Minerals in this group include fibroferrite, sideronatrite, botryogen, copiapite, ferricopiapite, and amarantite. In fibroferrite, the chain consists of $[MO_5]$ vertex-sharing octahedra. Adjacent chains link by both direct hydrogen bonding between chains and by a hydrogen-bonding network involving (H_2O) groups not linked to any cations. Sideronatrite has a more complex linkage between octahedra and tetrahedra, and shows considerable disorder in terms of the relations between adjacent chains. Botryogen is based on an $[M(SO_4)_2O]$ chain which links to an (MgO_6) octahedron through one of its vertices. Interchain linkage involves only hydrogen bonding. Copiapite and ferricopiapite have corner-sharing $[M_2(SO_4)_2O_7]$ clusters linked through additional tetrahedra to form infinite $[M_2(SO_4)_3O_5]$ chains. The chains are linked together by hydrogen bonds involving unconnected $\{M^{2+}(H_2O)\}$ octahedra and interstitial (H_2O) groups. The detailed structure of ferricopiapite, involving Fe^{3+} rather than an M^{2+} cation in the octahedra has not been fully resolved (Hawthorne et al., 2000). The structure of amarantite is based on a hierarchy of structural units: two octahedra share an edge to form an $[M_2O_{10}]$ dimer; two additional octahedra link to either end of the shared edges

Table 1
Ideal formulas, H_2O/SO_4 and OH/SO_4 ratios of the sulfates used in this study (they have been sorted on the basis of increasing H_2O/SO_4 or OH/SO_4 ratios)

Mineral	Formula	H_2O/SO_4[a]	OH/SO_4[a]	H_2O[b]	OH[b]
H_2O- and OH-free					
Anhydrite[4]	$[CaSO_4]$	0	0	0	0
Anglesite[5]	$[Pb^{2+}(SO_4)]$	0	0	0	0
Barite[5]	$[Ba(SO_4)]$	0	0	0	0
OH-bearing					
Jarosite[4]	$K[Fe^{3+}_3(OH)_6(SO_4)_2]$	0	3	0	1
Natrojarosite[4]	$Na[Fe^{3+}_3(OH)_6(SO_4)_2]$	0	3	0	1
Alunite[4]	$K[Al_3(OH)_6(SO_4)_2]$	0	3	0	1
H_2O-bearing					
Kieserite[5]	$[Mg(SO_4)(H_2O)]$	1	0	1	0
Szomolnokite[5]	$[Fe^{2+}(SO_4)(H_2O)]$	1	0	1	0
Voltaite[5]	$K_2[Fe^{2+}_5Fe^{3+}_3(H_2O)_{12}(SO_4)_{12}][Al(H_2O)_6]$	1.5	0	2	0
Rhomboclase[4]	$(H_5O_2)[Fe^{3+}(H_2O)_2(SO_4)_2]$	2[c]	0	2[c]	0
Gypsum[4]	$[CaSO_4(H_2O)_2]$	2	0	1	0
Amarantite[3]	$[Fe^{3+}_2O(H_2O)_4(SO_4)_2](H_2O)_4$	3	0	2	0
Coquimbite[2]	$[Fe^{3+}_3(SO_4)_6(H_2O)_6]\{Fe^{3+}(H_2O)_6\}(H_2O)_6$	3	0	3	0
Romerite[2]	$[Fe^{3+}(SO_4)_2(H_2O)_4]_2[Fe^{2+}(H_2O)_6]$	3.5	0	2	0
Rozenite[2]	$[Fe^{2+}(SO_4)(H_2O)_4]$	4	0	1	0
Hexahydrite[1]	$\{Mg(H_2O)_6\}(SO_4)$	6	0	1	0
Melanterite[1]	$\{Fe^{2+}(H_2O)_6\}(SO_4)(H_2O)$	7	0	2	0
Pickeringite[2]	$[Mg(SO_4)(H_2O)_5]\{Al(H_2O)_6\}_2(SO_4)(H_2O)_5$	11	0	3	0
H_2O- and OH-bearing					
Hydronium jarosite[4]	$(H_3O)[Fe^{3+}_3(OH)_6(SO_4)_2]$	1[d]	3	1[d]	1
Sideronatrite[3]	$Na_2[Fe^{3+}(OH)(SO_4)_2](H_2O)_3$	1.5	0.5	1	1
Ferricopiapite[3]	$[Fe^{3+}_2(OH)(H_2O)_4(SO_4)_3]_2\{(Fe^{3+}_{0.67}\square_{0.33})(H_2O)_6\}(H_2O)_6$	3.3	0.3	3	1
Copiapite[3]	$[Fe^{3+}_2(OH)(H_2O)_4(SO_4)_3]_2\{Fe^{2+}(H_2O)_6\}(H_2O)_6$	3.3	0.3	3	1
Botryogen[3]	$[MgFe^{3+}(OH)(H_2O)_6(SO_4)_2](H_2O)$	3.5	0.5	2	1
Fibroferrite[3]	$[Fe^{3+}(OH)(H_2O)_2(SO_4)](H_2O)_3$	5	1	2	1

[a] Ratio of number of H_2O or OH groups to SO_4 groups in unit cell.
[b] Number of structurally distinct H_2O and/or OH groups in unit cell.
[c] Includes an H_2O_5 group (as a single H_2O).
[d] Includes an H_3O group (as a single H_2O).
[1] Structure consists of isolated SO_4 tetrahedra.
[2] Structure consists of finite clusters of polyhedra.
[3] Structure consists of infinite chains.
[4] Structure consists of infinite sheets.
[5] Structure consists of infinite framework.

of the dimer to form an $[M_4O_{20}]$ tetramer; two tetrahedra link between corners of adjacent octahedra and further link adjacent tetramers to form complex chains.

2.4. Structures with infinite sheets

Minerals in this group include alunite, jarosite, natrojarosite, hydronium jarosite, rhomboclase, anhydrite, and gypsum. The structures of alunite, jarosite, natrojarosite, and hydronium jarosite are based on octahedral–tetrahedral sheets. Corner-sharing octahedra form a six-membered ring. At the junction of three six-membered rings is a three-membered ring, and one set of the apical vertices of those three octahedra link to a tetrahedron. The sheets are held together by interstitial cations and hydrogen bonds. Rhomboclase consists of a more regular two-dimensional grid of alternating octahedra and tetrahedra. It has an extended hydrogen-bonding scheme involving interstitial $(H_5O_2)^+$ dimers. The structure of anhydrite ($CaSO_4$) is based on chains of alternating edge-sharing (SO_4) tetrahedra and (CaO_8) dodecahedra which are linked by edge sharing between adjacent (CaO_8) dodecahedra and by corner sharing between (CaO_8) dodecahedra and (SO_4) tetrahedra. The structure consists of sheets of edge-sharing chains. The structure of gypsum is similar and includes interlayer (H_2O) which is hydrogen bonded to tetrahedrally coordinated O atoms.

2.5. Structures with infinite frameworks

This structural group includes kieserite, szomolnokite, voltaite, barite, and anglesite. The $[M(SO_4)(H_2O)]$ framework structures of kieserite and szomolnokite consist of $[M(SO_4)O_3]$ chains that are cross-linked by corner sharing between octahedra and tetrahedra of adjacent chains. The structure of voltaite is a three-dimensional polymerization of complex tetrahedral–octahedral chains with K in the interstices. In barite, Ba is in [12]-coordination, forming irregular polyhedra that are linked

into a framework. Considering only the six-nearest O atoms, the Ba coordination is a distorted octahedron and the structure is built from chains of edge-sharing octahedra linked by (SO_4) groups into sheets. The sheets are linked into a framework by corner-sharing between (BaO_6) polyhedra and (SO_4) tetrahedra from adjacent sheets. Barite and anglesite have the same structure with Pb instead of Ba in anglesite. More detailed descriptions and structural representations can be found in Hawthorne et al. (2000).

3. Experimental procedure

A suite of 42 sulfate minerals was used in this study. It was augmented with spectra from the literature, in particular Crowley (1991), Crowley et al. (2003), Grove et al. (1992), Lane (2004), and the RELAB public archive (http://www.planetary.brown.edu/relab/rel_pub/). The samples were characterized spectrally, compositionally, and structurally in order to identify the major and minor phases present in the samples. Samples were gently crushed by hand in an alumina mortar and pestle and dry sieved to obtain <45 μm fractions. Impurities were removed through a combination of visual inspection with a binocular microscope and with a hand magnet during crushing. Splits of the homogenized samples were allocated for the spectral, compositional, and structural studies.

Reflectance spectra were measured at the NASA-supported multi-user RELAB spectrometer facility at Brown University. The spectra were measured at $i = 30°$ and $e = 0°$ in bidirectional mode relative to halon for the 0.3–2.6 μm region at 5 nm spectral resolution, and at $i = 30°$ and $e = 30°$ with 4 cm^{-1} spectral resolution using an on-axis biconical configuration relative to brushed gold for the 2.5–26 μm (390–4000 cm^{-1}) region. The 0.3–2.6 μm spectra were measured under ambient atmosphere. The 2.5–26 μm spectra were measured after purging the samples (removal of water and CO_2) for at least 5 h. The spectra were merged at 2.5 μm by multiplying the longer-wavelength spectrum by an appropriate correction factor calculated in the region of spectral overlap (2.5–2.6 μm). As a result, direct comparison of absorption bands attributable to water across the 2.5–2.6 μm divide are not fully warranted. Details of the RELAB facility and spectral acquisition procedures are given by Pieters (1983) and are available at the RELAB web site (http://www.planetary.brown.edu/relab/). Band minima wavelength positions were determined by fitting a third-order polynomial to 10–20 data points (if available) on either side of a visually determined minimum. Absorption band depths were calculated using Eq. (32) of Clark and Roush (1984).

The samples were characterized using X-ray fluorescence (XRF) for major elements (Mertzman, 2000). Ferrous iron was determined using a modification of the procedure outlined by Reichen and Fahey (1962). Ferric iron concentration was taken as the difference between total and ferrous iron. Volatile contents were determined by heating splits of the samples to 950 °C for one h and measuring the associated weight loss.

The samples were structurally characterized using X-ray diffraction (XRD) to ascertain the phases present in the samples and to verify the phases determined by XRF. XRD analytical procedures are described in Cloutis et al. (2004). Sample descriptions, compositions, and phases identified through integrated XRF and XRD analyses are provided in Table 2. The reflectance spectra of the various samples are provided in Figs. 1–3. The XRD and XRF data and ideal formulas were integrated to provide constraints on the purity of the samples and the identity and approximate abundances of any accessory minerals. Phase abundances are generally accurate to within ±10%.

Table 2
Composition of samples used in this study

Wt%	SPT107	SPT108	SPT109	SPT110	SPT111	SPT112	SPT113
SiO_2	0.01	1.70	6.09	0.00	27.74	6.70	0.01
TiO_2	0.01	0.03	0.08	0.00	0.07	0.14	0.02
Al_2O_3	0.00	0.32	2.56	0.10	0.84	2.17	0.42
FeO	0.11	0.14	0.98	12.04	10.01	0.15	0.18
Fe_2O_3	61.19	55.97	21.78	15.93	12.82	46.33	52.01
MnO	0.01	0.01	0.02	0.02	0.07	0.14	0.01
MgO	0.12	0.16	0.32	0.00	0.41	0.23	0.10
CaO	0.15	0.18	0.30	0.00	0.68	1.11	0.35
Na_2O	4.63	6.04	0.58	0.32	0.28	0.34	4.35
K_2O	1.47	0.80	0.39	0.00	0.61	0.65	1.09
P_2O_5	0.03	0.06	0.02	0.00	0.02	1.00	0.03
SO_3	27.87	28.64	37.90	40.04	33.90	21.86	32.76
OH/H_2O[1]	3.76	5.67	28.39	29.64	11.00	17.96	8.05
Total	99.36	99.72	99.41	99.43	99.56	98.78	99.38
ppm							
Sr	130	780	190	2	95	40	<2
Zr	20	25	82	8	50	125	15
V	63	61	66	4	65	210	75
Co	<2	<2	860			<2	<2
Cr	20	25	58	<2	35	50	15
Ni	<2	<2	225			40	<2
Rb	10	28	125			20	20
Cu				1730			
Pb				4815			
Zn				4315			
XRD[2]	90% Na 10% Go	90% Na 10% Qu	60% Fe 30% Me 10% Ka	60% Ro 20% Rh 20% Py	60% Vo 20% Ro 20% Qu	80% Am 15% He 5% Ka	90% Na 10% Co

Wt%	SPT114	SPT115	SPT116	SPT117	SPT118	SPT119	SPT120
SiO_2	0.00	0.25	0.03	4.56		0.56	65.52
TiO_2	0.01	0.06	0.01	0.05		0.02	0.25
Al_2O_3	0.00	0.04	0.07	2.73	6.50	4.63	1.51
FeO	0.21	0.14	0.19	0.00	0.22	0.08	0.36
Fe_2O_3	68.75	51.72	53.09	22.05	0.00	22.68	19.94
MnO	0.01	0.01	0.01	0.07		0.01	0.02
MgO	4.62	0.17	0.11	2.79	7.96	0.24	0.76
CaO	5.73	0.05	0.11	0.16		0.03	0.40
Na_2O	1.20	0.32	3.07	0.26		0.08	0.43
K_2O	1.21	11.97	6.68	0.14		0.36	0.06
P_2O_5	0.10	0.08	0.59	0.03		0.03	0.38
SO_3	25.26	31.95	32.50	39.95	43.05	46.19	5.13
OH/H_2O[1]	0.00[a]	2.25	2.96	26.90	28.06	24.92	5.01
Total	107.10	99.01	99.42	99.69		99.83	99.77
ppm							
Sr	515	<2	2640	18		<2	295
Zr	20	15	25	39		24	<2
V	60	75	75	100		67	1600
Co	<2	<2	<2	52		<2	<2
Cr	10	13	600	130		40	280

(*continued on next page*)

Table 2 (*continued*)

Wt%	SPT114	SPT115	SPT116	SPT117	SPT118	SPT119	SPT120
Ni	75	<2	<2	52		<2	240
Rb	15	120	220	13		25	<2
Cu							
Pb							
Zn							
XRD[2]	80% Ja 10% Go 10% He	100% Ja	100% Ja	95% Co 5% Ka	95% Pi 5% Ha	100% Cq	60% Qu 40% Hj

Wt%	SPT121	SPT122	SPT123	SPT124	SPT125	SPT126	SPT127
SiO_2	0.95	0.19		1.78	4.39		0.00
TiO_2	0.01	0.02		0.01	0.06		0.00
Al_2O_3	0.08	0.24		0.27	2.01		0.20
FeO	0.00	0.16	0.36	0.34		0.45	0.00
Fe_2O_3	34.73	29.42	19.87	22.22	27.01[b]	26.34	0.03
MnO	0.02	0.01		0.09	0.01		0.00
MgO	0.11	0.09	0.01	10.43	0.27	0.05	0.07
CaO	0.26	0.22		0.05	0.41		32.46
Na_2O	0.21	0.15		0.09	4.25		0.30
K_2O	0.04	0.01		0.01	1.69		0.00
P_2O_5	0.01	0.01		0.01	0.07		0.01
SO_3	35.38	42.73	41.99	35.83	33.16	44.27	46.55
OH/H_2O[1]	27.84	26.63	1.39	27.11	25.83	23.28	20.58
Total	99.64	99.88		98.24	99.16		100.20
ppm							
Sr	15	<2		<2	<5		200
Zr	29	15		18	15		9
V	72	69		56	90		<2
Co	<2	160		680			
Cr	48	25		2223	55		<2
Ni	<2	<2		13,020			
Rb	8	10		2			
Cu							
Pb							
Zn							
XRD[2]	70% Fi 30% Bu	70% Ro 30% Cq	100% Si	100% Bo	90% Fe 10% Ja	70% Cq 30% Pc	100% Gy

Wt%	SPT128	SPT129	SPT130	SPT131	SPT132	SPT133	SPT134
SiO_2	0.00	0.00		60.70	63.29	0.25	
TiO_2	0.00	0.00		0.52	0.35	0.01	
Al_2O_3	0.15	44.48		1.24	2.01	0.11	
FeO	0.00	0.03	25.54	2.67	0.14	0.00	8.56
Fe_2O_3	0.04	0.00	2.40	5.95	5.78	29.80	0.00
MnO	0.00	0.00		0.01	0.02	0.02	
MgO	0.06	0.04	0.01	0.39	0.25	0.18	
CaO	46.06	0.07	0.11	0.27	3.17	0.05	
Na_2O	0.78	0.27	0.02	0.21	0.33	0.18	
K_2O	0.00	14.05		0.04	0.15	0.01	
P_2O_5	0.02	0.45		0.06	0.03	0.01	
SO_3	37.38	35.88	32.26	14.31	15.65	41.82	42.72
OH/H_2O[1]	15.89	4.27	35.02	12.97	8.17	26.97	23.35
Total	100.38	99.54			99.34	99.41	
ppm							
Sr	700	3420		825	690	<2	
Zr	10	20		250	175	18	
V	4	135		55	48	55	
Co		<2		24	65	1405	
Cr	4	40		23	22	28	
Ni		8		44	36	25	
Rb		25		<2	17	9	
Cu							

(*continued in next column*)

Table 2 (*continued*)

Wt%	SPT128	SPT129	SPT130	SPT131	SPT132	SPT133	SPT134
Pb							
Zn							
XRD[2]	80% An 20% Gy	100% Al	70% Rz 30% Ml	50% Co 10% Cq 40% Qu	40% Cq 20% An 40% Qu	100% Fe	40% Ro 30% Cq 30% Sz

Wt%	SPT135	SPT136	SPT137	SPT138	SPT139	SPT140	SPT141
SiO_2		16.19	0.03			0.44	0.00
TiO_2		0.33	0.10			0.01	0.00
Al_2O_3		0.30	3.37			3.68	0.02
FeO		0.32	0.00			0.03	0.00
Fe_2O_3		37.87	33.12			1.05	0.26
MnO		0.01	0.00			0.10	0.01
MgO		1.01	0.18			1.95	8.22
CaO		4.57	0.06			0.09	0.03
Na_2O		7.43	0.62			0.25	7.39
K_2O		3.47	0.04			0.02	2.16
P_2O_5		0.09	0.04			0.02	0.01
SO_3		38.45	25.44				
OH/H_2O[1]		0.00[c]	46.23[d]	71.21[e]	74.66[e]	77.03[e]	46.55[e]
Total		110.04	109.23				
ppm							
Sr		10	10			80	30
Zr		50	45			35	25
V		87	10			55	30
Co		3	525			525	5
Cr		45	4			100	<5
Ni		13	125			1825	<2
Rb		190	<2			10	15
Cu			1450			2600	520
Pb							
Zn							
XRD[2]	60% Mc 30% Sz 10% Py	60% Si 20% Ja 10% Py 10% Qu	90% Pc 10% Ko	60% Co 40% Pc	100% Rh	90% Pi 10% Ap	80% Ki 20% Hl

Wt%	SPT142	SPT143	SPT144	SPT145	SPT146	SPT147	SPT148
SiO_2	1.87	0.00	29.52	0.00	0.00		
TiO_2	0.03	0.00	0.92	0.00	0.23		
Al_2O_3	9.66	0.04	10.12	0.00	0.23		
FeO	0.00	0.00	8.34	0.00	0.00		
Fe_2O_3	0.23	0.00	16.42	0.00	0.00		
MnO	0.11	0.01	0.03	0.00	0.00		
MgO	7.41	15.53	1.87	0.08	0.00		
CaO	0.24	0.29	1.39	0.03	0.27		
Na_2O	0.16	0.58	0.62	0.15	0.07		
K_2O	0.14	0.06	1.20	0.00	0.00		
P_2O_5	0.05	0.03	0.10	0.04	0.02		
SO_3			23.53	29.47	34.15		
OH/H_2O[1]	71.70[e]	38.11[e]	6.02	1.07	0.07		
Total			100.08				
ppm							
Sr	175	90	100	80	15920		
Zr	50	25	215	<5	75		
V	50	30	170	40	425		
Co	420	<2	45	20	<2		
Cr	80	15	75	<5	<2		
Ni	2330	<2	20	650	35		
Rb	13	<2	70	<5	7		
Cu	3050	600	1700	1600	190		

(*continued on next page*)

Table 2 (*continued*)

Wt%	SPT142	SPT143	SPT144	SPT145	SPT146	SPT147	SPT148
XRD[2]	70% Pi 30% Hx Am[f]	100% Hx Am[f]	60% Sz 10% Rz 10% Py 20% Ka	100% Ag	100% Ba	80% Ag 20% Ce	100% Ag

Abbreviations: Ag: anglesite; Al: alunite; Am: amarantite; An: anhydrite; Ap: apjohnite; Ba: barite; Bo: botryogen; Bu: butlerite; Ce: cerussite; Co: copiapite; Cq: coquimbite; Fe: ferricopiapite; Fi: fibroferrite; Go; goethite; Gy: gypsum; Ha: halotrichite; He: hematite; Hj: hydronium jarosite; Hl: halite; Hx: hexahydrite; Ja: jarosite; Ka: kaolinite or other layer lattice aluminosilicates; Ki: kieserite; Ko: kornelite; Mc: magnesiocopiapite; Me: metavoltine; Ml: melanterite; Na: natrojarosite; Pc: paracoquimbite; Pi: pickeringite; Py: pyrite; Qu: quartz; Rh: rhomboclase; Ro: romerite; Rz: rozenite; Si: sideronatrite; Sz: szomolnokite; Vo: voltaite.

Localities of samples: SPT107: Skouriatissa Mine, Cyprus (Smithsonian Institute National Museum of Natural History #104139-1); SPT108: Warner Mine, south of Host Springs, Mineral County, NV, USA (Smithsonian Institute National Museum of Natural History #95074-1); SPT109: Borate, San Bernardino County, CA, USA; SPT110: Sulfur Hole, near Borate, San Bernardino County, CA, USA; SPT111: Island Mountain Mine, Trinity County, CA, USA; SPT112: Yazd, Iran; SPT113: Sierra Gorda, Chile; SPT114: Laurium, Greece; SPT115: Arabia District, Pershing County, NV, USA; SPT116: Copiapa Jarosite Mine, Dona Ana County, NM, USA; SPT117 and SPT118: Alma Pyrite Mine, Leona Heights, Oakland, Alameda County, CA, USA; SPT119: Dexter #7 Mine, San Rafael Swell, UT, USA; SPT120: Rustler Mine, Tooele County, UT, USA; SPT121: Skouriatissa, Cyprus; SPT122: Alcaparrosa, Chile; SPT123: Capitol Reef National Monument, Wayne County, UT, USA; SPT124: Redington Mine, Knoxville, Napa County, CA, USA; SPT125: Sierra Gorda, Chile; SPT126: Alcaparrosa, Chile; SPT127: UT, USA; SPT128: unknown locality; SPT129: Marysvale, Piute County, UT, USA; SPT130: Oage Mine, Ominato, Aomoriken, Honshu, Japan; SPT131 and SPT132: Borate, San Bernardino County, CA, USA; SPT133: Alcaparrosa, Chile; SPT134: Island Mountain Mine, Trinity County, CA, USA; SPT135: Island Mountain Mine, Trinity County, CA, USA; SPT136: Sierra Gorda, Chile; SPT137 and SPT138: Coso Hot Spring, Inyo County, CA, USA; SPT139: Alcaparrosa, Chile; SPT140: Kelly Mine, Red Mountain, Randsburg Mining District, San Bernardino County, CA, USA; SPT141: Stassfurt, Saxony, Germany; SPT142: Salt Lake, Box Elder County, UT, USA; SPT143: Basque Lakes, near Ashcroft, BC, Canada; SPT144: Getchell Mine, near Golconda, Humboldt County, NV, USA; SPT145: Excepcion Mine, Villa Ahumada, Chihuahua, Mexico; SPT146: Castle Dome, Yuma County, AZ, USA; SPT147: Tsumeb, Namibia; SPT148: Italy (Smithsonian Institution National Museum of Natural History #163581).

[1] OH/H_2O taken as difference between total loss on ignition (after heating sample to 950 °C for 1 h) and SO_3 content.

[2] Crystalline phases detected by XRD.

[a] Measured loss on ignition was lower than SO_3 content; this suggests that some sulfur may be present as sulfides, but no sulfide phases were detected by XRD.

[b] All Fe reported as Fe_2O_3.

[c] SO_3 content is higher than loss on ignition; this is likely due to the presence of pyrite in the sample; total S content in this sample is 25.4 wt%.

[d] OH/H_2O content taken as difference between loss on ignition and SO_3 content.

[e] Loss on ignition after heating sample in air at 950 °C for 1 h (i.e., $SO_3 \pm OH \pm H_2O$).

[f] An unknown amount of an amorphous component also detected by XRD.

Changes in the hydration states of some of the samples may also have occurred in the course of this study. Storage conditions for the samples prior to their acquisition for this study are unknown. However once the samples were acquired, they were placed in airtight containers with minimal headspace. The samples were exposed to ambient atmosphere for, at most, a few hours in the course of sample preparation, crushing and sieving, and for the compositional, structural analyses, and spectral measurements. The resultant spectra are very similar to those measured by Crowley et al. (2003), who used different sample preparation, storage, and spectral measurement procedures, for sulfates common to both studies.

A few comments are in order for some of the samples used in this study. Fe^{3+}-bearing sulfates used in this study were fibroferrite, rhomboclase, amarantite, coquimbite, paracoquimbite, and ferricopiapite. Fibroferrite is the dominant phase in SPT121. Compositionally, this sample is close to the ideal formula, but with a lower $H_2O + OH$ content (27.8 vs 38.3 wt%). SPT139 is essentially pure rhomboclase and is subordinate to romerite in SPT110. Amarantite is the dominant sulfate in sample SPT112, which also contains hematite. Coquimbite and paracoquimbite are the dominant sulfates in SPT119, 126, 132, and 137 and are close to the ideal compositions. Ferricopiapite is the dominant sulfate in SPT109, 125, and 133. Compositionally, these samples contain less than the ideal amount of OH/H_2O but are otherwise consistent with ferricopiapite.

Samples containing both Fe^{3+} and additional cations include hydronium jarosite, botryogen, sideronatrite, jarosite, and natrojarosite. Hydronium jarosite is represented by sample SPT120, which also contains abundant quartz. Compositionally, this sample deviates from the ideal formula in terms of OH/H_3O content, even after accounting for the quartz; the reason for this is unclear. Botryogen is represented by sample SPT124. Compositionally, it is close to the ideal formula, but with a lower than expected OH/H_2O content. Sideronatrite is represented by two samples, SPT123 and SPT136. Jarosite and natrojarosite are represented by three samples of each species (as discriminated by XRD)—natrojarosite: SPT107, SPT108, SPT113; jarosite: SPT114, SPT115, SPT116. These two minerals are grouped together because they form a solid solution series. Compositionally, all of the samples have less than expected OH/H_2O contents. Samples SPT107, 108, 113, and 114 also contain accessory phases (Table 2). The Na_2O:K_2O ratios for these samples range from 0.03 to 7.55.

The samples containing both Fe^{3+} and Fe^{2+} or just Fe^{2+} that were used in this study are voltaite, romerite, and copiapite (Fe^{3+}- and Fe^{2+}-bearing), and szomolnokite, rozenite, and melanterite (Fe^{2+}-bearing). Voltaite is the dominant sulfate in SPT111, and substantial romerite is also present. Romerite is the dominant sulfate in samples SPT110, 122, and 134, but a pure romerite sample was not available. Copiapite is the only sulfate detected in SPT117 by XRD, but the compositional analysis is more consistent with ferricopiapite. Copiapite is the dominant sulfate in SPT131 and SPT138. Szomolnokite is the dominant sulfate in SPT144, which also contains other phases. Rozenite and melanterite are both present in SPT130, with rozenite dominating. There is also a small amount of Fe^{3+} present in this sample in an unidentified phase, likely a sulfate.

Iron-free sulfates used in this study include hexahydrite, kieserite, pickeringite, alunite, anhydrite, gypsum, anglesite, barite, and celestite. Hexahydrite is the only crystalline material detected in SPT143, although XRD analysis indicates the

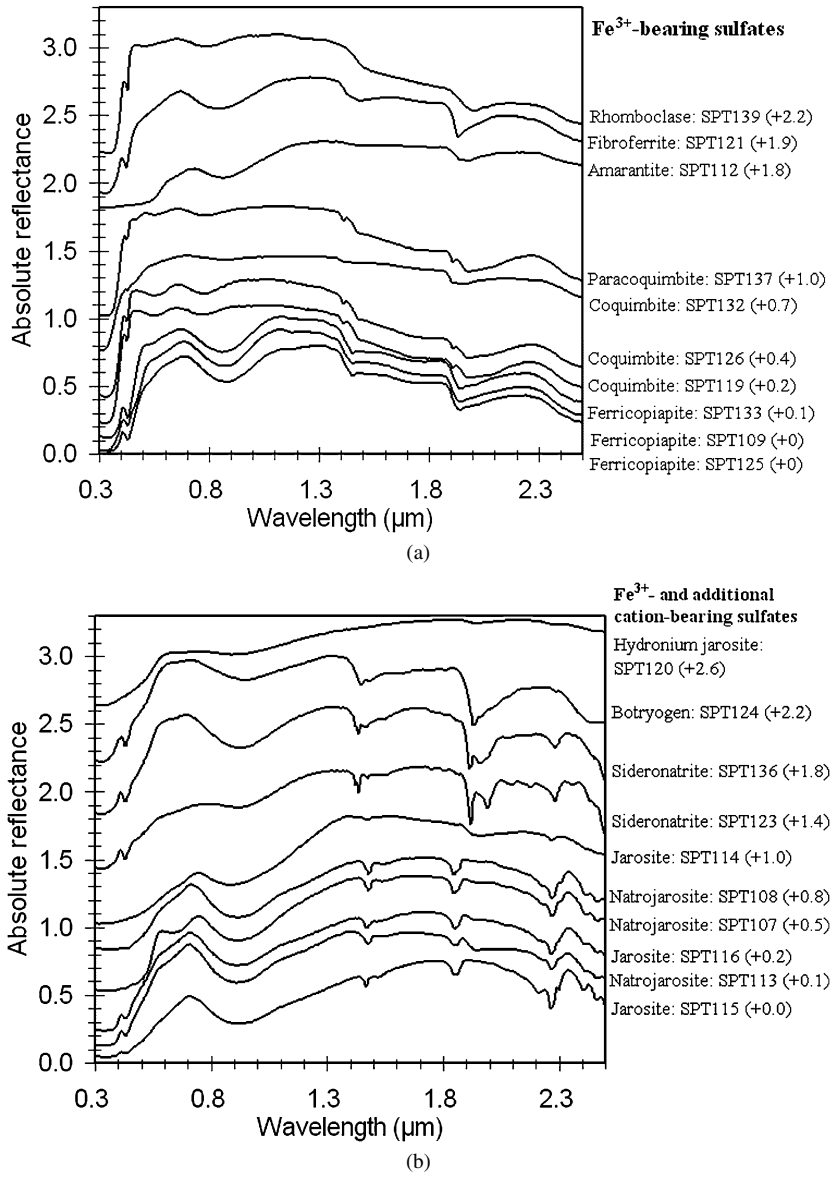

Fig. 1. 0.3–2.5 μm reflectance spectra of sulfates sorted by major cation groups. Numbers in brackets indicate linear vertical offset applied to the spectra for clarity. (a) Fe^{3+}-bearing samples; (b) Fe^{3+}- and additional cation-bearing samples; (c) Fe^{3+}- and/or Fe^{2+}-bearing samples; (d) Mg-, Al-, Ca-, K-bearing and Fe-free sulfates; (e) Pb- and Ba-bearing sulfates. The spectra were acquired by two different instruments under different viewing geometries and with different sample preparation procedures and merged in the 2.5 μm region, thus spectral features across this divide may not be directly comparable.

presence of an additional amorphous component. Kieserite is represented by SPT141. This sample also contains halite, and a small amount of Fe^{3+} in an unidentified sulfate phase. Pickeringite is the dominant sulfate in SPT118, 140, and 142. The small amounts of Fe^{3+} in all three samples result in weak absorption bands below 1 μm; pure pickeringite is expected to be spectrally featureless in this region. Alunite is represented in this study by SPT129, which contains less than the predicted amount of OH. Anhydrite is represented by a natural (SPT128) and synthetic (PIG002) sample. Gypsum is also represented by a natural (SPT127) and synthetic (PIG005) sample. Four essentially pure anglesite samples were used in this study: three natural (SPT145, 147, and 148) and one synthetic (PIG021). Two samples of essentially pure barite were available, one natural (SPT146) and one synthetic (PIG003).

4. Previous spectral studies

Sulfates have been the subject of a number of previous studies, and the most relevant are summarized here. Moenke (1962) presented a compendium of 5.5–25 μm (400–1800 cm^{-1}) transmission spectra of a number of sulfate minerals, along with a brief discussion of their general spectral features. Ross (1974) provided an overview of the infrared spectral-transmission properties of a number of sulfates, and discussed absorption band assignments for this class of minerals. Salisbury et al. (1987) also measured transmission spectra of a number of sulfate minerals. Adler and Kerr (1965) used transmission spectra of a number of sulfates to demonstrate that some sulfates have non-equivalent sites, based on the presence of a more than expected number of fundamental vibration bands.

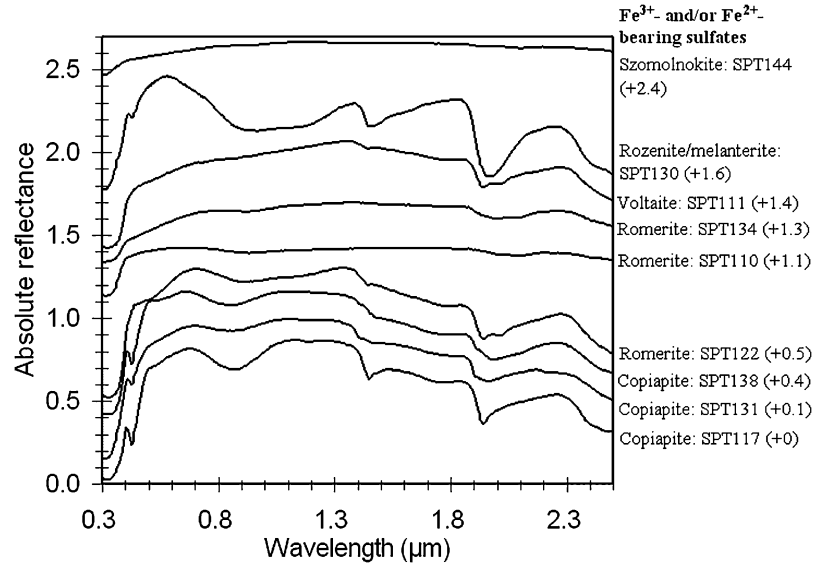

(c)

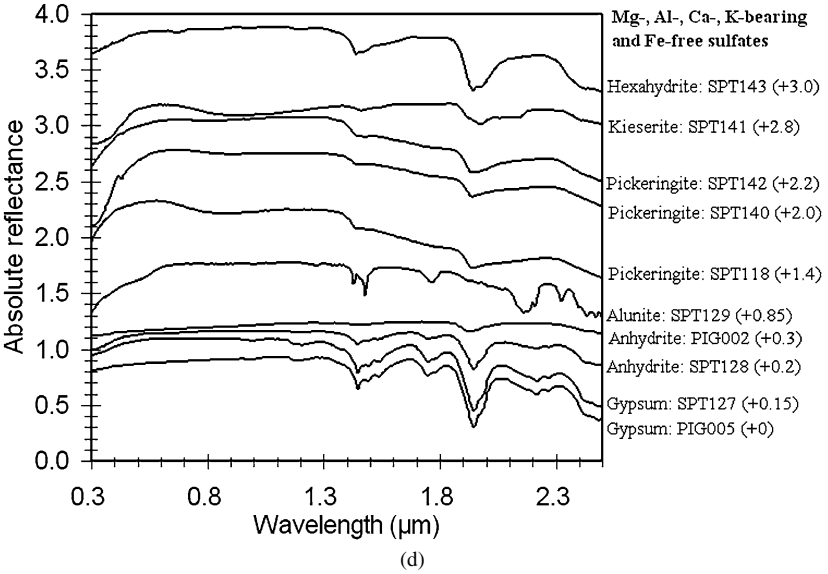

(d)

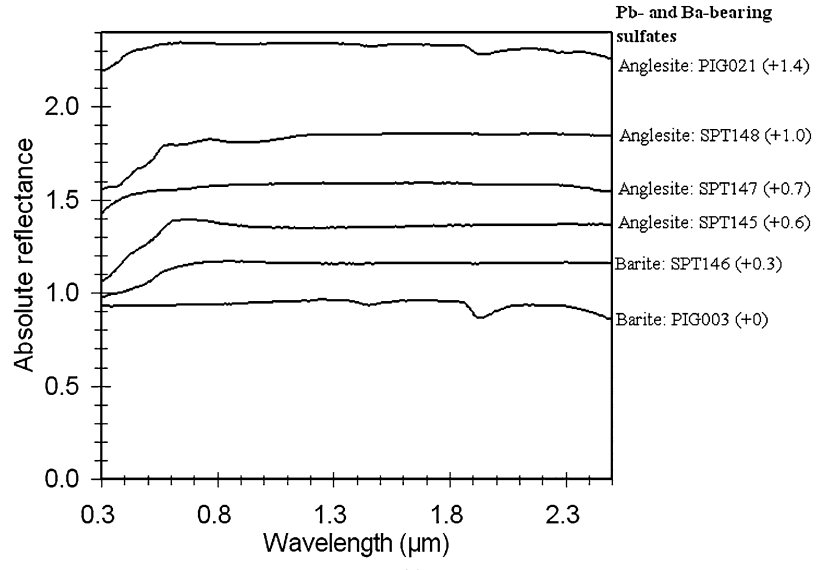

(e)

Fig. 1. (*continued*)

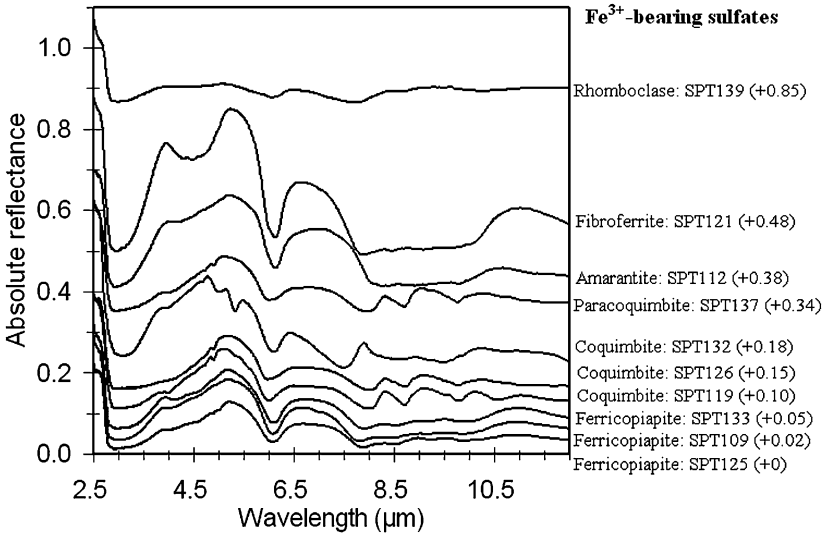

(a)

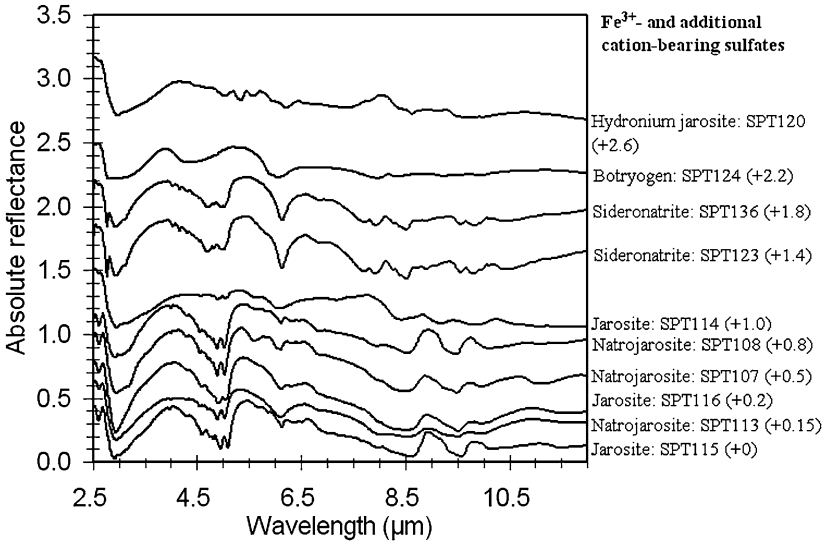

(b)

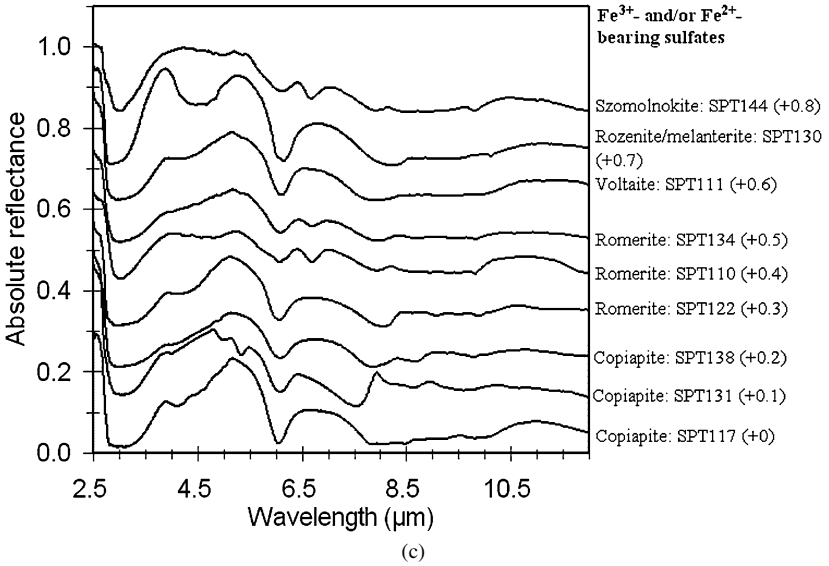

(c)

Fig. 2. 2.5–12 μm reflectance spectra of sulfates sorted by major cation groups. Numbers in brackets indicate linear vertical offset applied to the spectra for clarity. (a) Fe^{3+}-bearing samples; (b) Fe^{3+}- and additional cation-bearing samples; (c) Fe^{3+}- and/or Fe^{2+}-bearing samples; (d) Mg-, Al-, Ca-, K-bearing and Fe-free sulfates; (e) Pb- and Ba-bearing sulfates.

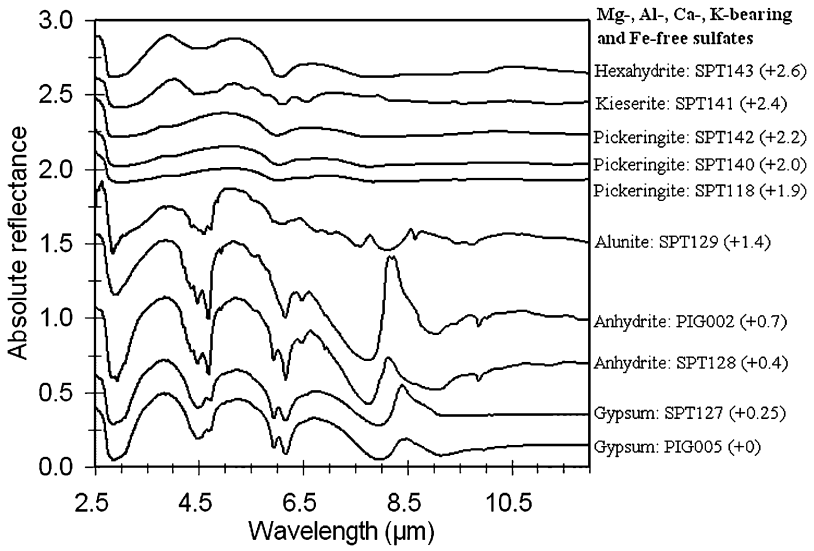

(d)

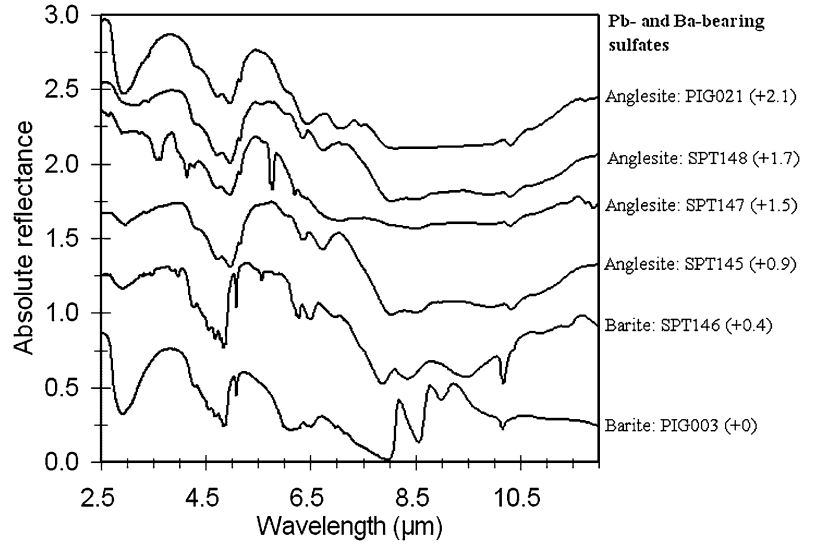

(e)

Fig. 2. (*continued*)

Morris (1963) used changes in absorption band positions and depths in hydrated calcium sulfate transmission spectra to enable discrimination of different hydrated calcium sulfates and determination of total H_2O content. Omori and Kerr (1963) measured transmission spectra (2–15 μm; 670–5000 cm^{-1}) of 58 sulfates. They found that the spectra could be grouped on the basis of similarities in spectral properties as follows: anhydrous sulfates show a strong S–O band near 9 μm (1100 cm^{-1}), and sometimes a second band near 8.5 μm (1180 cm^{-1}); alkali hydrous sulfates show a strong 3 μm (3300 cm^{-1}) band, a medium intensity 6 μm (1670 cm^{-1}) H_2O band, and a strong 9 μm (1100 cm^{-1}) S–O band; hydrous sulfates with Ca and other atoms show strong 3 μm (3300 cm^{-1}) and 9 μm (1100 cm^{-1}) bands, in some instances accompanied by bands near 4.5 μm (2200 cm^{-1}), 8.5 μm (1180 cm^{-1}), and 10 μm (1000 cm^{-1}); sulfates with OH, F, or Cl have a strong band or bands near 3 μm (3300 cm^{-1}), and multiple bands in the 9 μm (1100 cm^{-1}) region; hydrous sulfates with OH, F, or Cl have a broad band at 3–3.5 μm (2860–3300 cm^{-1}) and multiple bands in the 9 μm (1100 cm^{-1}) region (see Fig. 2).

Powers et al. (1975) measured infrared (2.5–250 μm; 40–4000 cm^{-1}) transmission spectra of jarosite, hydronium jarosite, alunite, and $Fe(OH)SO_4$, and made the following assignments: 1–2 bands in the 8.1–9.3 μm (1070–1230 cm^{-1}) region to ν_3 S–O bending; 1 band at 9.7–10 μm (1000–1030 cm^{-1}) to OH deformation; 2 bands in the 14.7–16.2 μm (620–680 cm^{-1}) region to ν_4 S–O bending; and 2 bands in the 18.9–19.8 μm (505–530 cm^{-1}) and 20.6–21.5 μm (465–485 cm^{-1}) regions to Fe–O stretching (up to two more weaker Fe–O bands may be present in the 17–23 μm (435–590 cm^{-1}) range). Roush (1996) measured transmission spectra (5–25 μm; 400–2000 cm^{-1}) of five sulfate minerals. The major absorption features were found in the 8–10 μm (1000–1250 cm^{-1}), 16 μm (625 cm^{-1}), and 19–21 μm (475–525 cm^{-1}) regions, and are attributable to ν_3 S–O bending, ν_4 S–O bending, and Fe–O stretching, respectively.

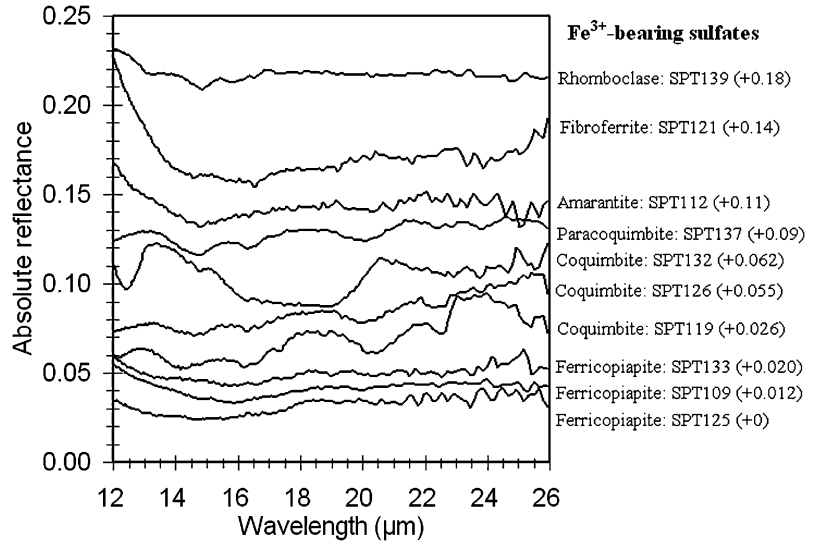

(a)

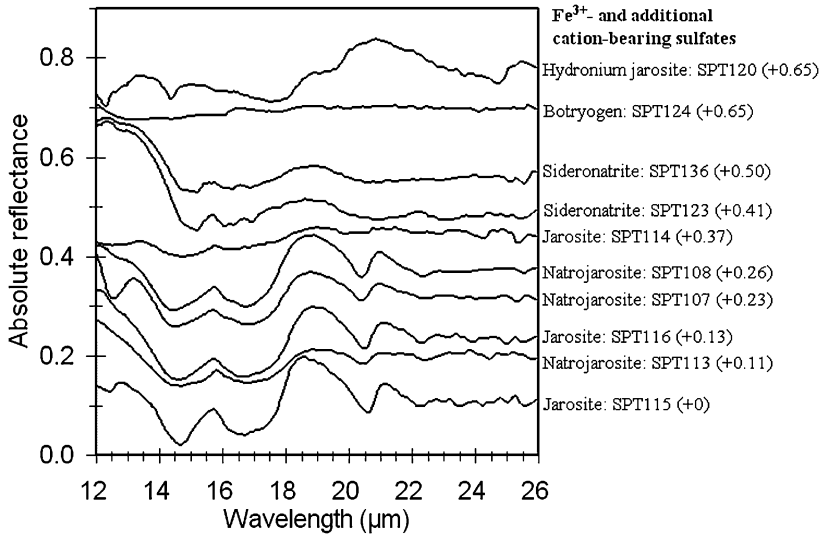

(b)

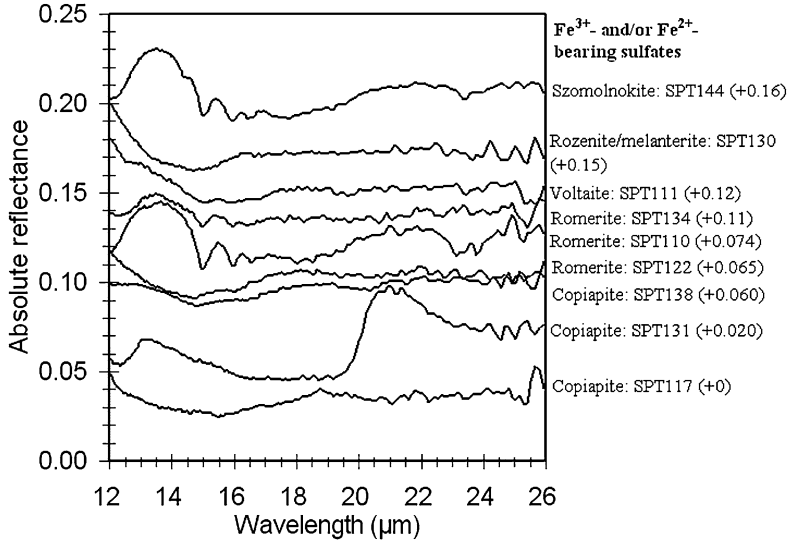

(c)

Fig. 3. 12–26 μm reflectance spectra of sulfates sorted by major cation groups. Numbers in brackets indicate linear vertical offset applied to the spectra for clarity. (a) Fe^{3+}-bearing samples; (b) Fe^{3+}- and additional cation-bearing samples; (c) Fe^{3+}- and/or Fe^{2+}-bearing samples; (d) Mg-, Al-, Ca-, K-bearing and Fe-free sulfates; (e) Pb- and Ba-bearing sulfates.

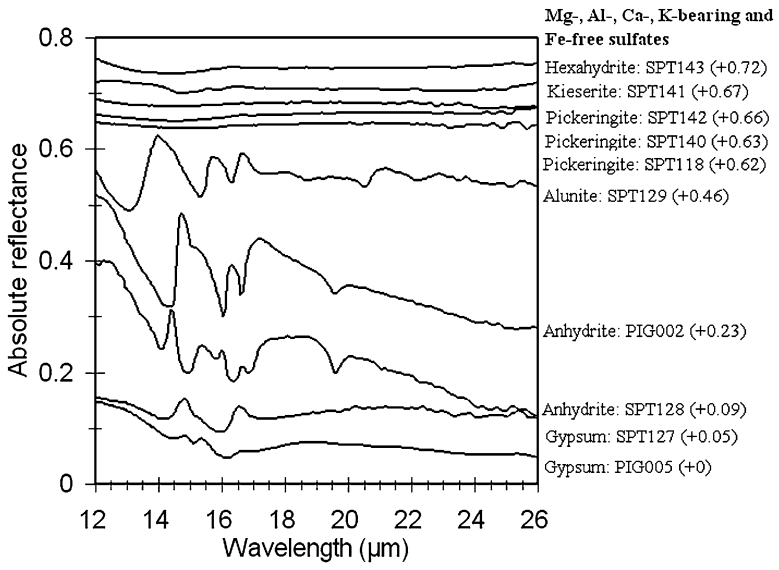

(d)

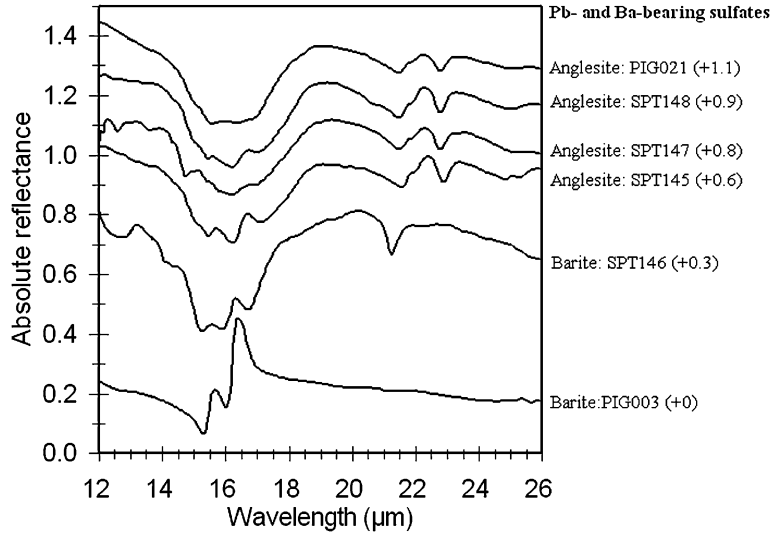

(e)

Fig. 3. (*continued*)

Lane (2004) presented 5–50 μm (200–2000 cm^{-1}) emission spectra of 30 sulfate minerals. These spectra are dominated by ν_3 S–O bands in the 8 μm (1250 cm^{-1}) region, with generally weaker ν_4 S–O bending bands in the 17 μm (590 cm^{-1}) region. Lane and Christensen (1998) presented emission spectra for gypsum and anhydrite. Both samples showed similar spectral behavior in the 5–25 μm (400–2000 cm^{-1}) range. They also showed that emission features above ~7 μm (<1430 cm^{-1}) can undergo dramatic changes as grain size is reduced below ~100 μm. Vassallo and Finnie (1992) measured emission spectra of gypsum, anhydrite, thenardite, and glauberite to track phase transformations as a function of temperature. They found that increasing temperature shifts S–O absorption bands to longer wavelengths and that the presence or absence of specific absorption bands is tied to phase transformations. The 8–13 μm emission spectra of a number of sulfates were investigated by Crowley and Hook (1996) to determine their detectability and discrimination in this wavelength region.

A series of papers by Rossman (1975, 1976a, 1976b, 1996) examined the 0.3–1.3 μm absorbance spectra of a number of Fe-bearing sulfate minerals. These studies showed the variety of Fe^{3+}-associated absorption bands present in these minerals and clarified the role of Fe^{3+} hydroxo-bridging in the expression of these spin-forbidden bands.

Bigham et al. (1990) and Murad and Rojík (2003) spectroscopically analyzed products of acid mine drainage. The major phase in their samples was a complex iron oxyhydroxysulfate, likely schwertmannite. The most intense absorption bands were found in the 8–10 μm (1000–1250 cm^{-1}) region, attributable to ν_3 S–O bending and ν_1 S–O stretching. A band at 16.4 μm (610 cm^{-1}) was attributed to ν_4 S–O bending. Assignment of an absorption band at 14.5 μm (690 cm^{-1}) was uncertain and tentatively attributed to Fe–O stretching.

Selected sulfates have also been characterized by reflectance spectroscopy by a number of investigators. Hunt et al. (1971), Hunt and Ashley (1979), Clark et al. (1990), and Grove et al.

(1992) presented reflectance spectra of a few sulfate minerals, but generally with little accompanying compositional or structural information. More systematic examinations of selected sulfate minerals in both reflectance and emittance were presented by Bishop et al. (2005a) and Lane et al. (2004).

Crowley (1991) and Crowley et al. (2003) measured 0.4–2.5 μm reflectance spectra of a number of H_2O/OH-bearing sulfates. The spectra of these minerals are dominated by H_2O-related absorption features, particularly in the 1.4 and 1.9 μm regions. Differences in these wavelength regions can be attributed to different bonding configurations for H_2O. A number of them also exhibit absorption bands in the 2.1–2.5 μm region. Hexahydrite and bloedite spectra measured by Crowley (1991) are similar to those measured by Dalton (2003). The thenardite spectrum (an anhydrous species) is essentially featureless and similar to that measured by Hunt et al. (1971).

Dalton (2003) measured 0.6–2.5 μm reflectance spectra of $MgSO_4{\cdot}nH_2O$ for $n = 0$, 1, 1.5, 2, 3, 4, 5, 6, and 7. These spectra are dominated by H_2O absorption bands in the 1.0, 1.2, 1.4, and 1.9 μm regions. With increasing H_2O content, the shapes of features in the 1.4 and 1.9 μm regions change as relative absorption band strengths vary. These absorption features also display significant temperature sensitivity (Dalton, 2003; Dalton et al., 2005), which is important not only for remote sensing of icy satellites, but also for Mars.

5. Results and interpretations

The reflectance spectra of the various samples have been compared to clarify some of the absorption band assignments over which confusion exists, as well as to search for spectral–compositional–structural systematic relations that can be used to discriminate the various sulfates included in this study. The ensuing discussion is subdivided on the basis of specific assignments and/or wavelength regions. In addition, the sulfates have been grouped in two different ways in subsequent tables depending on the spectral feature of interest. For H_2O/OH-related absorption features, the samples are grouped into anhydrous, H_2O-bearing, OH-bearing, and H_2O- and OH-bearing categories. For SO_4-related absorption features, the samples are grouped according to the structural classes described above.

At a broad level, reflectance spectra of sulfates will exhibit spectral features due to transition-series elements (if present), H_2O and/or OH (if present), and the SO_4 complexes. The wavelength positions and intensities of these bands are a function of composition, structure, and temperature (e.g., Omori and Kerr, 1963; Vassallo and Finnie, 1992; Dalton, 2003; Lane, 2004; Dalton et al., 2005). Chaban et al. (2002) have shown that changes in factors such as water abundance lead to shifts in absorption band positions, and changes in the number of absorption bands, with more water-related absorption bands appearing in samples with greater numbers of sites available to water molecules. Spectroscopic techniques can also be used to detect metastable forms and irreversible transformations resulting from heating (Vassallo and Finnie, 1992). A number of previous spectral studies, including those cited above, have been assimilated to develop an overview of the spectral properties of sulfate minerals.

5.1. Fe^{3+} absorption bands: 0.3–1.0 μm region

Fe^{3+}-bearing sulfates can display absorption bands when the iron atoms are linked through shared oxygens or hydroxide ions (Rossman, 1975). Absorption in the 0.3–1 μm region results from Fe^{3+} $^6A_{1g}$ spin–forbidden ligand field transitions in edge- or corner-shared $Fe^{3+}(O/OH)_6$ octahedra. Spin polarization in these linked octahedra enables magnetic coupling via superexchange interactions (Sherman et al., 1982; Sherman and Waite, 1985). This magnetic coupling causes relaxation of the selection rules and the spin–forbidden transitions occur (Bishop and Murad, 2005). These spin–forbidden bands are stronger in oxo-bridged Fe^{3+} cations than in hydroxo-bridged Fe^{3+} cations (Sherman, 1985). The positions of these absorption bands vary among different Fe^{3+} hydroxysulfates (Powers et al., 1975; Rossman, 1975, 1976a, 1976b). Absorption bands in the 0.43 μm ($^6A_{1g} \rightarrow (^4A_{1g}, {}^4E_g)$ transition) and 0.8–0.9 μm ($^6A_{1g} \rightarrow {}^4T_{1g}$ transition) regions are generally the most intense of these bands, followed by bands in the ∼0.5–0.55 μm region (Crowley et al., 2003). The 0.43 μm feature is narrower than the 0.8–0.9 μm feature in wavelength space.

The reflectance spectra of all of the hydroxy- and oxyhydroxy-sulfates containing only Fe^{3+} exhibit absorption bands in the 0.4–1 μm region. The results of this study agree with band positions determined by previous investigators for those samples which are common to more than one study, generally to within 10 nm (Table 3). The spectral resolution of the current data (5 nm) is insufficient to resolve the three absorption bands that should be present in coquimbite between 0.415 and 0.433 μm (Rossman, 1975), but multiple bands are suggested by the asymmetric shape of the absorption feature in this region (Fig. 4). Three absorption bands are expected because iron is present in three different coordination environments (Fang and Robinson, 1970). For jarosite, a weak inflection was detected near 0.63 μm (Fig. 4). The transmission spectrum of Rossman (1976a) also shows a weak inflection in this region, although this feature was not assigned to a specific mechanism. In amarantite, the absorption feature in the 0.43 μm region is generally weak in transmission spectra (Rossman, 1976b) and the presence of hematite in our sample lowers reflectance in this region, effectively masking this feature. Copiapite exhibits both Fe^{3+} (0.43, 0.55, 0.85 μm) and Fe^{2+} absorption bands (1.18 μm), consistent with its composition.

Of the sulfates containing both Fe^{3+} and Fe^{2+}, romerite and voltaite do not exhibit obvious Fe^{3+} bands, while copiapite exhibits strong Fe^{3+} bands (Fig. 5). This is due to the fact that Fe^{3+}-containing octahedra in romerite and voltaite are not hydroxo-bridged to adjacent octahedra (a requisite for enabling spin forbidden Fe^{3+} transitions to become allowed), but are hydroxo-bridged in copiapite. The results presented in Table 3 indicate that Fe^{3+} absorption bands, particularly those in the 0.43 and 0.8–0.95 μm regions, can be used to detect hydroxo-bridged Fe^{3+}-bearing/Fe^{2+}-free sulfates, as well as copiapite, and that the wavelength position of the 0.8–0.95 μm band can

Table 3
Wavelength positions (in μm) of minima of Fe^{3+}-associated absorption bands for Fe^{3+}-bearing sulfates

Mineral	Electronic transition			Source of data
	$^6A_{1g} \rightarrow (^4A_{1g}, {}^4E_g)$	$^6A_{1g} \rightarrow {}^4T_{2g}$	$^6A_{1g} \rightarrow {}^4T_{1g}$	
Reflectance spectra				
Rhomboclase[3]	0.429	0.53[a]	0.785	This study
Fibroferrite[2]	0.427	0.55[a]	0.844	This study
Amarantite[2]	0.43[b]	0.55[c]	0.865[b]	This study
Coquimbite[1]	0.423–0.433[d]	0.553–0.558	0.774–0.775	This study
Ferricopiapite[2]	0.431	0.55[a]	0.860–0.873	This study
Hydronium jarosite[3]	0.43[a]	0.68[a]	0.895	This study
Botryogen[2]	0.405, 0.432	0.5[a]	0.950	This study
Sideronatrite[2]	0.433	0.5[a], 0.63[a]	0.916–0.922	This study
Jarosite[3]	0.43–0.436	0.5[a], 0.63[a]	0.915–0.922	This study
Natrojarosite[3]	0.43–0.434	0.5[a], 0.63[a]	0.914–0.919	This study
Voltaite[4]	–	–	–	This study
Romerite[1]	–	–	–	This study
Copiapite[2]	0.430	0.55[a]	0.855–0.866	This study
Schwertmannite	0.43[a]	0.5[a], 0.6[a]	0.915–0.918	Bishop and Murad (1996)
Transmission spectra				
Coquimbite[1]	0.415, 0.427, 0.433	0.561	0.778	Rossman (1975)
Magnesiocopiapite[2]	0.430	~0.555, ~0.598	~0.818, 0.864	Rossman (1975)
Botryogen[2]	0.412, 0.432	~0.498	0.939	Rossman (1975)
$Fe(OH)SO_4$	0.428	~0.490	0.945	Rossman (1975)
Butlerite[2]	0.424	0.488	0.920	Rossman (1976a)
Parabutlerite[2]	0.416, 0.428	0.478	0.816, 0.912	Rossman (1976a)
Stewartite	0.428		0.880	Rossman (1976a)
Jarosite[3]	0.434	~0.472	0.933	Rossman (1976a)
Fibroferrite[2]	0.423	0.555	0.840	Rossman (1976a)
Amarantite[2]	0.424, 0.434, 0.442	0.500	0.866	Rossman (1976b)
Metavoltine[1]	0.464		0.855	Rossman (1976b)

Note. Absorption bands associated with accessory phases have been omitted.
[a] Shoulder, band position approximate.
[b] Band position may be affected by the presence of hematite in the sample.
[c] Weak band expected at this wavelength may be obscured by presence of hematite.
[d] Spectral resolution (5 nm) of current study inadequate to resolve expected closely spaced bands in 0.43 μm region.
[1] Structure consists of finite clusters of polyhedra.
[2] Structure consists of infinite chains.
[3] Structure consists of infinite sheets.
[4] Structure consists of infinite framework.

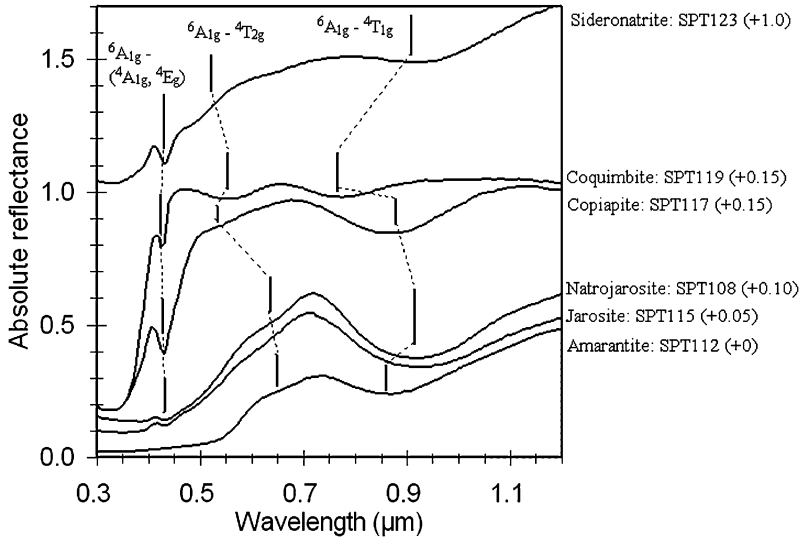

Fig. 4. Reflectance spectra of the region of Fe^{3+} absorption bands (0.3–1.2 μm) for selected Fe^{3+}-bearing samples. Numbers in brackets indicate linear vertical offset applied to the spectra for clarity.

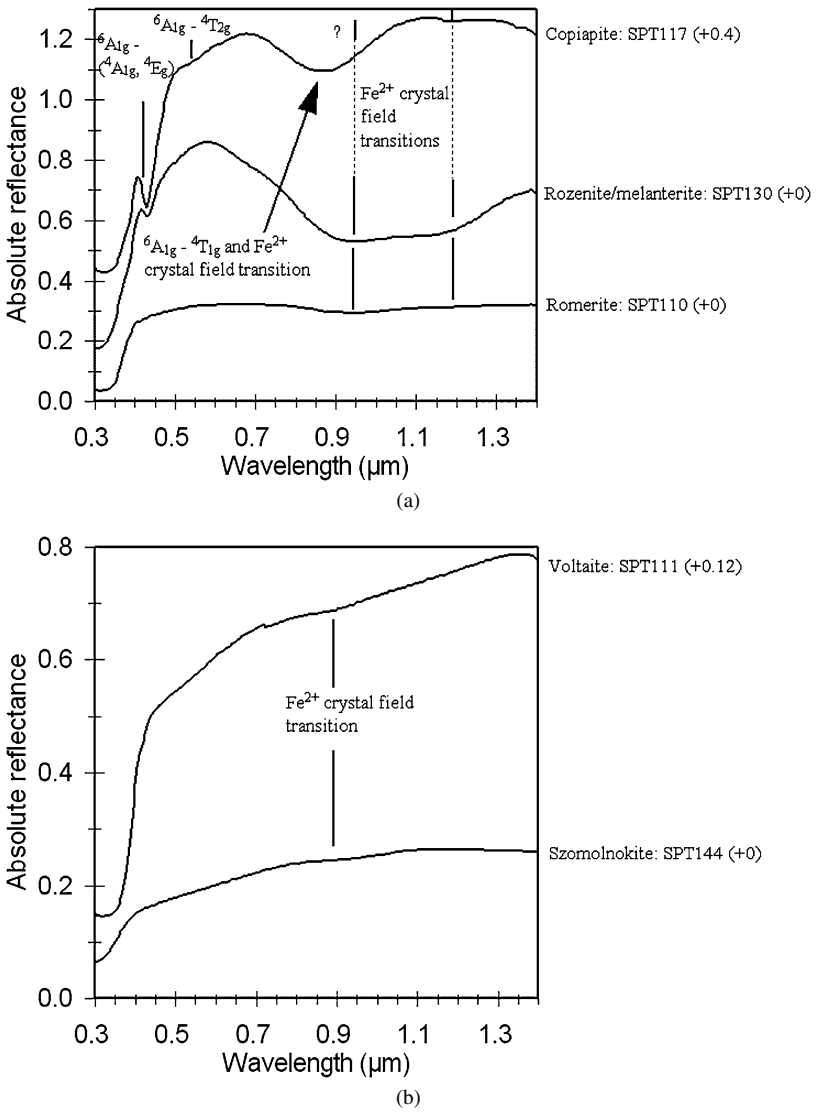

Fig. 5. Reflectance spectra (0.3–1.4 μm) of Fe^{3+}- and/or Fe^{2+}-bearing sulfates. Numbers in brackets indicate linear vertical offset applied to the spectra for clarity. (a) Spectra of samples showing two absorption bands near 0.9 and 1.17 μm; (b) spectra of sample showing only a single absorption band near 0.9 μm.

be used to discriminate most of them. In cases where absorption band positions do not uniquely discriminate an individual sulfate (e.g., sideronatrite versus jarosite; Table 3, Fig. 4), relative band intensities may provide a potential method of discrimination.

Fe^{3+}-bearing non-sulfates may also display absorption bands similar to those seen in the Fe^{3+}-bearing sulfates. In particular, we have found that some serpentinites and goethite can also display spin–forbidden Fe^{3+} transitions (Morris et al., 1985; King and Clark, 1989; Clark et al., 1990), broadly comparable to those seen in jarosite (Fig. 6). The shape and width of the 0.43 μm absorption feature differs between jarosite and the serpentinites, and the wavelength position of the goethite absorption band (0.45 μm) differs from that of the jarosite (0.43 μm) and is very intense, as expected for oxo-bridged Fe^{3+} (Sherman et al., 1982). In addition, there are differences between jarosite and the other sample spectra in terms of the positions of the longer wavelength Fe^{3+} absorption bands. The visible/near infrared region could potentially be used to distinguish sulfate from non-sulfate hydroxo-bridged Fe^{3+}-bearing minerals.

5.2. *Fe^{2+} absorption bands: 0.9–1.2 μm region*

Ferrous iron is present in a number of common sulfates such as melanterite, halotrichite, rozenite, and copiapite. There is little data on the nature of Fe^{2+}-associated absorption bands in sulfates. This was investigated by comparing the reflectance spectra of Fe^{3+}, Fe^{2+}, and Fe-free synthetic ammonium-bearing sulfates (Fig. 7). Comparison of the three spectra indicates that prominent Fe^{2+}-associated absorption bands occur near 0.9 and 1.2 μm, in contrast to the Fe^{3+} feature which is located near 0.83 μm (Crowley et al., 2003). The appearance of two Fe^{2+} absorption bands in the 0.9–1.2 μm region is similar to type A clinopyroxene spectra, whose absorption bands are at-

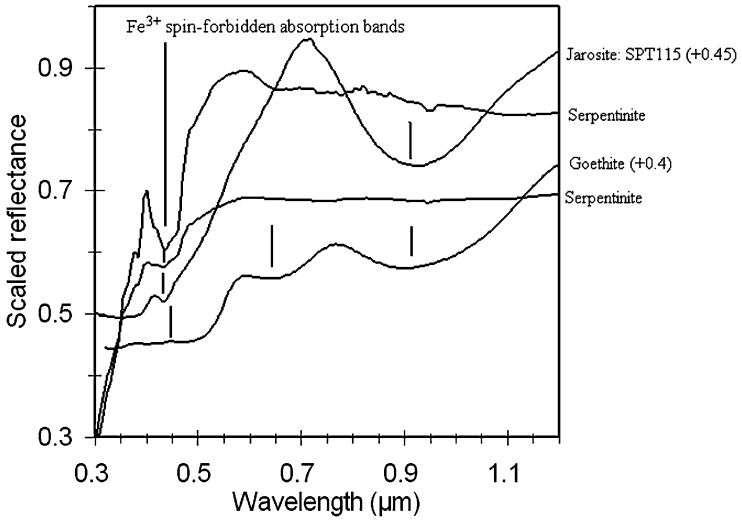

Fig. 6. Reflectance spectra of goethite, jarosite (SPT115), and two serpentinites, showing details of absorption bands in the 0.3–1.2 μm region. The goethite and jarosite spectra have been linearly vertically offset by the amounts shown in brackets in order to enhance details in the visible spectral region.

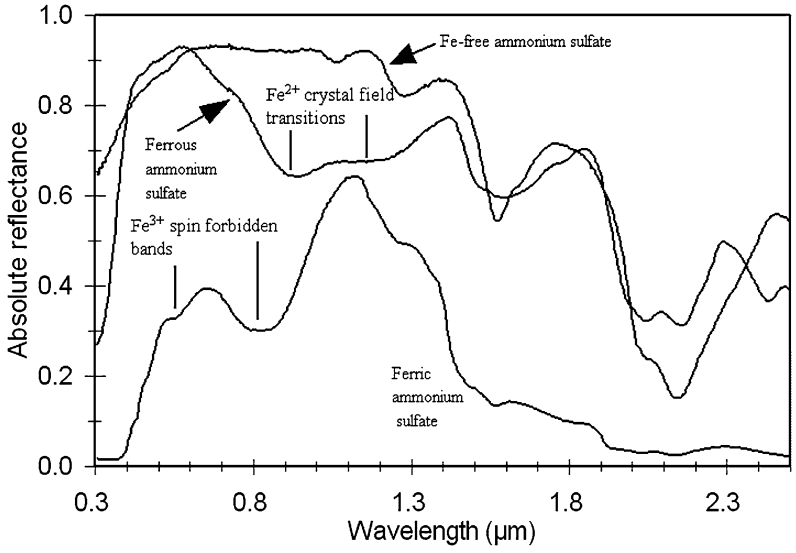

Fig. 7. Reflectance spectra of synthetic ferric ammonium sulfate ($FeNH_4(SO_4)_2 \cdot 12H_2O$; unsorted), synthetic ferrous ammonium sulfate ($(NH_4)_2FeSO_4 \cdot 6H_2O$; <45 μm grain size), and synthetic ammonium sulfate ($(NH_4)_2SO_4$; <45 μm grain size).

tributable to Fe^{2+} crystal field transitions (Cloutis and Gaffey, 1991; Burns, 1993b).

The Fe^{2+}-bearing sulfates that were analyzed in this study include three species containing only Fe^{2+} (szomolnokite, rozenite, melanterite), two containing both Fe^{2+} and Fe^{3+} (romerite, copiapite), and one containing Fe^{2+}, Fe^{3+}, and other cations (voltaite). All are expected to exhibit Fe^{2+} crystal field transition bands. Absorption bands in these spectra that are likely associated with Fe^{2+} are listed in Table 4. Three types of Fe^{2+} coordination occur in these minerals. The Fe^{2+} in melanterite, romerite, and copiapite is coordinated by H_2O, in szomolnokite and rozenite it is coordinated by SO_4 and H_2O, and in voltaite the coordination is more complicated. Spectra of the minerals where the Fe^{2+} is coordinated by H_2O exhibit two bands near 0.9–0.95 and 1.17 μm, whereas the others exhibit a single band near 0.9 μm (Fig. 5). It should be noted that one romerite spectrum (SPT134) shows no evidence for a 1.17 μm band.

Table 4
Wavelength positions of minima for likely or presumed Fe^{2+}-associated absorption bands for the sample spectra used in this study

Mineral	Type of Fe^{2+} coordination	Band position (μm)
Rozenite/melanterite	SO_4 and H_2O (rozenite)	
	H_2O (melanterite)	~0.92[a], ~1.17
Romerite	H_2O	~0.947[a], ~1.17
Copiapite	H_2O	0.9?[b], 1.17?[b]
Szomolnokite	SO_4 and H_2O	~0.9
Voltaite	Complex	~0.9

Note. Absorption bands associated with accessory phases have been omitted.
[a] Band may be due to Fe^{3+} and/or consist of overlapping Fe^{3+} and Fe^{2+} bands.
[b] Weak bands may be present but obscured by other bands.

5.3. H_2O, OH, and metal–OH absorption bands

The presence of H_2O and/or OH can lead to a number of absorption features. The free H_2O molecule has a symmetric H–O–H stretch (ν_1) at 2.738 μm, an asymmetric H–O–H stretch (ν_3) at 2.66 μm, an H–O–H bend (ν_2) at 6.27 μm (Clark et al., 1990), and a rotational fundamental near 20 μm (Bayly et al., 1963). In ice, in which hydrogen bonding occurs (as it does for many hydroxysulfates), the stretching and bending bands shift to 3.10 μm (ν_1), 2.94 μm (ν_3), and 6.06 μm (ν_2). For isolated H_2O molecules, overtones and combinations of these bands are expected near 0.94 μm ($2\nu_1 + \nu_3$), 1.13 μm ($\nu_1 + \nu_2 + \nu_3$), 1.38 μm ($\nu_1 + \nu_3$), 1.45 μm ($2\nu_2 + \nu_3$), and 1.88 μm ($\nu_2 + \nu_3$). In ice, overtone and combination bands are seen in transmission and reflectance spectra at 1.04 μm (vs 0.94 μm), 1.25 μm (vs 1.13 μm), 1.50–1.66 μm (vs 1.38–1.45 μm), and 1.96–2.05 μm (vs 1.88 μm) (Buijs and Choppin, 1963; Yamatera et al., 1964; Thomas et al., 1965; Clark, 1981). The H_2O ice molecule also has rotational and translational vibration bands near 13 μm (770 cm^{-1}) or 20 μm (500 cm^{-1}), and near 48 μm (210 cm^{-1}), respectively (Bayly et al., 1963; Ryskin, 1974). In ice spectra, an absorption band is seen near 2.55–2.6 μm, as a shoulder on the short wavelength wing of the H_2O stretching fundamentals, and has been assigned to a combination of the asymmetric stretch (ν_3) and the rotational fundamental (ν_L) that occurs near 20 μm (500 cm^{-1}) (Bayly et al., 1963).

OH^- has only one stretching vibration (ν_{OH}), located near 2.8 μm (3570 cm^{-1}). Overtones of this absorption are expected near 1.4 μm (7140 cm^{-1}) ($2\nu_{OH}$) and 0.95 μm (10,700 cm^{-1}) ($3\nu_{OH}$). The wavelength position of the OH vibration is related to the electronic environment of the site that it occupies (Ryskin, 1974). OH also has rotational vibration bands in the 9–25 μm (400–1100 cm^{-1}) range and translational vibration bands in the 15–33 μm (300–670 cm^{-1}) range (Moenke, 1974). The presence of a 1.9 μm band indicates molecular H_2O in a sample, whereas the absence of a 1.9 μm band but the presence of a 1.4 μm band indicates that only OH is present.

5.3.1. Metal–OH absorption bands: 10–25 μm (400–1000 cm^{-1}) region

Metals present in various minerals, where the metal is bonded to OH or O in octahedral sites can give rise to metal–OH or metal–O bending vibrations, in addition to affecting the wavelength position of the O–H stretching fundamentals (Farmer, 1974a). Metal–OH bending vibrations occur largely in the 10–17 μm (590–1000 cm^{-1}) region (Ross, 1974; Farmer, 1974a; Moenke, 1974). In general, Fe–OH bending bands occur in the 19–20 μm (500–525 cm^{-1}) region; jarosite–alunite minerals exhibit two or three metal–OH bending bands near 12.5 μm (800 cm^{-1}) and 20 μm (500 cm^{-1}), Na-, K-, Mg-, Ca-bearing sulfates exhibit one or two bands between 11.8 μm (850 cm^{-1}) and 14 μm (715 cm^{-1}), with a number of other mixed-cation species showing one or two bands in the 13–19.2 μm (520–770 cm^{-1}) range (Ross, 1974). It should be noted that band assignments in longer-wavelength regions are often uncertain (e.g., Ross, 1974; Ryskin, 1974); for example, other investigators have assigned a band at 20.4 μm (490 cm^{-1}) to the ν_2 S–O vibrational mode rather than a metal–OH bend (e.g., Lane and Christensen, 1998).

Fe–O–Fe stretching bands appear near 14.2 μm (705 cm^{-1}), 20.7 μm (480 cm^{-1}), and 23.8–25 μm (400–420 cm^{-1}) for schwertmannite (Schugar et al., 1972; Bigham et al., 1990, 1994; Bishop and Murad, 1996). Powers et al. (1975) assigned up to five bands in the 17–25 μm (400–590 cm^{-1}) region to Fe–O vibrations for a number of iron-bearing sulfates. They found that the one or two strongest bands were located between 18.9 μm (530 cm^{-1}) and 21.5 μm (465 cm^{-1}). In jarosite, absorption bands at 19.2 μm (520 cm^{-1}) and 20.9 μm (478 cm^{-1}) have been assigned to Fe–O vibrations. In natrojarosite, these bands shift to 19.5 μm (512 cm^{-1}) and 20.8 μm (480 cm^{-1}) (Sasaki et al., 1998).

Mg–O stretching was the mechanism assigned to absorption bands at 24.3 μm (412 cm^{-1}) and 24.9 μm (402 cm^{-1}) in the spectrum of kieserite (Schubert, 1967). Other investigators have found Mg–O stretching bands in other sulfate minerals near 50 μm (200 cm^{-1}) (Ross, 1974). In alunite, absorption bands at 14.7 μm (681 cm^{-1}), 15.8 μm (631 cm^{-1}), 16.6 μm (602 cm^{-1}). 18.9 μm (529 cm^{-1}), and 23.1 μm (432 cm^{-1}) have been assigned to $AlO_2(OH)_4$ vibrations (Breitinger et al., 1997). Information on other metal–O stretching bands in sulfates is generally lacking. The available data for various metal–OH vibrations in common sulfate minerals are summarized in Table 5.

H–O–H/O–H rotational and translation bands are expected longward of ∼12 μm (830 cm^{-1}), and the rotational vibration is expected somewhere between 12 and 20 μm (500–830 cm^{-1}) (Table 6) (Ross, 1974). However, band assignments beyond ∼17 μm (<590 cm^{-1}) are not fully resolved and hence the utility of bands in this region is still limited. In addition, absorption bands in the 12 μm region occur in or near the region also occupied by S–O bending vibrations. The shape and intensity of these bands varies widely, from strong and sharp bands through very weak inflections, to no evident band. For those minerals common to both Ross (1974) and this study (Table 6), band positions are generally in good agreement. However, the diversity of intensities, shapes, and wavelength positions does not permit these assignments to be extended to other sulfates with a reasonable degree of confidence.

Some, but not all, of the H_2O-bearing sulfates exhibit a resolvable absorption band in the 11–13 μm (770–900 cm^{-1}) region, that is likely attributable to H_2O rotation (Tables 6 and 7). The OH-bearing sulfates, such as jarosite and alunite have a number of OH rotational and translational bands longward of 12 μm (<830 cm^{-1}) (Ross, 1974; Serna et al., 1986; Bishop and Murad, 2005) (Tables 6 and 7). In addition, alunite has an OH deformation band near 8.7 μm (1150 cm^{-1}) (Breitinger et al., 1997). The nominally anhydrous sulfates, anhydrite, barite, celestite, and anhydrite (which contains some gypsum) may exhibit weak absorption bands associated with H_2O in the 1.4, 1.9, 3, and 6 μm regions. These are likely due to some combination of adsorbed H_2O, fluid inclusions, or incipient alteration, and are not characteristic of the pure anhydrous phases.

Table 5
Wavelength positions of absorption bands due to metal–oxygen vibrations in transmission and reflectance spectra from other investigators

Mineral	Band positions	Assignment	Source of data
Jarosite	19.2 μm (520 cm^{-1}), 20.9 μm (478 cm^{-1})	O–Fe	Sasaki et al. (1998)
Jarosite	18.2 μm (550 cm^{-1}), 19.8 μm (505 cm^{-1})		
	21.3 μm (469 cm^{-1}), 22.7 μm (441 cm^{-1})	FeO_6 vibrations	Powers et al. (1975)
Natrojarosite	19.5 μm (512 cm^{-1}), 20.8 μm (480 cm^{-1})	O–Fe	Sasaki et al. (1998)
Hydronium jarosite	19.8 μm (505 cm^{-1}), 21.5 μm (465 cm^{-1})		
	26.2 μm (383 cm^{-1})	FeO_6 vibrations	Powers et al. (1975)
Schwertmannite	21.7–24.4 μm (410–460 cm^{-1})	Fe–O stretch	Bigham et al. (1990)
	14.2 μm (704 cm^{-1}), 20.7 μm (483 cm^{-1})	Fe–O stretch	Bigham et al. (1994)
	23.8–25.0 μm (400–420 cm^{-1})	Fe–O stretch	Bishop and Murad (1996)
Alunite	16.8 μm (595 cm^{-1}), 18.9 μm (528 cm^{-1})		
	20.6 μm (486 cm^{-1}), 23.1 μm (433 cm^{-1})	FeO_6 vibrations	Powers et al. (1975)
Alunite	14.7 μm (681 cm^{-1}), 15.8 μm (631 cm^{-1})		
	16.6 μm (602 cm^{-1}), 18.9 μm (529 cm^{-1})		
	23.1 μm (432 cm^{-1})	$AlO_2(OH)_4$ vibrations	Breitinger et al. (1997)
Kieserite	24.3 μm (412 cm^{-1}), 24.9 μm (402 cm^{-1})	Mg–O stretch	Schubert (1967)

Table 6
OH/H_2O rotational mode absorption bands in transmission and reflectance spectra of sulfates

Mineral	Absorption band position in transmittance spectra (μm)	Present in reflectance spectra? (Position (μm))
Alunite	12.5	Possibly, as shoulder on wing of more intense 13.1 μm band
	12.8	Yes (13.1 μm)
	19.8	Yes (20.5 μm)
Amarantite	18.9	Yes (19.3 μm)
	19.7	Yes (20.3 μm)
Botryogen	13.0	Yes (13.2 μm)
Copiapite	13.3	Possibly, as shoulder on wing of intense 15.5 μm S–O band
	18.0	Yes (∼18 μm)
Coquimbite	11.9	∼12 μm, broad, weak band
Jarosite	12.7	∼12.4 μm[a]
	19.5	20.6[b]
Romerite	11.7	Yes (12.0 μm)
	14.1	Possibly as a shoulder on wing of intense 15 μm S–O band
Pickeringite	13.8	Possibly, may be obscured by intense 14.8 μm S–O band

Note. Transmission data values are from Ross (1974).
[a] A weak absorption band is located at 12.4 μm in jarosite. A weak inflection is present near 13.2 μm. In natrojarosite an inflection is present near 12.6 μm.
[b] This band shifts to 20.4 μm in natrojarosite.

OH- and/or H_2O-related absorption features occur in both reflectance and transmission spectra of sulfates that contain these molecular groups (e.g., Powers et al., 1975; Serna et al., 1986; Bigham et al., 1990; Bishop and Murad, 1996). The number of absorption features is a function of the number of distinct electronic environments available to H_2O/OH and the degree of hydrogen bonding (Buijs and Choppin, 1964; Ross, 1974; Clark, 1981; Clark et al., 1990; Chaban et al., 2002). A number of the OH/H_2O overtone and combination bands, to wavelengths as low as ∼1 μm, may be present in reflectance spectra of iron-free sulfates, due to their high overall reflectance (e.g., Dalton, 2003). The shapes and intensities of these bands change as a function of H_2O content and structural state (Dalton, 2003).

The minerals used in this study include samples containing only OH, only H_2O, or both, with abundances of these molecules spanning a wide range, as well as minerals containing other types of O + H groups, such as rhomboclase (H_5O_2), and hydronium jarosite (H_3O) (Table 1). Diverse behavior of H_2O- and OH-associated bands is expected for two main reasons: (1) most sulfates possess extensive hydrogen bonding, and for an H_2O molecule, zero, one, or two hydrogen molecules may participate in hydrogen bonding; and (2) many of the sulfate minerals used in this study possess more than one structurally distinct site that can be occupied by H_2O or OH. Band positions can be further modified by cation substitutions. Simple structural formulas may not fully reflect the site symmetries of H_2O or OH within a sulfate. As an example, the formula of gypsum ($CaSO_4(H_2O)_2$) is suggestive of a single environment for H_2O, but it exhibits at least three H–O–H bending fundamentals in the 6 μm (1670 cm^{-1}) region due to the asymmetric geometry of the site occupied by H_2O and the consequent differences in H–O–H bond lengths (Hunt et al., 1971).

The OH-bearing and H_2O-free samples (jarosite, natrojarosite, and alunite) all contain six OH groups in the unit cell (Table 1), and are structurally similar. They all exhibit weak and non-diagnostic H_2O features near 1.9 and 6 μm; this is not unexpected as adsorbed H_2O and/or minor accessory H_2O-bearing phases may be present. The 3 μm region of all the spectra shows well-defined OH stretching absorption bands, with the strongest band centered near 2.94 μm (ν_3) and a weaker band near 3.0–3.15 μm (ν_1) for jarosite and natrojarosite, and near 2.84 and 2.92 μm for alunite (as well as some finer structure in this region) (Fig. 8, Tables 7 and 8). The presence of more than one OH stretching fundamental is not unexpected as the six OH groups are not all identically coordinated in these minerals (Hawthorne et al., 2000). The 1.4 μm region of the jarosite and natrojarosite spectra show two absorption bands, occurring at longer wavelengths in natrojarosite (Fig. 8, Table 8). These are attributable to first-order overtones of ν_{OH}. The alunite spectrum exhibits at least four absorption bands in this region, two strong bands at 1.425 and 1.467 μm, and two weaker bands near 1.46 and 1.50 μm (Table 8). These band positions agree

Table 7
Wavelength positions (in μm) of minima of H_2O- and OH-associated absorption bands in the 3, 6, and >8 μm regions

Mineral	OH stretching fundamentals (3 μm region)	H_2O stretching fundamentals (3 μm region)	H_2O bending fundamentals (6 μm region)	OH/H_2O rotation or translation (>8 μm region)
H_2O- and OH-free				
Anhydrite[4]	–	–	–	–
Anglesite[5]	–	–	–	–
Barite[5]	–	–	–	–
OH-bearing				
Jarosite[4]	2.87[a], 2.93–2.94, 3.0–3.15[a]	–	–	9.6[c], 12.4[d], 17.2, 20.6[d]
Natrojarosite[4]	2.80[a], 2.89[a], 2.94–2.96, 3.05–3.20[a]	–	–	9.5[c], 12.6[a,d], 17.0[a], 20.4[d]
Alunite[4]	2.84, 2.88, 2.93[a], 3.08[a]	–	–	8.7, 13.1[d], 16.4, 17.8, 20.5[d]
H_2O-bearing				
Kieserite[5]	–	2.9[b], 3.1[b]	6.04, 6.17, 6.58	11.8
Szomolnokite[5]	–	2.95[a,b], 3.06[b]	5.95[a], 6.11	12.0
Voltaite[5]	–	2.95[b], 3.1[a,b]	6.11	12.5
Rhomboclase[4]	–	~3.0[b]	6.06	13.3
Gypsum[4]	–	2.86, 2.96, 3.09	5.92, 6.11[a], 6.18	–
Amarantite[3]	–	2.93, 3.1[a]	6.13	19.3, 20.3
Coquimbite[2]	–	~3.0[b]	5.99–6.01	12.0
Romerite[2]	–	3.05[b]	5.8[a], 6.08, 6.2[a], 6.70[c]	12.0
Rozenite[2]	–	2.85[b], 3.05[b]	6.03[a], 6.15	–
Hexahydrite[1]	–	2.85[b], 3.1[b]	6.0[a], 6.10	–
Pickeringite[2]	–	2.95[b], 3.1[b]	6.02, 6.59[c]	11.3
H_2O- and OH-bearing				
Hydronium jarosite[4]	~2.8[a]	2.97, 3.1[a]	5.97[a], 6.21	12.3, 17.5
Sideronatrite[3]	2.78, 2.94[a,c]	3.0[c], 3.12[c]	5.8[a], 6.13, 6.86[c]	12.8
Ferricopiapite[3]	2.82	2.95[b], 3.1[b]	6.09, 6.16	–
Copiapite[3]	2.74[a], 2.82	2.95[b], 3.1[b]	6.05, 6.17[a]	18[b]
Botryogen[3]	2.80, 2.89	2.95[b], 3.1[b]	5.93[a], 6.06, 6.16[a]	13.2
Fibroferrite[3]	2.78[a]	2.95[b], 3.1[b]	6.0[a], 6.15	21[b]

Note. Absorption bands that are not integral to the mineral (e.g., due to adsorbed water), but may be present in the spectra, have been omitted.
[a] Shoulder on a more intense absorption band, wavelength position approximate.
[b] Broad band, wavelength position approximate.
[c] Identity as H_2O or OH band uncertain.
[d] Band is likely an OH bending band (Ross, 1974).
[1] Structure consists of isolated SO_4 tetrahedra.
[2] Structure consists of finite clusters of polyhedra.
[3] Structure consists of infinite chains.
[4] Structure consists of infinite sheets.
[5] Structure consists of infinite framework.

well with the calculated first order overtones of the observed OH stretching fundamentals.

The H_2O-bearing/OH-free sample spectra exhibit up to four resolvable absorption bands in the H–O–H bending region near 6 μm (1670 cm^{-1}) (Table 7). The first order H–O–H bending overtones and H–O–H stretching fundamentals occur in the 2.9–3.1 μm region. In this group, the 3 μm region is generally featureless and individual absorption bands are difficult to recognize. In contrast to other minerals and mineral groups (Milliken and Mustard, 2004, 2005), there is no strong correlation between the depths of these absorption bands and H_2O content in our sulfate samples, although increasing H_2O generally results in lower reflectance in this region. The 1.9 μm region is characterized by one or more absorption bands (Table 8), and the number of bands in this region closely follows that of the 6 μm region. In particular, minerals such as gypsum and kieserite, whose spectra contain multiple and well-resolved absorption bands in the 5.8–6.8 μm (1470–1720 cm^{-1}) region, exhibit a greater number of bands in the 1.9 μm region, which can be attributed to $\nu_2 + \nu_1$ and $\nu_2 + \nu_3$ combinations.

The 1.8 μm region of most of the sulfate minerals exhibits a broad, shallow absorption feature and/or between one and three narrow absorption bands (Fig. 1, Table 9). In gypsum, the band at 1.75 μm was assigned to combinations of OH/H_2O librations, bends and stretches (Hunt et al., 1971), while in alunite the band at 1.775 μm was assigned to a combination of the OH fundamental stretch with the first overtone of the Al–OH bend. Subsequently, Clark et al. (1990) questioned the assignment of the alunite band, as it is not seen in other Al–OH bearing minerals. Its appearance and shape in relation to sulfate composition and longer wavelength bands allows us to place some constraints on its possible identity. No absorption feature is seen in the 1.8 μm region of anhydrous (OH- and/or H_2O-free) sulfate spectra; a single broad and shallow band is generally present in

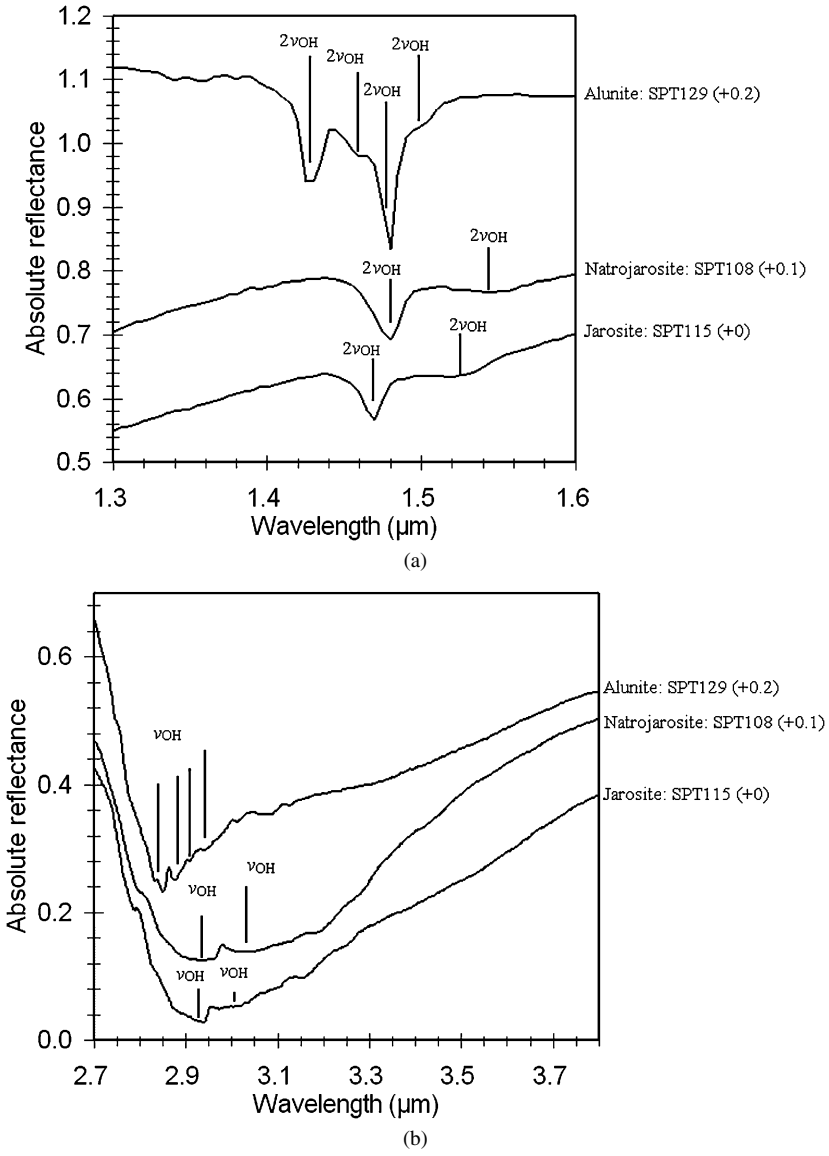

Fig. 8. 1.4 μm (a) and 3 μm (b) region spectra of some OH-bearing sulfates. Numbers in brackets indicate linear vertical offset applied to the spectra for clarity.

the H_2O-bearing/OH-free spectra, while a single narrow (and asymmetric) absorption band is seen in the OH-bearing/H_2O-free sample spectra. The H_2O- and OH-bearing sample spectra exhibit up to three absorption bands in this region.

The H_2O-bearing sulfates generally exhibit an absorption band in the 11–13 μm (770–910 cm^{-1}) region attributable to H–O–H rotation (Ross, 1974) (Tables 6 and 7). In our reflectance spectra, this feature is not always apparent, sometimes appearing as an inflection on the short wavelength wing of a longer wavelength ν_4 S–O bend. The second-order overtone of this band, combined with the H–O–H stretching fundamental in the 3 μm region (~3300 cm^{-1}) will yield an absorption band in the 1.8 μm region. Such a feature is consistent with similar bands attributable to OH combinations in the OH-bearing sulfates (e.g., Bishop and Murad, 2005).

The 1.4 μm region is expected to exhibit absorption bands attributable to H–O–H bending plus stretching bands, combinations and overtones of the H_2O stretching bands, and overtones of the O–H stretch. As expected, this wavelength region shows complex behavior. In some cases strong bands are expected on the basis of high water content (e.g., romerite (SPT110), voltaite (SPT111) amarantite (SPT112)) but are weak or absent (Fig. 1). These spectrally anomalous samples may be the result of dehydration, although spectra of water-bearing samples common to this study and Crowley et al. (2003) are very similar, in spite of differences in sample preparation, storage, and spectral acquisition methods. The amount of spectral detail in the 1.4 μm region ranges from virtually non-existent (e.g., romerite (SPT110)) to spectra showing a number of well-resolved absorption features (e.g., gypsum (SPT127)) (Fig. 1). These differences are attributable to variations in the number of distinct crystallographic sites available to water molecules, as well as the degree of hydrogen bonding (Buijs and Choppin, 1964; Clark, 1981). Utilizing band positions in the 1.4, 1.9, and 6 μm regions provides good discrimination of members of this group.

Table 8
Wavelength positions (in μm) of minima of H_2O- and OH-associated absorption bands in the 1.4 and 1.9 μm regions

Mineral	OH stretching overtones (1.4 μm region)	H_2O overtones/combinations (1.4 μm region)	H_2O combinations (1.9 μm region)
H_2O- and OH-free			
Anhydrite[4]	–	–	–
Anglesite[5]	–	–	–
Barite[5]	–	–	–
OH-bearing			
Jarosite[4]	1.465–1.468, 1.51–1.52	–	–
Natrojarosite[4]	1.477–1.48, 1.541–1.546	–	–
Alunite[4]	1.425, 1.46[a], 1.467, 1.50[a]	–	–
H_2O-bearing			
Kieserite[5]	–	1.461, 1.53[a]	1.974, 2.06[c], 2.13[b]
Szomolnokite[5]	–	–	1.98[b]
Voltaite[5]	–	1.456	1.939, 2.011
Rhomboclase[4]	–	∼1.5[a,b]	2.02, 2.07[a]
Gypsum[4]	–	1.39[a], 1.449, 1.488, 1.534	1.944, 1.97[a]
Amarantite[3]	–	1.44[b], 1.48[b]	1.941, 1.978
Coquimbite[2]	–	1.412, 1.48[a]	1.911, 1.984
Romerite[2]	–	–	2.0[a]
Rozenite[2]	–	1.450, 1.5[a]	1.95, 1.98
Hexahydrite[1]	–	1.441, 1.46[a]	1.938, 1.97[a]
Pickeringite[2]	–	1.44[a]	1.942, 2.05[a]
H_2O- and OH-bearing			
Hydronium jarosite[4]	–	–	1.93[b]
Sideronatrite[3]	1.39[a], 1.475	1.418, 1.434, 1.552	1.867, 1.918, 1.990
Ferricopiapite[3]	–	1.453, 1.5[b]	1.943, 1.98[a]
Copiapite[3]	1.36	1.452, 1.48[a]	1.940, 2.0[a]
Botryogen[3]	1.39, 1.448	1.474	1.932, 1.96[a]
Fibroferrite[3]	1.37[b], 1.43[a]	1.490	1.934

Note. Absorption bands that are not integral to the mineral (e.g., due to adsorbed water), but may be present in the spectra, have been omitted.
[a] Shoulder on a more intense absorption band, wavelength position approximate.
[b] Broad band, wavelength position approximate.
[c] Identity as H_2O band uncertain.
[1] Structure consists of isolated SO_4 tetrahedra.
[2] Structure consists of finite clusters of polyhedra.
[3] Structure consists of infinite chains.
[4] Structure consists of infinite sheets.
[5] Structure consists of infinite framework.

The spectra of the OH- and H_2O-bearing group are more difficult to analyze because spectral contributions from both OH and H_2O are expected. All of the spectra in this group have some features in common. All exhibit two or more H–O–H bending fundamentals in the 6 μm region (Table 7). All show some structure in the 3 μm region, consistent with contributions from both OH and H_2O. Assignments in the 3 μm region are made largely on the basis of comparisons to the OH- or H_2O-bearing samples described above. Because minerals in this group have lower OH:SO_4 ratios per unit cell than the OH-bearing group (Table 1), OH-associated absorption bands in the 1.4 μm region are weaker and often poorly resolved. In all cases, the 1.4 μm region exhibits at least two partially resolvable absorption features, attributable to OH and H_2O.

While some absorption band assignments for this latter group are tentative, measurable differences exist between all the sulfates included in this study. Restricting ourselves to OH- and H_2O-associated absorption bands for the moment, absorption band positions in the 1.4, 1.9, and 6 μm regions, in particular, are useful for discriminating different sulfates. The 3 μm region, which can contain contributions from both OH and H_2O, is generally less diagnostic.

5.4. Christiansen feature and Restrahlen band

Sulfate reflectance spectra can exhibit a region of low reflectance (high emittance) near 8 μm (1250 cm^{-1}), termed the Christiansen feature. This reflectance minimum occurs where the real part of the index of refraction approaches that of the surrounding medium, resulting in minimal scattering (Conel, 1969; Salisbury, 1993). The Christiansen feature generally occurs at slightly shorter wavelengths than the fundamental molecular vibration, and its wavelength position varies for different sulfates (Bishop and Murad, 1996). Sulfate reflectance spectra may also exhibit a region of high reflectance near 9 μm (1100 cm^{-1}), termed a Restrahlen peak. This peak arises from strong mirror-like first surface reflections from mineral grains in regions of high absorbance (Salisbury, 1993). In sulfates,

Table 9
Wavelength positions of minima of absorption bands in the 1.62–1.87 μm and 2.0–2.7 μm regions that are attributable to combinations of OH- or H_2O-bending, stretching, and rotational fundamentals or S–O bending overtones

Mineral	Absorption band minimum wavelength position (μm)	
	1.7–1.8 μm region	2.0–2.7 μm region
H_2O- and OH-free		
Anhydrite[4]	–	–
Anglesite[5]	–	–
Barite[5]	–	–
OH-bearing		
Jarosite[4]	1.84–1.85	2.08[b,A], 2.21[B], 2.27[B], 2.30[C], 2.41[C], 2.46[C], 2.51[B], 2.59[b,B], 2.61[B]
Natrojarosite[4]	1.85–1.86	2.07[b,A], 2.23[b,B], 2.27[B], 2.30[b,C], 2.42[C], 2.46[C], 2.52[B], 2.61[B]
Alunite[4]	1.777	2.07[b,D], 2.16[B], 2.18[B], 2.21[B], 2.32[C], 2.40[b,C], 2.42[C], 2.48[B], 2.51[B], 2.56[B], 2.68[E]
H_2O-bearing		
Kieserite[5]	1.75[c]	2.13[c,F], 2.42[b,C], 2.55[B]
Szomolnokite[5]	–	2.10[c,F], 2.41[a,b,C], 2.55[B]
Voltaite[5]	1.8[c]	2.55[b,B]
Rhomboclase[4]	1.8[a,b]	2.45[b,C], 2.58[b,B]
Gypsum[4]	1.751, 1.78[b]	2.17[C], 2.22[C], 2.28[C], 2.43[b,A], 2.48[A], 2.55[b,B]
Amarantite[3]	1.78[a,b]	2.55[b,B]
Coquimbite[2]	1.75[a,b]	2.1[b,F], 2.55[b,B]
Romerite[2]	1.75[a,b]	2.10[F], 2.40[C], 2.60[B]
Rozenite[2]	1.75[a]	2.44[b,C], 2.53[B]
Hexahydrite[1]	1.75[a]	2.45[b,C], 2.54[b,B]
Pickeringite[2]	1.75[a,b]	2.1[b,F], 2.55[b,B]
H_2O- and OH-bearing		
Hydronium jarosite[4]	–	2.28[c,B], 2.45[a,b,C], 2.6[a,b,B]
Sideronatrite[3]	1.748[a], 1.803[a]	2.09[A], 2.15[b,A], 2.18[A], 2.24[b,A], 2.28[B], 2.36[C], 2.43[b,A], 2.46[b,C], 2.50[B], 2.60[A], 2.68[a,b,E]
Ferricopiapite[3]	1.78[a,b]	2.41[b,A], 2.46[b,B], 2.55[b,B]
Copiapite[3]	1.78[a]	2.42[b,A], 2.47[b,B], 2.53[B]
Botryogen[3]	1.751[a], 1.811[a]	2.28[b,B], 2.43[b,A], 2.54[B]
Fibroferrite[3]	1.78[a]	2.40[a,b,A], 2.47[a,b,B], 2.55[b,B]

[a] Weak band, wavelength position approximate.
[b] Shoulder on a more intense absorption band, wavelength position approximate.
[c] Broad band, wavelength position approximate.
[1] Structure consists of isolated SO_4 tetrahedra.
[2] Structure consists of finite clusters of polyhedra.
[3] Structure consists of infinite chains.
[4] Structure consists of infinite sheets.
[5] Structure consists of infinite framework.
[A] $3\nu_3$ S–O.
[B] $\nu_{OH/H_2O} + \gamma/\delta_{OH/H_2O}$.
[C] $3\nu_3$ S–O or OH/H_2O combinations and/or overtones.
[D] 3 μm region ν_{OH/H_2O} stretch + 12 μm region OH/H_2O rotation.
[E] 3 μm region ν_{OH/H_2O} stretch + unspecified "lattice modes" near or beyond 25 μm.
[F] 3 μm region ν_1 or ν_3 H_2O stretch + 12 μm region H_2O rotation.

it occurs in the region of the sulfate-anion stretching fundamental near 9 μm (1100 cm^{-1}). The appearance of both the Christiansen feature and Restrahlen peak are very sensitive to grain size (e.g., Hanel et al., 1970; Salisbury and Walter, 1989)

Table 10
Wavelength positions of minima or maxima, as appropriate, for resolvable Christiansen features and Restrahlen peaks in sulfate spectra

Mineral	Christiansen feature (μm)	Restrahlen peak (μm)
Unconnected SO_4 groups		
Hexahydrite	7.9[a]	8.48[b]
Finite clusters of polyhedra		
Romerite	7.93	8.20[c]
Pickeringite	7.85	8.03[c]
Rozenite	8.25	8.60[b]
Coquimbite	8.02	8.32[b]
Infinite chains		
Fibroferrite	7.90	8.30[c]
Sideronatrite	7.91	8.12[c]
Botryogen	7.98	8.17[b]
Copiapite	7.87[c]	7.95[b,c]
Ferricopiapite	7.92	8.32[b]
Amarantite	8.30[a]	8.6[b,c]
Infinite sheets		
Alunite	7.60	7.80
Jarosite	8.0[c]	8.07[b,c]
Natrojarosite	7.95–8.0	8.05–8.20
Hydronium jarosite	7.40	8.0
Rhomboclase	7.73	8.40[b,c]
Gypsum	7.95	8.40
Anhydrite	7.75	8.2[a]
Infinite frameworks		
Kieserite	7.83[c]	7.94[b,c]
Szomolnokite	7.90	8.15[b,c]
Voltaite	7.9[a]	8.45[b,c]
Barite	7.87	8.11[b]
Anglesite	8.05	8.30[b,c]

Note. Samples have been sorted by structural groups.
[a] Broad band, wavelength position approximate.
[b] Not the highest peak in the 8–10 μm region.
[c] Weak band.

and other factors, such as cementation (Cooper and Mustard, 2002).

Cooper and Mustard (2002) noted the presence of a Christiansen feature and Restrahlen band in reflectance spectra of $MgSO_4$ cements. In the current spectral suite (all <45 μm size powders), clearly defined Christiansen features and Restrahlen bands are present in approximately half of the spectra. In the remaining cases, either an absorption feature in the 8 μm (1250 cm^{-1}) region is not the band with the lowest reflectance and/or the Restrahlen band is not the most prominent reflectance peak. Wavelength positions for these features for the current spectral suite are summarized in Table 10. There is no systematic trend to the data in terms of structural types, and given the various factors that can affect these features (Conel, 1969; Mustard and Hays, 1997), its utility for remote sensing applications may be limited.

5.5. SO_4 fundamental stretching and bending

The SO_4^{2-} group in sulfates can exhibit four infrared-active vibrational modes: an A_1 symmetric stretch (ν_1), an E sym-

metric bend (ν_2), an F asymmetric bend (ν_3), and an F symmetric bend (ν_4) (Ross, 1974; Minenyi, 2000). These absorption bands generally occur in the following intervals: ν_1 at 9.6–10.4 μm (960–1040 cm^{-1}) (normally one or two bands); ν_2 at 19–24 μm (420–525 cm^{-1}) (normally one or two bands); ν_3 at 7.8–10.4 μm (960–1280 cm^{-1}) (normally between two and four bands); and ν_4 at 13–18 μm (550–770 cm^{-1}) (normally between two and four bands) (Ross, 1974; Brady et al., 1986; Bigham et al., 1994). These assignments are consistent for a large number of sulfates (e.g., Omori and Kerr, 1963; Hovis, 1966; Townsend, 1987; Bigham et al., 1990, 1994; Roush, 1996; Bishop and Murad, 2005). Combinations and overtones of these bands are most prominent in the 4–5 μm region (Khanna et al., 1988; Cooper and Mustard, 2002). Once again, the appearance of these bands is sensitive to factors such as grain size (e.g., Hanel et al., 1970; Salisbury and Walter, 1989).

Multiple fundamental absorption bands can occur if the symmetry of an SO_4 group is distorted, leading to differences in S–O bond lengths and consequent energy-level splitting (Hass and Sutherland, 1956; Adler and Kerr, 1965; Ross, 1974; Powers et al., 1975; Bigham et al., 1994; Lane and Christensen, 1998). In addition, the types of cations that may be present, and the nature of any hydrogen bonding, can shift the position of these bands (Freedman and Straughan, 1971). There seems to be no strong correlation between positions of these bands and cation type (Minenyi, 2000), or with the presence or absence of OH/H_2O and additional anions (Lane, 2004).

Transmission spectral studies indicate that the ν_1 symmetric stretch is weak in almost all sulfate spectra (e.g., Ross, 1974). The ν_2 symmetric bends are also generally weak. This is due to the fact that these modes are normally infrared inactive. The strongest absorption bands are those associated with the ν_3 asymmetric bend and the ν_4 symmetric stretch. Emission spectra of a number of sulfates (Lane, 2004; Lane et al., 2004; Bishop et al., 2005a) show a variety of spectral forms. Anhydrous-sulfate spectra are dominated by ν_3 and ν_4 S–O bands. Anhydrous sulfates with additional anions, hydrous sulfates, and hydrous sulfates with additional anions generally exhibit shallower ν_4 S–O bands compared to the ν_3 S–O bands.

5.5.1. The ν_3 bending region: 7.8–10.4 μm

The 7.8–10.4 μm region of all the sulfate spectra exhibits at least two resolvable absorption bands (Table 11). The appearance of absorption features in this region ranges from a series of narrow and well-resolved absorption bands (e.g., coquimbite, jarosite) to highly overlapped absorption bands, resulting in a region of overall low reflectance with little or no spectral structure (e.g., fibroferrite, amarantite) (Fig. 9). The number and wavelength positions of these bands have no apparent correlation with structural group or composition, such as the type of major cations, or the presence or absence of H_2O or OH.

5.5.2. The ν_1 stretching region: 9.6–10.4 μm (960–1040 cm^{-1})

Assigning absorption bands to this mechanism is complicated by the fact that ν_1 SO bands are generally weak and may overlap the region occupied by ν_3 bending vibrations. The ν_1 bands are generally narrower than ν_3 bands, and a number of the spectra show no clear evidence for absorption bands in this wavelength region. Possible ν_1 SO bands are listed in Table 12. Band assignments generally agree with those of Ross (1974). In general, ν_1 bands are absent or weakest in the sulfates composed of infinite chains and are strongest in the anhydrous samples.

5.5.3. The ν_4 bending region: 13–18 μm (550–770 cm^{-1})

Absorption bands in this wavelength region range from a series of narrow, well-resolved bands to a broad unresolved feature, likely due to overlapping bands. The wavelength position of the shortest wavelength absorption band in this region generally increases as the structure becomes more condensed, proceeding from isolated SO_4 groups to infinite frameworks, however a more precise correlation could not be derived (Table 11). Absorption bands also generally become better resolved as the structure becomes more complex: the most well-resolved absorption bands in this region are found for the infinite sheet and infinite framework and anhydrous species (Fig. 10). Species that contain different cations, but which are otherwise compositionally and structurally identical (e.g., barite versus anglesite, jarosite versus natrojarosite), as well as hydrous versus anhydrous, but otherwise compositionally identical species (e.g., anhydrite versus gypsum), exhibit measurable differences in band position (Table 11). No systematic variations were found between band position and compositional or structural parameters. These general observations are consistent with those found by other investigators (e.g., Lane, 2004).

5.5.4. The ν_2 bending region: 19–24 μm (420–525 cm^{-1})

The 19–24 μm (420–525 cm^{-1}) region is expected to exhibit absorption bands attributable to ν_2 bending vibrations. In transmission spectra, these absorption bands are frequently weak and poorly resolved (Ross, 1974). Possible ν_2 absorption band assignments have been compiled in Table 12. These assignments draw heavily on previous studies (Ross, 1974) because the shapes of presumed ν_2 bands are very variable and most are expected to be weak. From the limited data and uncertainties in assignment, no useful conclusions can be drawn on the utility of these bands for spectral characterization and discrimination of sulfates.

5.5.5. SO_4 overtone and combination bands: 4–5 μm (2000–2500 cm^{-1}) region

All of the sulfate spectra exhibit absorption features in the 4–5 μm (2000–2500 cm^{-1}) region that are attributable to first-order overtones and combinations of the ν_3 absorptions in the 7.8–10.4 μm (960–1280 cm^{-1}) region. The overall shapes, and number of bands in the 4–5 μm region follows that of the 7.8–10.4 μm region (Fig. 11). These features range from a barely discernible broad region of absorption (e.g., amarantite, rhomboclase) to intense and well-resolved absorption bands (e.g., anhydrite, jarosite). Wavelength positions of absorption bands in this wavelength region are provided in Table 13. There is enough variability in absorption band positions in this wave-

Table 11
Wavelength positions (in μm) of minima of ν_3 and ν_4 SO_4-associated fundamental absorption bands in the 7.8–10.4 and 13–18 μm regions, respectively

Mineral	ν_3 SO_4 bend (7.8–10.4 μm region)	ν_4 SO_4 bend (13–18 μm region)
Unconnected SO_4 groups		
Hexahydrite	8.3[a], 8.9[a,b], 9.2[a,b], 9.8[b]	**14.4**[b], 15.4[a], 17.1[b], 18.0
Finite clusters of polyhedra		
Romerite[e]	7.85–7.95, 8.6[b], 8.9[b], 9.3[b],10.1[b,c]	**15.0**, **15.95**, 16.4–16.6, 17.6[c], 18.0–18.2
Pickeringite	8.2[b], 8.6[a,b], 9.1, 10.1, 10.4[a]	**14.6–14.8**[b], 15.4–15.6, 15.7–15.8[a], 16.0, 16.4
Rozenite	**8.25**, 8.7[a], 9.3[b]	13.7[a], **14.6**, **15.0**
Coquimbite[e]	8.45[a], **8.7–8.8**, 9.5[a], **9.75–9.85**[d], 10.55	**14.2–14.5**, 14.7–14.9, **16.2–16.3**, 16.6[a], 17.3–17.4
Infinite chains		
Fibroferrite	8.45, 9.1[b], 9.6[b], 9.8[a,b]	14.6, 15.6[a,b], **16.5**, 16.8[a,b]
Sideronatrite	8.27, 8.4[a], **8.52**, 8.7[a], 8.8, **8.91** 9.1[a], **9.58**, 9.8[a], **9.68**, 9.97[a], 10.45	14.8[a], **15.2**, 16.0, 16.4, 16.9, 17.8[a]
Botryogen	**8.37**, 8.7[a], 9.25, 9.5, 9.85	**14.4**, 15.9, 16.9[a], 17.7
Copiapite[e]	8.07, 8.47, 8.75[c], 9.25[a], 9.7, 9.8	14.7[b], **15.6**, 16.0[a], 16.5[a], 17.2[a]
Ferricopiapite	8.45[b], 8.55[b], 9.20, 9.85[a], 10.08[a], 10.2[a]	15.0[a,b], **15.8**, 16.6[a], 17.4[a]
Amarantite	8.3[b], 8.9[b], 9.2[b,c], 9.7	14.4[a], **14.8**, 15.2[a]
Infinite sheets		
Alunite	**8.10**, 8.65, 9.2[a], 9.40, 10.15[c], 10.6[c]	**15.3**, **16.3**, 17.4
Jarosite[e]	8.0[b], **8.5–8.6**, 9.1[a], **9.4**, 10.1–10.2	**14.6–14.7**, **16.2**, 16.5–16.6[a]
Natrojarosite[e]	7.95, 8.55, 9.2[a], **9.4**, **10.0–10.1**	**14.4–14.5**, **16.0–16.1**, **16.7–16.8**
Hydronium jarosite	8.40[a], **8.65**, 9.1[b], 9.5[a], 9.6, 9.8[b]	**14.4**, 14.8[a], 15.2[c], 16.0[b], 17.0[a]
Rhomboclase	8.62, 9.48, 10.3[b]	**14.8**, 15.8, 16.5, 17.4
Gypsum	8.7[a], **9.2**[b]	**14.2**[d], 15.2[a], **15.9–16.1**[d], 17.4[b], 17.8[a]
Anhydrite	8.6[a], 8.9[a], **9.15**, 9.5[b], 10.25[c], 10.5[b,c]	**14.1–14.3**[d], 14.9–15.1[a], **15.8–16.1**, **16.4–16.6**, 16.9–17.0
Infinite frameworks		
Kieserite	**8.23**, 8.35[a], 8.65[d], 8.85[a], 9.0[a], 9.11, 9.25[a], **9.57**, 9.95[a]	**14.7**, 14.9[a], 15.2[a], 15.7[a], **15.9**
Szomolnokite	8.6[b], 9.0[b], 9.2[b]	14.5[a], **15.0**, **15.9**, 16.5, 17.7[b]
Voltaite	8.6[b,c], 9.1[b,c], 9.4[b,c]	**15.1**, **15.8**[b], 16.8
Barite	8.20[a], **8.36**, 9.25[a], **9.46**, 10.4[a]	14.3[a,b], **15.3**, **15.9**, **16.7**, 17.9[a]
Anglesite	**8.04**, **8.52**, 9.90[b]	15.1[a], **15.5**, **16.2**, **17.1**

Note. Some bands may overlap or duplicate the Christiansen bands listed in Table 10. The most well-resolved and intense absorption bands are indicated in bold face type.

[a] Shoulder on a more intense absorption band, wavelength position approximate.
[b] Broad band, wavelength position approximate.
[c] Weak band.
[d] Asymmetric absorption feature, may be composed of overlapping bands.
[e] Band shapes vary for different spectra of this mineral.

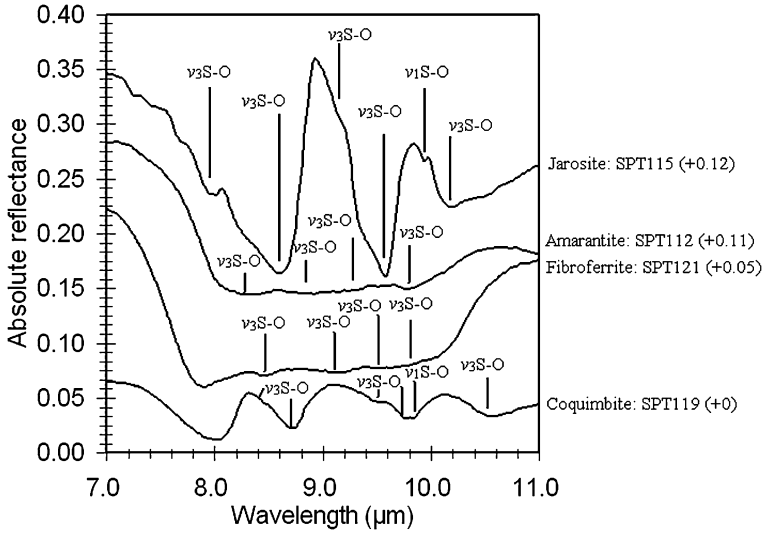

Fig. 9. S–O ν_3 bending region (7–10 μm) spectra of selected sulfates. Numbers in brackets indicate linear vertical offset applied to the spectra for clarity.

Table 12
Wavelength positions (in μm) of minima of ν_1 and ν_2 SO_4-associated fundamental absorption bands in the 9.6–10.4 and 19–24 μm regions, respectively

Mineral	ν_1 SO_4 stretch (9.6–10.4 μm region)	ν_2 SO_4 bend (19–24 μm region)
Unconnected SO_4 groups		
Hexahydrite	10.02	23.4[a]
Finite clusters of polyhedra		
Romerite[e]	9.82	23.1, 24.0
Pickeringite	9.57	23.4[b]
Rozenite	10.11	23.7[g]
Coquimbite[e]	9.8[d]	19.9–20.4[b], 22.3–22.5[b]
Infinite chains		
Fibroferrite	–	–[g]
Sideronatrite	10.1[c]	21.0[b], 23.2[b]
Botryogen	10.2[a,c]	24.1[g]
Copiapite[e]	–	21.1, 23.5[g]
Ferricopiapite	–	23.5[g]
Amarantite	–	20.3[f], 21.0, 24.5[e]
Infinite sheets		
Alunite	9.78[d]	20.5, 22.2, 23.5
Jarosite[e]	9.92	20.5–20.6[h], 22.3, 23.5, 24.2
Natrojarosite[e]	9.90	20.4[h], 22.3
Hydronium jarosite	10.0[b,d]	23.7[c]
Rhomboclase	9.74	23.1, 23.7[g]
Gypsum	9.97	23.3, 24.1
Anhydrite	9.88	19.6
Infinite frameworks		
Kieserite	9.78[d]	22.6, 24.0[g]
Szomolnokite	9.82	23.4
Voltaite	9.87[d]	23.5, 24.0
Barite	10.18	21.2
Anglesite	10.33	21.6, 22.9

[a] Shoulder on a more intense absorption band, wavelength position approximate.
[b] Broad band, wavelength position approximate.
[c] Weak band.
[d] Assignment to ν_1 uncertain; may be a ν_3 SO_4 absorption feature.
[e] Additional band detected in transmission spectra (Ross, 1974) could not be reliably located in reflectance spectrum.
[f] Band detected in transmission spectra (Ross, 1974) could not be reliably located in reflectance spectrum.
[g] Multiple absorption bands or only weak bands present in 20–25 μm region, consequently reliable assignment to ν_2 could not be made.
[h] May be OH bending band (Ross, 1974).

length region to allow a number of sulfate minerals to be discriminated.

5.6. 2.1–2.7 μm region

The 2.1–2.7 μm region of the sulfate spectra exhibits a diversity of spectral types with variable numbers of resolvable absorption bands (Table 9). Various band assignments have been proposed for a few sulfate minerals in this wavelength region (e.g., Hunt et al., 1971; Clark et al., 1990). Examination of the full spectral data set and previous investigations (e.g., Bishop and Murad, 2005) suggest that absorption bands in this region may be attributable to multiple causes, primarily

Table 13
Wavelength positions of minima of SO_4-associated overtone and combination absorption bands in the 3.8–5.2 μm region

Mineral	Absorption band minimum wavelength positions (μm)
Isolated SO_4 clusters	
Hexahydrite	4.46[b], 4.60[b], 4.8[b], 5.0[a,b]
Finite clusters of polyhedra	
Romerite	4.23[c], 4.32[c], 4.50[a], 4.58[c], 4.80[c], 4.92[c]
Pickeringite	4.0[c], 4.8[a,b]
Rozenite	4.20[a], 4.30[a,] 4.38[b], 4.46[b], 4.68, 4.80[b], 4.92[b]
Coquimbite	3.87[b], 4.0[b], 4.50[a], 4.75[a], 4.92
Infinite chains	
Fibroferrite	4.28[b], 4.45[b], 4.7[b], 4.9[b], 5.0[b]
Sideronatrite	4.03, 4.10, 4.17, 4.26[a], 4.32, 4.41[a], 4.46[a], 4.49, 4.55, 4.68, 4.74[a], 4.83, 4.88, 4.93, 4.98, 5.03, 5.08[a]
Botryogen	4.27[c], 4.46[c], 4.59[b], 4.65[b], 4.83[a], 5.03[a]
Copiapite	4.1[c], 4.45[c], 4.6[b], 4.93[b], 5.02[a]
Ferricopiapite	4.1[c], 4.5[c], 4.88[c]
Amarantite	4.1–5.0[c]
Infinite sheets	
Alunite	4.15[c], 4.28[a], 4.36, 4.43[a], 4.50, 4.55[a], 4.60, 4.67[a], 4.73, 4.81, 4.87[a]
Jarosite	3.98, 4.30, 4.59, 4.75, 4.81, 4.95, 5.10
Natrojarosite	4.00, 4.31, 4.56, 4.63[a], 4.69[a], 4.72, 4.78, 4.89, 5.03
Hydronium jarosite	4.50[b], 4.70[b], 4.94[a], 5.01, 5.08[a], 5.15[a]
Rhomboclase	4.1–5.0[c]
Gypsum	4.33[a], 4.46, 4.53[a], 4.67[a], 4.73, 4.98
Anhydrite	4.20[a], 4.28[a], 4.34, 4.38[a], 4.47, 4.55[a], 4.60[a], 4.68[a], 4.70, 4.93
Infinite frameworks	
Kieserite	4.25[a], 4.40[a], 4.46[a], 4.53, 4.68, 4.81,4.95[a]
Szomolnokite	4.32, 4.50[a,c], 4.58[c], 4.70[c], 4.82[b], 4.94[c], 5.00[c]
Voltaite	4.0–5.0[c]
Barite	4.26[a], 4.29, 4.38[a], 4.46[a], 4.56, 4.62, 4.68, 4.71[a], 4.78, 4.84, 4.89, 5.10
Anglesite	4.3[a], 4.73, 4.97, 5.16

[a] Shoulder on a more intense absorption band, wavelength position approximate.
[b] Broad, weak band, wavelength position approximate.
[c] Broad band (may consist of multiple overlapped bands, wavelength position approximate).

S–O vibrational overtones, as well as H–O–H/O–H combinations and overtones. Detailed spectra of some sulfates that exhibit absorption bands in the 2.1–2.7 μm region are shown in Fig. 12. Resonances and other perturbations of the fundamental absorption bands in sulfates complicate definitive assignments of combination and overtone bands (Breitinger et al., 1999; Bishop and Murad, 2005).

This wavelength region is essentially featureless for the anhydrous species. The H_2O-bearing sample spectra all exhibit an absorption band near 2.55 μm. The intensity of this band decreases when sulfate-bearing samples are measured under low atmospheric pressure (Bishop and Pieters, 1995), when hydrous sulfates are heated (Hunt et al., 1971), and with decreasing H_2O content (Dalton, 2003), suggesting that it is related to OH/H_2O content. A comparable absorption band is present in water spectra (Bayly et al., 1963) and has been assigned to a combination of the H_2O asymmetric stretch (ν_3) and rotational (υ_L) fundamental that occurs near 20 μm (Bayly et al., 1963).

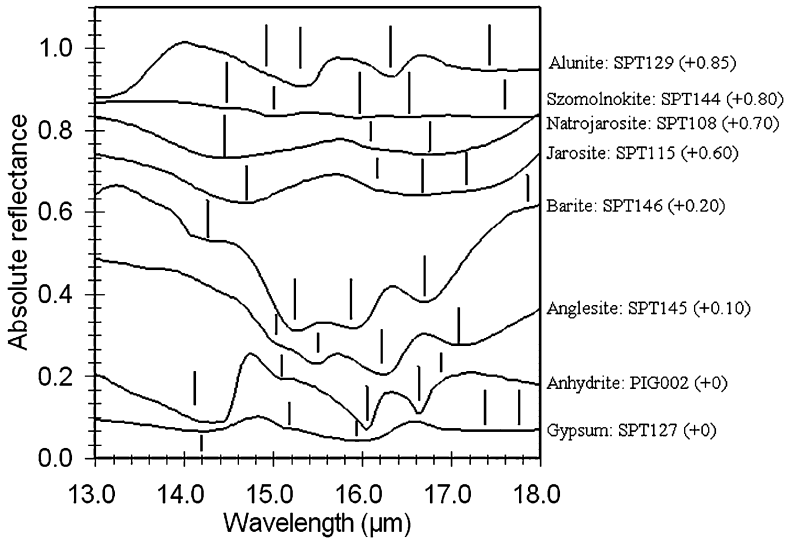

Fig. 10. S–O ν_4 bending region (13–18 μm) spectra of selected sulfates. Numbers in brackets indicate linear vertical offset applied to the spectra for clarity. Vertical bars indicate positions of S–O ν_4 absorptions.

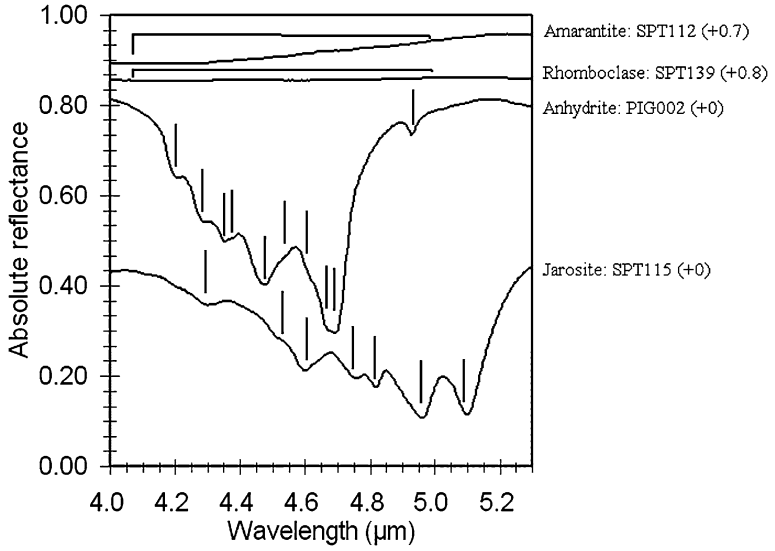

Fig. 11. S–O overtone/combination region (4–5.3 μm) spectra of selected sulfates. Numbers in brackets indicate linear vertical offset applied to the spectra for clarity. Vertical bars indicate location of absorption bands.

In sulfates, this band was assigned to a combination of low frequency rotational/translational OH/H_2O lattice modes located near 20 μm (500 cm^{-1}) and OH stretching fundamentals near 2.86 μm (Hunt et al., 1971; Bishop and Murad, 2005). All of the H_2O- and OH-bearing sulfate spectra exhibit some evidence of an absorption feature in the 20 μm (500 cm^{-1}) region, suggesting that this assignment is correct.

Some of the H_2O-bearing spectra (particularly szomolnokite, kieserite, coquimbite, and romerite) exhibit a generally weak and broad absorption band near 2.1 μm (Fig. 12, Table 9). The appearance of this band correlates with the appearance of the H–O–H rotational absorption band near 12 μm (830 cm^{-1}). It is assigned to a combination of the ν_3 H_2O stretching fundamental in the 3 μm region plus the H_2O rotation band located near 12 μm (830 cm^{-1}) consistent with the appearance of a similar band in OH-bearing sulfates (Bishop and Murad, 2005). It should be noted however that the assignment of the 12 μm band is not well constrained in some cases (Ross, 1974).

A number of the OH- and/or H_2O-bearing spectra also exhibit additional absorption bands in the 2.1–2.7 μm region. Bands in this region can be assigned to a number of mechanisms, including ν_{OH} or ν_{H_2O} stretches in the 3 μm region plus various OH/H_2O translations/rotations, or overtones of S–O stretches (Bishop and Murad, 2005) (Table 9). Some of these assignments are at odds with previous assignments. For example, Hunt et al. (1971) assigned a group of bands located between 2.2 and 2.27 μm in gypsum to combinations of stretching and rotational/translational H_2O fundamentals and overtones, whereas we assign these features to S–O bending overtones, as the fundamental S–O bands are particularly intense and located at the expected wavelength positions to account for the 2.17, 2.22, and 2.28 μm bands. For alunite, Hunt et al. (1971) as-

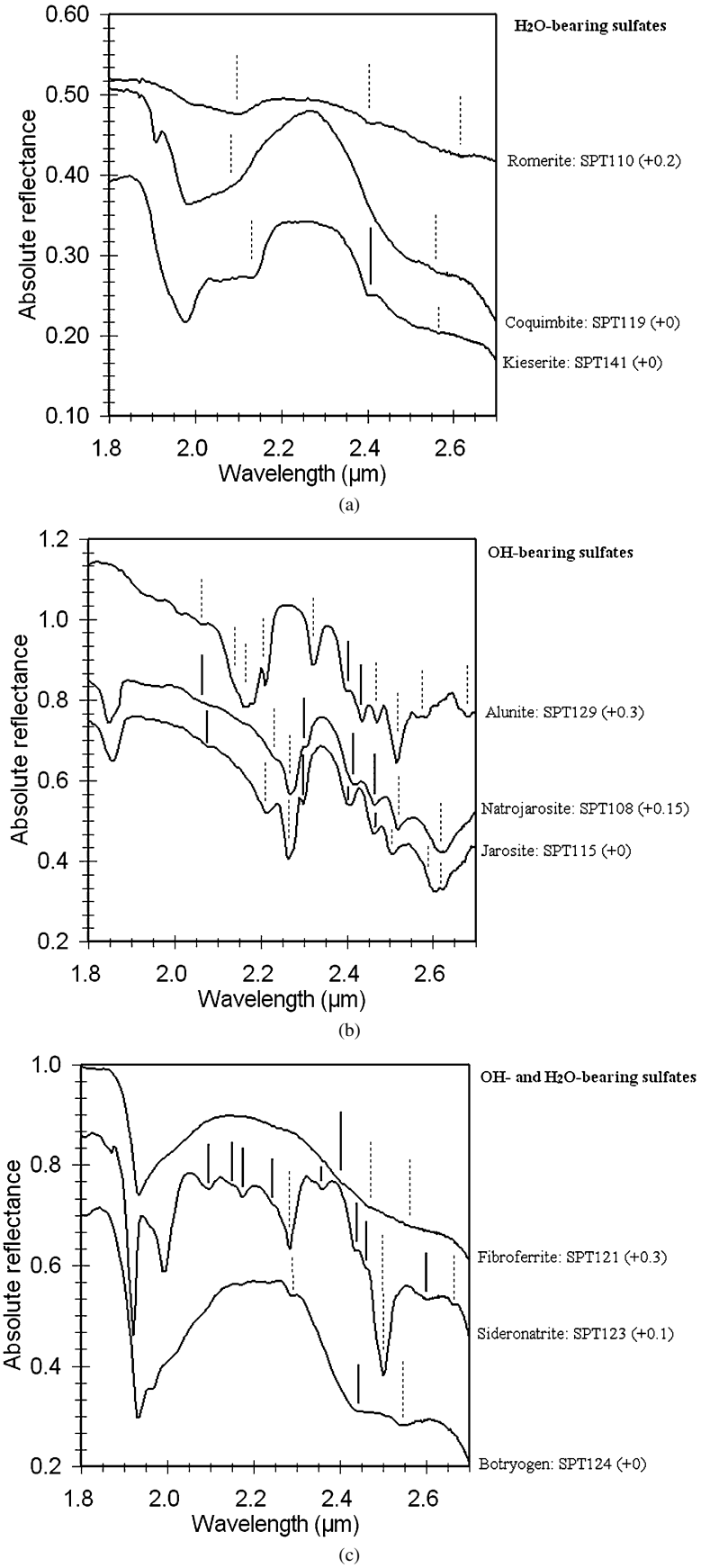

Fig. 12. 1.8–2.7 μm region spectra of selected sulfates. (a) H_2O-bearing samples; (b) OH-bearing samples; (c) H_2O- and OH-bearing samples. Numbers in brackets indicate linear vertical offset applied to the spectra for clarity. Dashed lines: OH- or H_2O-related absorption bands; solid lines: SO related absorption bands. See Table 9 for details.

signed the absorption band at 2.33 μm to a combination of the fundamental Al–O–H bend (located near 9.52 μm (1050 cm^{-1})) and the lowest frequency OH stretching fundamental, whereas our assignment is more general (ν_{OH} stretch plus γ OH out-of-plane bend) and in agreement with Bishop and Murad (2005). For jarosite, Clark et al. (1990) assigned the absorption band near 2.27 μm to a combination of an OH stretch and Fe–OH bend; our assignment involves a ν_{OH} stretch plus a γ OH out-of-plane bend (Bishop and Murad, 2005).

The OH- and H_2O-bearing sulfates exhibit behavior in the 2.1–2.7 μm region consistent with OH-bearing samples, H_2O-bearing samples, or a combination of both (Table 9). In general, we see that H_2O-bearing/OH-free sulfates exhibit broad, weak absorptions in the 2.1–2.7 μm region, largely attributable to H_2O combinations/overtones, or S–O stretching overtones. In the case of OH-bearing/H_2O-free sulfates, absorption bands in this region are more numerous and are largely attributable to OH combinations/overtones or S–O bending overtones (Bishop and Murad, 2005). For OH- and H_2O-bearing sulfates, the appearance of both H_2O- and OH-associated absorption bands, as well as S–O bending overtones is possible. In general, OH-associated absorption bands are deeper and narrower than H_2O-associated absorption bands.

5.7. Additional absorption bands: 20–25 μm (400–500 cm^{-1})

In addition to the absorption bands identified in the 20–25 μm (400–500 cm^{-1}) region attributable to ν_2 S–O bending and OH/H_2O rotational vibrations, most of the sulfate reflectance spectra exhibit additional absorption bands in this wavelength region for which assignments are unknown or uncertain. Possible assignments include M–OH stretches, additional ν_2 S–O bending, or OH translations (Powers et al., 1975; Ross, 1974). In this wavelength region, small changes in activation energy due to even slight changes in structure will translate into large changes in band wavelength position. The current data do not provide any reliable insights into the causes of these absorption bands. As an example of this uncertainty, an absorption band near 19.5 μm (515 cm^{-1}) in jarosite is variously assigned to an M–OH bend (Ross, 1974) or an $[FeO]_6$ vibration (Powers et al., 1975).

6. Discussion

The current sulfate sample suite is sufficiently diverse to provide insights into some of the causes of spectral variability within the sulfate group. The effects of cation substitutions, changes in H_2O content, variability for a single mineral, and spectrum-altering effects of accessory phases can all be addressed with this sample suite.

6.1. Spectral variability

Our ability to discriminate individual absorption bands varies as a function of many factors, including changes in adjacent band depths. As an example of the effects of overlapping absorption bands, Dalton (2003) measured the reflectance spectra of a series of progressively hydrated magnesium sulfates ($MgSO_4{\cdot}nH_2O$, where n varies from 0 to 7). The 0.95, 1.2, and 1.4–1.5 μm regions all seem to exhibit the same number of absorption bands, although as water content increases, individual bands become less resolvable, gradually merging into broader regions of low reflectance and decreasing spectral structure. A well-resolved absorption feature near 2.39 μm in the H_2O-poor sample spectra gradually transforms into an inflection point on the short wavelength wing of the major H_2O absorption band located near 2.9 μm as H_2O content increases. These spectral changes cannot be related solely to variations in H_2O content because all these structures are different, varying from a framework ($n = 0$) to unconnected polyhedra ($n = 6, 7$).

Jarosite and natrojarosite reflectance spectra measured by other investigators (e.g., Townsend, 1987; Clark et al., 1990; Grove et al., 1992; Morris et al., 2000; Bishop and Murad, 2005) are broadly consistent with the current results. However, differences often exist, particularly in terms of the widths and depths of the various absorption bands. These differences are likely due to factors such as purity of the samples, grain size, and degree of crystallinity, as well as the effect of Na and K substitutions.

6.2. Effect of cation substitutions

Isomorphous substitutions are common in sulfate minerals. In the current sample suite, the spectrum-altering effects of cation substitutions can be assessed by comparing barite to anglesite (Ba–Pb substitution), alunite to jarosite (Al–Fe^{3+} substitution), jarosite to natrojarosite to hydronium jarosite (K–Na–H_3O substitution), copiapite to ferricopiapite (Fe^{2+}–Fe^{3+} substitution), and kieserite to szomolnokite (Mg–Fe^{2+} substitution). In the case of barite–anglesite–anhydrite, the presence of the smaller Ca cation as opposed to Ba in barite and Pb in anglesite, results in a structural change.

6.2.1. Barite–anglesite–anhydrite

For barite versus anglesite, the presence of Ba or Pb in these anhydrous sulfates results in changes in unit cell dimensions but not structure (Hawthorne et al., 2000). Spectrally, these differences are manifested as differences of up to 400 nm in the positions of the S–O fundamental bending and stretching, and overtone and combination bands and variations in the number of resolvable absorption bands (Tables 11–13). The spectral differences are related to changes in S–O bond lengths due to differences in cation size and charge density. For barite–anglesite–anhydrite, anhydrite is not isostructural with barite or anglesite, due to the smaller size of the Ca cation. This results in changes in wavelength positions of all the S–O bands, as expected (Tables 11–13, Figs. 2–3).

6.2.2. Jarosite–natrojarosite

The jarosite–natrojarosite series includes six samples in the current study, allowing a detailed view of K–Na substitution. The Na_2O:K_2O ratios for the samples range from 0.03 to 7.55

(Table 2). Spectrally, there are a number of differences between the two compositional clusters: (1) the OH bands in the 1.4 μm region occur at longer wavelengths in natrojarosite (1.477–1.48 and 1.541–1.546 μm) than in jarosite (1.465–1.468 and 1.51–1.52 μm) (Table 8); (2) the OH combination bands in the 1.8 μm region occur at longer wavelengths in natrojarosite (1.85–1.86 μm) than jarosite (1.84–1.85 μm) (Table 9); and (3) there are differences in the wavelength positions of the major S–O fundamental bands (Tables 11–13). Some of these variations are not gradual, as in some cases, only the most Na-rich (SPT108) exhibits band positions different from other jarosite/natrojarosite spectra. Shifts in absorption band wavelength positions due to K–Na substitutions were also noted by Bishop and Murad (2005).

6.2.3. Jarosite–natrojarosite–hydronium jarosite

The relation of jarosite and natrojarosite to hydronium jarosite is more difficult to assess because absorption bands in the hydronium jarosite spectrum are generally broad and weak, and only a single sample of this mineral was included in the study. The major differences include: (1) the 0.9 μm region Fe^{3+} absorption band occurs at shorter wavelength in the hydronium jarosite (0.895 μm) than jarosite–natrojarosite (0.914–0.922 μm) (Table 3); and (2) the major ν_4 S–O bands occur at different wavelengths (14.4 μm (695 cm^{-1}) and 17.0 μm (590 cm^{-1}) versus 14.4–14.7 μm (695–690 cm^{-1}) and 16.5–16.8 μm (594–606 cm^{-1})) (Table 11).

6.2.4. Alunite–jarosite

While Al–Fe^{3+} solid solution is possible for alunite–jarosite, naturally occurring minerals show little variation from the end members (Brophy et al., 1962; Stoffregen et al., 2000). The presence of Al in alunite versus Fe^{3+} in jarosite results in numerous spectral differences, many of which have been discussed above. These include the absence of Fe^{3+} absorption bands in the alunite spectrum, and differences in the wavelength positions of OH and SO absorption bands (Tables 7–9, 11–13). These results clearly illustrate how cation substitution can affect a wide range of spectral properties, including the appearance of absorption bands associated with molecular groups adjacent to the substituted cations. Spectral variations, in this case, are due solely to variations in bond lengths as opposed to structural rearrangements.

6.2.5. Copiapite–ferricopiapite

Partial substitution of Fe^{2+} by Fe^{3+} and structural vacancies distinguish copiapite from ferricopiapite. Six samples in this group are available for comparison. Spectrally, these two minerals show few differences: Fe^{3+} band depths are generally shallower in copiapite but their wavelength positions are similar. SO and H_2O overtone and fundamental bands positions are essentially identical across the entire spectral range. Thus, there is no consistent spectral variability that can be used to reliably distinguish between these two minerals, as Fe^{3+} band depth can be affected by accessory phases and other variables.

6.2.6. Kieserite–szomolnokite

These two minerals are both framework sulfates with the same space group and differ (ideally) only in terms of major cation: Mg in kieserite and Fe^{2+} in szomolnokite. Spectrally, this cation substitution results in changes in the positions of the S–O bending and stretching fundamentals and overtone/combinations (Tables 11–13). Spectral differences below 3 μm may be attributable, at least in part, to the presence of accessory phases and other cations.

Based on these results, the effect of cation substitution is different in each case examined. Spectral differences range from minor (copiapite–ferricopiapite), where spectral differences are nearly absent, to major (alunite versus jarosite), where the wavelength position of nearly every absorption band is affected.

6.3. Effect of H_2O

The effect of H_2O content on sulfate spectra was examined by Dalton (2003) as discussed above. The current sample suite includes additional sample pairs that differ in terms of water content: gypsum–anhydrite, kieserite–hexahydrite.

6.3.1. Gypsum–anhydrite

These two minerals are composed of identical infinite tetrahedral–octahedral sheets, with gypsum containing H_2O molecules between adjacent sheets. The presence of H_2O in gypsum results in an interlayer structure different from that of anhydrite (Hawthorne et al., 2000) and leads to the appearance of H_2O-associated absorption bands. The presence of H_2O also causes changes in the wavelength positions of the major S–O absorption bands in the 8–17 μm (590–1250 cm^{-1}) region, as well as their combinations and overtones in the 4–5 μm region (Tables 11–13). This arises from the influence of adjacent H_2O molecules on S–O bond lengths.

6.3.2. Kieserite–hexahydrite

Kieserite and hexahydrite are both magnesium sulfates containing one and six H_2O molecules in their unit formulas, respectively. This leads to fundamentally different structures, providing insights into the structure-altering effects of changes in H_2O content. H_2O absorption bands in the 1.4 and 1.9 μm regions exhibit differences in wavelength positions, as expected (Table 8); these relate to associated differences in the number and wavelength positions of the H–O–H bending fundamentals in the 6 μm region (Table 7). Differences in wavelength positions are also found for the SO-fundamental, combination, and overtone bands (Tables 11–13). Differences in H_2O and SO band positions have also been noted in a more extensive series of variously hydrated magnesium sulfates (Crowley, 1991).

6.4. Spectral variability within a single mineral

A number of the sulfate minerals were represented by multiple samples from different localities, allowing us to examine whether spectral variability exists for a single sulfate mineral. Minerals for which reasonably pure duplicate samples

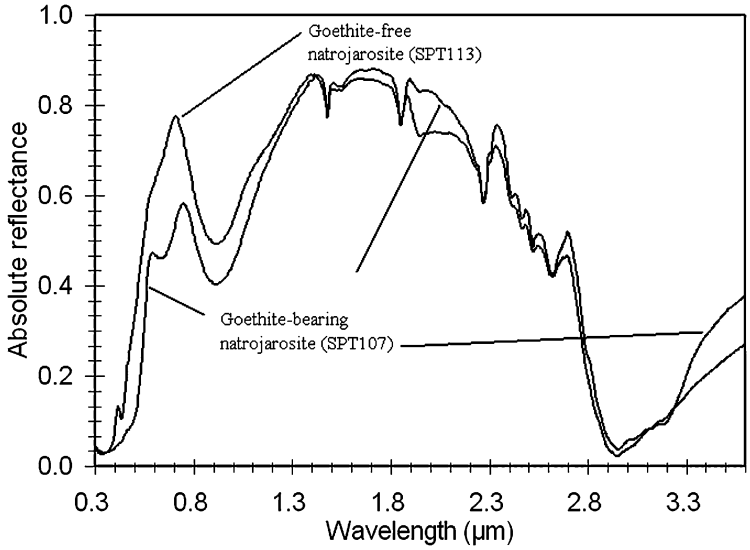

Fig. 13. Reflectance spectra (0.3–3.6 μm) of a goethite-bearing natrojarosite (SPT107) (lower spectrum in the 1 μm region), and a compositionally similar goethite-free natrojarosite (SPT113).

were available include coquimbite, ferricopiapite, jarosite, natrojarosite, pickeringite, anglesite, and barite. Duplicate spectra showed little or no difference in terms of absorption band minima wavelength positions (generally <10 nm). This arises from the fact that these minerals are not subject to extensive cation substitutions in nature, with the notable exception of the jarosite–natrojarosite series (Stoffregen et al., 2000). Spectral differences that do exist are largely confined to small variations in absorption band depths and widths. In cases where absorption features were broad and weak (e.g., 14 μm (715 cm^{-1}) region of ferricopiapite), band minima may vary by more than 10 nm, due to difficulties in reliably locating the band minimum. In the case of barite, some absorption band minima wavelength positions in the 8–16 μm (625–1250 cm^{-1}) region (e.g., band near 8.3–8.5 μm (1175–1205 cm^{-1})), showed large differences (up to 200 nm) between the sample spectra due to the appearance of strong Restrahlen bands and Christiansen features in one of the spectra. These results suggest that for sulfates in which cation substitutions and variations in structural H_2O content are minor, no significant changes in absorption band positions will occur. However, grain size effects could affect band minima determination, particularly in regions of transparency features (Conel, 1969; Mustard and Hays, 1997).

6.5. Spectrum-altering effects of accessory phases

A number of the available sulfate samples contain accessory minerals. These samples are useful for examining how these accessory phases affect sulfate spectra. The detectability of any mineral, including sulfates, will depend on a variety of factors, including grain size, the type and abundance of other phases, and physical disposition (e.g., intimate versus areal mixtures). Detectability and detection limits can be improved by focusing on wavelength regions where sulfates possess diagnostic absorption bands, such as the 4–5 μm region (Blaney, 2001).

Laboratory spectral studies of iron sulfate-bearing clays suggest that it may be difficult to detect fine-grained sulfates, such as schwertmannite, in emittance spectra because fine-grained samples result in weak emittance features (Bishop et al., 1995; Bishop and Murad, 1996) and many of schwertmannite's absorption features below ∼7 μm (>1430 cm^{-1}) are not diagnostic of this mineral. For Mars, it seems that sulfates (at the abundance levels measured by Viking and Pathfinder) are best detected in the 4–5 μm region in either loose or cemented soils, even in the presence of palagonite (Cooper and Mustard, 2002), although significant sulfate detection and discrimination has been achieved using lower wavelength data (Arvidson et al., 2005; Gendrin et al., 2005; Langevin et al., 2005). Sulfate-cemented soils also exhibit a pronounced Restrahlen band in the 8–9 μm (1110–1250 cm^{-1}) region; thus using both the 4–5 and 8–9 μm wavelength regions allows sulfate abundances and forms to be constrained. Deconvolution of TES data using sulfate-cemented soils as an end member has allowed the identification of regions on Mars where this material seems to exist (Cooper and Mustard, 2001).

Comparison of goethite-bearing (SPT107; ∼10% goethite) and goethite-free (SPT113) natrojarosite samples (Fig. 13) indicates that the spectrum-altering effects of goethite are largely confined to the 0.3–1.0 μm region. The goethite suppresses overall reflectance across this region as well as the 0.43 μm Fe^{3+} band, and introduces its own 0.65 μm absorption band. The 0.91 μm band of the natrojarosite is also affected by the goethite, because goethite also exhibits an absorption band at this wavelength; however, due to this overlap, its effect on the wavelength position of the natrojarosite band is minor. Goethite, which contains OH, also causes a broadening of the 3 μm region absorption feature. At longer wavelengths, goethite exhibits weak bands at 14.7 μm (680 cm^{-1}) and 19.6 μm (510 cm^{-1}), which are not apparent in the SPT107 spectrum. SO absorption band wavelength positions are not affected by goethite.

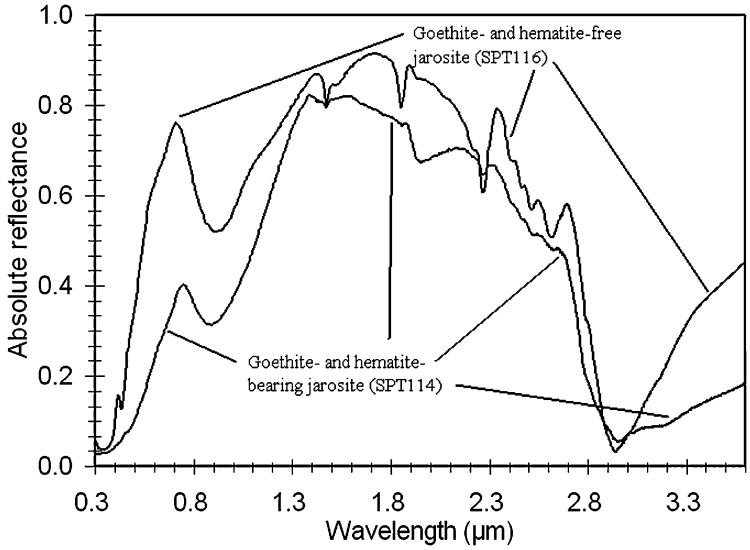

Fig. 14. Reflectance spectra (0.3–3.6 μm) of a goethite- and hematite-bearing jarosite (SPT114) (lower spectrum), and a compositionally similar goethite-free jarosite (SPT116).

Comparison of a goethite- and hematite-bearing (SPT114) to a pure (SPT116) jarosite of similar composition can be used to assess the spectrum-altering effects of both goethite and hematite on jarosite (Fig. 14). The compositional data suggests that SPT114 contains ∼10 wt% each of goethite and hematite. The presence of these two accessory minerals suppresses the 0.43 μm Fe^{3+} band, causes the 0.91 μm Fe^{3+} band to move to shorter wavelengths (0.88 versus 0.91 μm), largely attributable to the hematite, whose absorption band is located at 0.87 μm (resulting in a composite band from both the hematite and sulfate with a position intermediate between the two), widens the 3 μm absorption feature, likely causes the moderate reduction in overall reflectance beyond ∼10 μm (<1000 cm^{-1}), and introduces an absorption band near 19.5 μm (513 cm^{-1}). Once again, the spectrum-altering effects of these accessory phases are most evident in the 0.3–1.0 μm region, while the S–O fundamentals are unaffected.

In these examples and for other spectra measured for this study, most spectral features diagnostic of the presence of sulfates and useful for species discrimination, such as wavelength positions of the S–O fundamental, combination, and overtone bands and OH combination bands, are unaffected by the presence of these ferric oxides and hydroxides. This indicates that sulfate detection and species discrimination can be done in the presence of these minerals using spectral features beyond ∼1 μm, at least for the abundance levels present in the current samples. Some discrimination is also possible using features in the 1 μm region (Clark et al., 2003).

6.6. Spectral uniqueness of sulfates

This study has shown that sulfates exhibit characteristic absorption features in a number of wavelength intervals. Absorption bands in the 0.43 and 0.8–0.9 μm regions are characteristic of hydroxo-bridged Fe^{3+}. However, similar bands are also present in the spectra of some layer silicates (0.43 μm band) and a number of iron oxides/hydroxides (0.8–0.9 μm bands) (Fig. 6) (e.g., Morris et al., 2000). Similarly, weak Fe^{2+} bands located in the 0.9–1.2 μm region can be overlapped by iron oxides/hydroxides, and a number of mafic silicates (e.g., King and Ridley, 1987; Cloutis and Gaffey, 1991). The 1.4, 1.9, 3, and 6 μm regions exhibit absorption bands attributable to OH/H_2O, and while band positions can be used to distinguish different sulfates, most OH/H_2O-bearing minerals also exhibit absorption bands in these wavelength regions (e.g., Clark et al., 1990), limiting their utility for practical remote sensing on many bodies. Absorption bands in the 1.8 μm region, attributable to H–O–H and O–H stretching and bending combinations (Fig. 1), are not significantly overlapped by bands from other common minerals, and hence this wavelength region may be useful for detection and partial characterization of sulfates, particularly OH-bearing species. More generally, a broad feature in this region is characteristic of OH/H_2O-bearing sulfates. The 2.1–2.7 μm region of OH-bearing sulfates exhibits a number of absorption bands attributable to OH or SO combination vibrations (Fig. 12). However, layer silicates and carbonates also exhibit absorption bands in this region (e.g., Gaffey, 1985; Clark et al., 1990). Precise determination of band positions in this region and determination of relative band depths and widths should permit discrimination of a large number of minerals.

The 4–5 μm region exhibits absorption features due to overtones and combinations of longer wavelength S–O fundamentals. As it is not significantly overlapped by bands from common rock-forming minerals, it appears to be the most widely applicable wavelength region for sulfate detection and characterization. The 8–10 μm (1000–1250 cm^{-1}) and 14–17 μm (590–715 cm^{-1}) regions exhibit absorption bands attributable to S–O fundamentals. Sulfate absorption bands in these regions may be partly overlapped by bands from common silicates, somewhat reducing their utility (e.g., Farmer, 1974b; Crisp et al., 1990).

7. Summary and conclusions

Absorption bands attributable to transition series elements (particularly Fe^{2+} and Fe^{3+}), OH, H_2O, and SO_4 are all present in the 0.3–26 μm region. This study has also helped to clarify a number of uncertain or contentious band assignments, although absorption band assignments beyond ∼18 μm remain uncertain in many cases. Hydroxo-bridged Fe^{3+} leads to absorption bands in the 0.43, 0.5, and 0.9 μm regions. Differences in the positions of these features allows for partial discrimination of specific sulfates; however, similar absorption features occur in other common minerals, and the width of the 0.43 μm feature may be the only distinguishing characteristic. The presence of Fe^{2+} results in a usually weak absorption feature in the 0.9–1.2 μm region whose appearance may be related to ligand type. Sulfates that are both anhydrous and transition element-free are generally featureless below ∼4 μm. The presence of OH leads to the appearance of absorption bands in the 1.4 and 3 μm regions. The presence of H_2O leads to the appearance of absorption bands in the 1.4, 1.9, 3, and 6 μm regions. Consequently, OH- versus H_2O-bearing sulfates have fundamentally different spectral properties below ∼7 μm (>1430 cm^{-1}). The number and wavelength positions of absorption bands below 2.5 μm allows for discrimination of individual OH- and H_2O-bearing sulfates (Crowley et al., 2003), and is a function of the number of distinct sites available to these molecules and the degree of hydrogen bonding. Changes in H_2O content can result in structural change, and consequently significant spectral change.

SO_4 tetrahedra give rise to fundamental bending and stretching vibrations in the 7.8–10.4 μm (960–1280 cm^{-1}), 13–18 μm (555–770 cm^{-1}), and 19–24 μm (415–525 cm^{-1}) regions. Band positions are unique for a particular sulfate mineral. Combinations and overtones of H_2O or OH fundamentals can lead to absorption bands in the 1.6–1.9 and 2.1–2.7 μm intervals. The 2.1–2.7 μm region may also exhibit additional absorption bands due to SO bending overtones. Cation substitutions that lead to structural rearrangements result in significant spectral changes, and in some cases, wavelength positions of all major absorption bands are affected. Even cation substitutions that do not lead to structural changes can still cause shifts in band position due to their effects on bond lengths of adjacent molecular groups.

Group-wide spectral–compositional–structural trends, similar to those derived for some mafic silicates (e.g., Cloutis and Gaffey, 1991), could not be established. However, individual sulfate minerals can be uniquely identified on the basis of absorption band positions in a number of wavelength regions (Crowley et al., 2003; Bishop and Murad, 2005). Of the various wavelength regions attributable to sulfate-related absorptions, the 4–5 μm region is probably the best from an operational perspective, because absorption bands for the major rock-forming minerals do not appreciably affect this wavelength region. However, many planetary bodies have low reflected or thermal fluxes in this region (e.g., Europa).The spectrum-altering effects of accessory Fe oxides/hydroxides are largely confined to the 0.3–1 μm region.

Given the spectral diversity of sulfates, the availability of multiple wavelength regions in which partial or complete species discrimination is possible, and the availability of wavelength regions where sulfates exhibit features that are not overlapped by absorption bands of common rock-forming minerals, optical spectroscopy can be a powerful tool for sulfate detection and discrimination on a number of planetary bodies. Bodies on which sulfates are known, presumed, or suspected to exist, and for which spectral observational campaigns could benefit from spectral analysis in diagnostic wavelength regions, include Mars, Europa, Io, and some classes of dark asteroids.

Acknowledgments

Thanks to Dr. Jeffrey Post and the staff at the Smithsonian Institution National Museum of Natural History for providing a number of the sulfate samples. We also acknowledge the kind assistance provided by Dr. Takahiro Hiroi and Dr. Carlé Pieters for enabling access to the NASA-funded multi-user Reflectance Experiment Laboratory (RELAB) facility in the Department of Geological Sciences at Brown University for the spectral measurements. Thanks also to Mr. Neil Ball in the Department of Geological Sciences at the University of Manitoba for acquisition of the X-ray diffraction data, and Doug Goltz, Michael Guertin, Brad Russell, and Matthew Barg for their assistance with sample preparation and analysis. This study was supported by a Discovery Grant from the Natural Sciences and Engineering Research Council of Canada, and grants from the Canadian Space Agency, the University of Winnipeg, Human Resources Development Canada, and Manitoba Education, Training and Youth. Thanks to Janice Bishop and Brad Dalton for their insightful and thorough reviews and many helpful suggestions which greatly improved this paper.

References

Adler, H.H., Kerr, P.F., 1965. Variations in infrared spectra, molecular symmetry and site symmetry of sulfate minerals. Am. Mineral. 50, 132–147.

Alpers, C.N., Blowes, D.W. (Eds.), 1994. Environmental Geochemistry of Sulfide Oxidation. American Chemical Society Symposium Series, vol. 550. Mineralogical Society of America, Washington, DC, p. 681.

Arlauckas, S.M., Hurowitz, J.A., Tosca, N.J., McLennan, S.M., 2004. Iron oxide weathering in sulfuric acid: Implications for Mars. Lunar Planet. Sci. 35. Abstract 1868 [CD-ROM].

Arvidson, R.E., Poulet, F., Bibring, J.-P., Wolff, M., Gendrin, A., Morris, R.V., Freeman, J.J., Langevin, Y., Mangold, N., Bellucci, G., 2005. Spectral reflectance and morphologic correlations in eastern Terra Meridiani, Mars. Science 307, 1591–1594.

Bain, R.J., 1990. Diagenetic, nonevaporative origin for gypsum. Geology 18, 447–450.

Baird, A.K., Toulmin III, P., Clark, B.C., Rose Jr., H.J., Keil, K., Christian, R.P., Gooding, J.L., 1976. Mineralogic and petrologic implications of Viking geochemical results from Mars: Interim report. Science 194, 1288–1293.

Baker, L.L., Agenbroad, D.J., Wood, S.A., 2000. Experimental hydrothermal alteration of a martian analog basalt: Implications for martian meteorites. Meteorit. Planet. Sci. 35, 31–38.

Bandfield, J.L., 2002. Global mineral distribution on Mars. J. Geophys. Res. 107, doi:10.1029/2001JE001510.

Banin, A., Han, F.X., Kan, I., Cicelsky, A., 1997. Acidic volatiles and the Mars soil. J. Geophys. Res. 102, 13341–13356.

Bayly, J.G., Kartha, V.B., Stevens, W.H., 1963. The absorption spectra of liquid phase H_2O, HDO and D_2O from 0.7 to 10 μm. Infrared Phys. 3, 211–223.

Berkley, J.L., 1981. Mars weathering analogs: Secondary mineralization in Antarctic basalts. Proc. Lunar Sci. Conf. B 12, 1481–1492.

Bibring, J.-P., Langevin, Y., Gendrin, A., Gondet, B., Poulet, F., Berthé, M., Soufflot, A., Arvidson, R., Mangold, N., Mustard, J., Drossart, P., and the OMEGA Team, 2005. Mars surface diversity as revealed by the OMEGA/Mars Express observations. Science 307, 1576–1581.

Bigham, J.M., Schwertmann, U., Carlson, L., Murad, E., 1990. A poorly crystallized oxyhydroxysulfate of iron formed by bacterial oxidation of Fe(II) in acid mine waters. Geochim. Cosmochim. Acta 54, 2743–2758.

Bigham, J.M., Schwertmann, U., Carlson, L., 1992. Mineralogy of precipitates formed by the biochemical oxidation of Fe(II) in mine drainage. In: Skinner, H.C.W., Fitzpatrick, R.W. (Eds.), Biomineralization Processes of Iron and Manganese. In: Catena Supplements, vol. 21. Catena Verlag, Cremlingen-Destedt, Germany, pp. 219–232.

Bigham, J.M., Carlson, L., Murad, E., 1994. Schwertmannite, a new iron oxyhydroxysulfate from Pyhäsalmi, Finland, and other localities. Miner. Mag. 58, 641–648.

Bigham, J.M., Schwertmann, U., Traina, S.J., Winland, R.L., Wolf, M., 1996. Schwertmannite and the chemical modeling of iron in acid sulfate waters. Geochim. Cosmochim. Acta 60, 2111–2121.

Bishop, J.L., Murad, E., 1996. Schwertmannite in Mars? Spectroscopic analyses of schwertmannite, its relationship to other ferric minerals, and its possible presence in the surface material on Mars. In: Dyar, M.D., McCammon, C., Schaefer, M.W. (Eds.), Mineral Spectroscopy: A Tribute to Roger G Burns. Geochemical Society, London, pp. 337–358. Special Publication No. 5.

Bishop, J.L., Murad, E., 2005. The visible and infrared spectral properties of jarosite and alunite. Am. Mineral. 90, 1100–1107.

Bishop, J.L., Pieters, C.M., 1995. Low-temperature and low atmospheric pressure infrared reflectance spectroscopy of Mars soil analog materials. J. Geophys. Res. 100, 5369–5379.

Bishop, J.L., Pieters, C.M., Burns, R.G., Edwards, J.O., Mancinelli, R.L., Fröschl, H., 1995. Reflectance spectroscopy of ferric sulfate-bearing montmorillonites as Mars soil analog materials. Icarus 117, 101–119.

Bishop, J.L., Dyar, M.D., Lane, M.D., Banfield, J.F., 2005a. Spectral identification of hydrated sulfates on Mars and comparison with acidic environments on Earth. Int. J. Astrobiol. 3, 275–285.

Bishop, J.L., Schiffman, P., Lane, M.D., Dyar, M.D., 2005b. Solfataric alteration in Hawaii as a mechanism for formation of the sulfates observed on Mars by Omega and the MER instruments. Lunar Planet. Sci. 36. Abstract 1456 [CD-ROM].

Blain, C.F., Andrew, R.L., 1977. Sulfide weathering and the evaluation of gossans in mineral exploration. Miner. Sci. Eng. 9, 119–150.

Blaney, D.L., 2001. The 4.5 μm sulfate absorption feature on Mars and its relationship to formation environment. Lunar Planet. Sci. 35. Abstract 1919 [CD-ROM].

Blaney, D.L., McCord, T.B., 1995. Indications of sulfate minerals in the martian soil from Earth-based spectroscopy. J. Geophys. Res. 100, 14433–14441.

Bonello, G., Berthet, P., D'Hendecourt, L., 2005. Identification of magnesium sulfate hydration state derived from NIR reflectance spectroscopy. Lunar Planet. Sci. 36. Abstract 1996 [CD-ROM].

Brady, K.S., Bigham, J.M., Jaynes, W.F., Logan, T.J., 1986. Influence of sulfate on Fe-oxide formation: Comparisons with a stream receiving acid mine drainage. Clays Clay Miner. 34, 266–274.

Brearley, A.J., 1993. Occurrence and possible significance of rare Ti-oxides (Magnéli phases) in carbonaceous chondrite matrices. Meteoritics 28, 590–595.

Brearley, A.J., Jones, R.H., 1998. Chondritic meteorites. In: Papike, J.J. (Ed.), Planetary Materials. In: Reviews in Mineralogy, vol. 36. Mineralogical Society of America, Washington, DC. Chap. 3.

Breitinger, D.K., Krieglstein, R., Bogner, A., Schwab, R.G., Pimpl, T.H., Mohr, J., Schukow, H., 1997. Vibrational spectra of synthetic minerals of the alunite and crandallite type. J. Mol. Struct. 408–409, 287–290.

Breitinger, D.K., Schukow, H., Belz, H.-H., Mohr, J., Schwab, R.G., 1999. Two-phonon excitations in IR and NIR spectra of alunites. J. Mol. Struct. 480–481, 677–682.

Bridges, J.C., Grady, M.M., 1999. A halite–siderite–anhydrite–chlorapatite assemblage in Nakhla: Mineralogical evidence for evaporites on Mars. Meteorit. Planet. Sci. 34, 407–415.

Bridges, J.C., Grady, M.M., 2000. Evaporite mineral assemblages in the nakhlite (martian) meteorites. Earth Planet. Sci. Lett. 176, 267–279.

Brophy, G.P., Scott, E.S., Snellgrove, R.A., 1962. Sulfate studies. II. Solid solution between alunite and jarosite. Am. Mineral. 47, 112–126.

Buckby, T., Black, S., Coleman, M.L., Hodson, M.E., 2003. Fe-sulfate-rich evaporative mineral precipitates from the Rio Tinto, southwest Spain. Miner. Mag. 67, 263–278.

Buijs, K., Choppin, G.R., 1963. Near-infrared studies of the structure of water. I. Pure water. J. Chem. Phys. 39, 2035–2041.

Buijs, K., Choppin, G.R., 1964. Assignment of the near-infrared bands of water and ionic solutions. J. Chem. Phys. 40, 3120.

Bullock, M.A., Moore, J.M., Mellon, M.T., 2004. Laboratory simulations of Mars aqueous geochemistry. Icarus 170, 404–423.

Burgess, R., Wright, I.P., Pillinger, C.T., 1991. Determination of sulfur-bearing components in C1 and C2 carbonaceous chondrites by stepped combustion. Meteoritics 26, 55–64.

Burns, R.G., 1987. Ferric sulfates on Mars. Proc. Lunar Sci. Conf. 17 (2), J. Geophys. Res. 92, E570–E574.

Burns, R.G., 1988. Gossans on Mars. Proc. Lunar Sci. Conf. 18, 713–721.

Burns, R.G., 1992. Rates of oxidative weathering on the surface of Mars. In: Workshop on the Martian Surface and Atmosphere through Time, LPI Tech. Rep. 92-02, pp. 26–27.

Burns, R.G., 1993a. Rates and mechanisms of chemical weathering of ferromagnesian silicate minerals on Mars. Geochim. Cosmochim. Acta 57, 4555–4574.

Burns, R.G., 1993b. Mineralogical Applications of Crystal Field Theory, second ed. Cambridge Univ. Press, Cambridge, UK. 551 pp.

Burns, R.G., Fisher, D.S., 1990. Iron–sulfur mineralogy of Mars: Magmatic evolution and chemical weathering products. J. Geophys. Res. 95, 14415–14421.

Burns, R.G., Fisher, D.S., 1993. Rates of oxidative weathering on the surface of Mars. J. Geophys. Res. 98, 3365–3372.

Burt, D.M., Kirkland, L.E., Adams, P.M., 2004. Barite and celestine detection in the thermal infrared—Possible application to the determination of aqueous environments on Mars. Lunar Planet. Sci. 35. Abstract 2085 [CD-ROM].

Chaban, G.M., Huo, W.M., Lee, T.J., 2002. Theoretical study of infrared and Raman spectra of hydrated magnesium sulfate salts. J. Chem. Phys. 117, 2532–2537.

Chou, I.-M., Seal II, R.R., 2003. Evaporites, water, and life. I. Determination of epsomite–hexahydrite equilibria by the humidity buffer technique at 0.1 MPa with implications for phase equilibria in the system $MgSO_4$–H_2O. Astrobiology 3, 619–630.

Clark, B.C., Van Hart, D.C., 1981. The salts of Mars. Icarus 45, 370–378.

Clark, B.C., Baird, A.K., Weldon, R.J., Tsusaki, D.M., Schnabel, L., Candelaria, M.P., 1982. Chemical composition of martian fines. J. Geophys. Res. 87, 10059–10067.

Clark, R.N., 1981. Water frost and ice: The near-infrared spectral reflectance 0.65–2.5 μm. J. Geophys. Res. 86, 3087–3096.

Clark, R.N., Roush, T.L., 1984. Reflectance spectroscopy: Quantitative analysis techniques for remote sensing applications. J. Geophys. Res. 89, 6329–6340.

Clark, R.N., King, T.V.V., Klejwa, M., Swayze, G.A., 1990. High spectral resolution reflectance spectroscopy of minerals. J. Geophys. Res. 95, 12653–12680.

Clark, R.N., Swayze, G.A., Livo, K.E., Kokaly, R.F., Sutley, S.J., Dalton, J.B., McDougal, R.R., Gent, C.A., 2003. Imaging spectroscopy: Earth and planetary remote sensing with the USGS Tetracorder and expert systems. J. Geophys. Res. 108, doi:10.1029/2002JE001847.

Cloutis, E.A., Gaffey, M.J., 1991. Pyroxene spectroscopy revisited: Spectral–compositional correlations and relationship to geothermometry. J. Geophys. Res. 96, 22809–22826.

Cloutis, E.A., Sunshine, J.M., Morris, R.V., 2004. Spectral reflectance–compositional properties of spinels and chromites: Implications for planetary remote sensing and geothermometry. Meteorit. Planet. Sci. 39, 545–565.

Conel, J.E., 1969. Infrared emissivities of silicates: Experimental results and a cloudy atmosphere model of spectral emission from condensed particulate mediums. J. Geophys. Res. 74, 1614–1634.

Cooper, C.D., Mustard, J.F., 2001. TES observations of the global distribution of sulfate on Mars. Lunar Planet. Sci. 32. Abstract 2048 [CD-ROM].

Cooper, C.D., Mustard, J.F., 2002. Spectroscopy of loose and cemented sulfate-bearing soils: Implications for duricrust on Mars. Icarus 158, 42–55.

Crisp, J., Kahle, A.B., Abbott, E.A., 1990. Thermal infrared spectral character of Hawaiian basaltic glasses. J. Geophys. Res. 95, 21657–21669.

Crowley, J.K., 1991. Visible and near-infrared (0.4–2.5 μm) reflectance spectra of playa evaporite minerals. J. Geophys. Res. 96, 16231–16240.

Crowley, J.K., Hook, S.J., 1996. Mapping playa evaporite minerals and associated sediments in Death Valley, California, with multispectral thermal infrared images. J. Geophys. Res. 101, 643–660.

Crowley, J.K., Williams, D.E., Hammarstrom, J.M., Piatak, N., Chou, I.-M., Mars, J.C., 2003. Spectral reflectance properties (0.4–2.5 μm) of secondary Fe-oxide, Fe-hydroxide, and Fe-sulfate–hydrate minerals associated with sulfide-bearing mine wastes. Geochem. Explorat. Environ. Anal. 3, 219–228.

Dalton III, J.B., 2003. Spectral behavior of hydrated sulfate salts: Implications for Europa mission spectrometer design. Astrobiology 3, 771–784.

Dalton, J.B., Prieto-Ballesteros, O., Kargel, J., Jamieson, C.S., Jolivet, J., Quinn, R., 2005. Spectral comparison of heavily hydrated salts with disrupted terrains on Europa. Icarus 177, 472–490.

Dickinson, W.W., Rosen, M.R., 2003. Antarctic permafrost: An analogue for water and diagenetic minerals on Mars. Geology 31, 199–202.

Dill, H.G., 2001. The geology of aluminum phosphates and sulfates of the alunite group minerals: A review. Earth Sci. Rev. 53, 35–93.

Fang, J.H., Robinson, P.D., 1970. Crystal structures and mineral chemistry of the hydrated ferric sulfates. I. The crystal structure of coquimbite. Am. Mineral. 55, 1534–1539.

Farmer, V.C., 1974a. The layer silicates. In: Farmer, V.C. (Ed.), The Infrared Spectra of Minerals. Mineralogical Society, London, pp. 331–364.

Farmer, V.C., 1974b. Orthosilicates, pyrosilicates, and other finite-chain silicates. In: Farmer, V.C. (Ed.), The Infrared Spectra of Minerals. Mineralogical Society, London, pp. 285–303.

Feldman, W.C., Mellon, M.T., Maurice, S., Prettyman, T.H., Carey, J.W., Vaniman, D.T., Fialips, C.I., Kargel, J.S., Elphic, R.C., Funsten, H.O., Lawrence, D.J., Tokar, R.L., 2004. Contributions from hydrated states of $MgSO_4$ to the reservoir of hydrogen at equatorial latitudes on Mars. Lunar Planet. Sci. 35. Abstract 2035 [CD-ROM].

Forray, F.L., Navrotsky, A., Drouet, C., 2004. Jarosite stability on Mars. In: Second Conference on Early Mars. Abstract 8009 [CD-ROM].

Freedman, A.N., Straughan, B.P., 1971. Vibrational spectra and structures of some thiosulfate complexes. Spectrochim. Acta A 27, 1455–1465.

Gaffey, S.J., 1985. Reflectance spectroscopy in the visible and near-infrared (0.35–2.55 μm): Applications in carbonate petrology. Geology 13, 270–273.

Gaidos, E., Marion, G., 2003. Geological and geochemical legacy of a cold early Mars. J. Geophys. Res. 108, doi:10.1029/2002JE002000.

Garcia-Gonzalez, M.T., Vizcayno, C., Cortabitarte, J., 2000. Effect of kaolinite and sulfate on the formation of hydroxy-aluminum compounds. Clays Clay Miner. 48, 85–94.

Gendrin, A., Mustard, J.F., 2004. Sulfate-cemented soils detected in TES data through the application of an automatic band detection algorithm. Lunar Planet. Sci. 35. Abstract 1205 [CD-ROM].

Gendrin, A., Mangold, N., Bibring, J.-P., Langevin, Y., Gondet, B., Poulet, F., Bonello, G., Quantin, C., Mustard, J., Arvidson, R.E., LeMouélic, S., 2005. Sulfates in martian layered terrains: The OMEGA/Mars Express view. Science 307, 1587–1591.

Gibson, E.K., Wentworth, S.J., McKay, D.S., 1983. Chemical weathering and diagenesis of a cold desert soil from Wright Valley, Antarctica: An analog of martian weathering processes. Proc. Lunar Sci. Conf. 13, J. Geophys. Res. Suppl. 88, A921–A928.

Golden, D.C., Ming, D.W., Morris, R.V., 2004. Acid–sulfate vapor reactions with basaltic tephra: An analog for martian surface processes. Lunar Planet. Sci. 35. Abstract 1388 [CD-ROM].

Gooding, J.L., 1978. Chemical weathering on Mars. Thermodynamic stabilities of primary minerals (and their alteration products) from mafic igneous rocks. Icarus 33, 483–513.

Gooding, J.L., Wentworth, S.J., Zolensky, M.E., 1988. Calcium carbonate and sulfate of possible extraterrestrial origin in the EETA 79001 meteorite. Geochim. Cosmochim. Acta 52, 909–915.

Greenwood, J.P., Gilmore, M.S., Merrill, M., Blake, R.E., Martini, A.M., Varekamp, J., 2005. Jarosite mineralization in St. Lucia, WI: Preliminary geochemical, spectral, and biological investigation of a martian analogue. Lunar Planet. Sci. 36. Abstract 2348 [CD-ROM].

Grove, C.I., Hook, S.J., Paylor II, E.D., 1992. Laboratory Reflectance Spectra of 160 Minerals, 0.4 to 2.5 Microns. JPL Publ. 92-2, Pasadena, CA.

Hanel, R.A., Conrath, B.J., Hovis, W.A., Kunde, V., Lowman, P.D., Prabhakara, C., Schlachman, B., Levin, G.V., 1970. Infrared spectroscopy experiment for Mariner Mars 1971. Icarus 12, 48–62.

Hass, M., Sutherland, G.B.B.M., 1956. The infra-red spectrum and crystal structure of gypsum. Proc. R. Soc. London Ser. A 236, 427–445.

Hasenmueller, E.A., Bish, D.L., 2005. The hydration and dehydration of hydrous ferric iron sulfates. Lunar Planet. Sci. 36. Abstract 1164 [CD-ROM].

Hawthorne, F.C., Krivovichev, S.V., Burns, P.C., 2000. The crystal chemistry of sulfate minerals. In: Alpers, C.N., Jambor, J.L., Nordstrom, D.K. (Eds.), Sulfate Minerals: Crystallography, Geochemistry, and Environmental Significance. In: Reviews in Mineralogy, vol. 40. Mineralogical Society of America, Washington, DC, pp. 1–112.

He, S., Morse, J.W., 1993. The carbonic acid system and calcite solubility in aqueous Na–K–Ca–Mg–Cl–SO_4 solutions from 0 to 90 °C. Geochim. Cosmochim. Acta 57, 3533–3554.

Hladky, G., Slansky, E., 1981. Stability of alunite minerals in aqueous solutions at normal temperature and pressure. Bull. Mineral. 104, 468–477.

Hogenboom, D.L., Dougherty, A.J., Kargel, J.S., Mushi, S.E., 2005. Volumetric and optical studies of high-pressure phases of $MgSO_4$–H_2O with applications to Europa and Mars. Lunar Planet. Sci. 36. Abstract 1825 [CD-ROM].

Hovis Jr., W.A., 1966. Infrared spectral reflectance of some common minerals. Appl. Opt. 5, 245–248.

Hunt, G.R., Ashley, R.P., 1979. Spectra of altered rocks in the visible and near infrared. Econ. Geol. 74, 1613–1629.

Hunt, G.R., Salisbury, J.W., Lenhoff, C.J., 1971. Visible and near-infrared spectra of minerals and rocks. VI. Sulfides and sulfates. Mod. Geol. 3, 1–14.

Hurowitz, J.A., McLennan, S.M., Lindsley, D.H., Schoonen, M.A.A., 2005. Experimental epithermal alteration of synthetic Los Angeles meteorite: Implications for the origin of martian soils and identification of hydrothermal sites on Mars. J. Geophys. Res. 110, doi:10.1029/2004JE002391.

Jänchen, J., Bish, D.L., Mohlman, D.T.F., Stach, H., 2005. Experimental studies of the water sorption properties of Mars-relevant porous minerals and sulfates. Lunar Planet. Sci. 36. Abstract 1263 [CD-ROM].

Jeong, G.Y., Lee, B.Y., 2003. Secondary mineralogy and microtextures of weathered sulfides and manganoan carbonates in mine waste-rock dumps, with implications for heavy-metal fixation. Am. Mineral. 88, 1933–1942.

Jerz, J.K., Rimstidt, J.D., 2003. Efflorescent iron sulfate minerals: Paragenesis, relative stability, and environmental impact. Am. Mineral. 88, 1919–1932.

Kawano, M., Tomita, K., 2001. Geochemical modeling of bacterially induced mineralization of schwertmannite and jarosite in sulfuric acid spring water. Am. Mineral. 86, 1156–1165.

Khanna, R.K., Zhao, G., Ospina, M.J., Pearl, J.C., 1988. Crystalline sulfur dioxide: Crystal field splittings, absolute band intensities, and complex refractive indices derived from infra-red spectra. Spectrochim. Acta A 44, 581–586.

King, T.V.V., Clark, R.N., 1989. Spectral characteristics of chlorites and Mg-serpentines using high-resolution reflectance spectroscopy. J. Geophys. Res. 94, 13997–14008.

King, T.V.V., Ridley, W.I., 1987. Relation of the spectroscopic reflectance of olivine to mineral chemistry and some remote sensing implications. J. Geophys. Res. 92, 11457–11469.

King, P.L., Lescinsky, D.T., Nesbitt, H.W., 2005. Comparisons of predicted salt precipitation sequences with Mars Exploration Rover data. Lunar Planet. Sci. 36. Abstract 2300 [CD-ROM].

Klingelhöfer, G., Morris, R.V., Berhradt, B., Schröder, C., Rodionov, D., de Souza, P.A.J., Yen, A.S., Gellert, R., Evlanov, E.N., Zubkov, B., Foh, J., Bonnes, U., Kankeleit, E., Gütlich, P., Ming, D.W., Renz, F., Wdowiak, T.J., Squyres, S.W., Arvidson, R.E., 2004. Jarosite and hematite at Meridiani Planum from Opportunity's Mössbauer spectrometer. Science 306, 1740–1745.

Knauth, L.P., Burt, D.M., 2004. The "brine splat" hypothesis for features observed at the Opportunity landing site. In: Second Conference on Early Mars. Abstract 8047 [CD-ROM].

Lammer, H., Lichtenegger, H.I.M., Kolb, C., Ribas, I., Guinan, E.F., Abart, R., Bauer, S.J., 2003. Loss of water from Mars: Implications for the oxidation of the soil. Icarus 165, 9–25.

Lane, M.D., 2004. Thermal emission spectroscopy of sulfates: Possible hydrous iron-sulfate in the soil at the MER—A Gusev Crater landing site. Lunar Planet. Sci. 35. Abstract 1858 [CD-ROM].

Lane, M.D., Christensen, P.R., 1998. Thermal infrared emission spectroscopy of salt minerals predicted for Mars. Icarus 135, 528–536.

Lane, M.D., Dyar, M.D., Bishop, J.L., 2004. Spectroscopic evidence for hydrous iron sulfate in the martian soil. Geophys. Res. Lett. 31, doi:10.1029/2004GL021231. L19702.

Langevin, Y., Poulet, F., Bibring, J.-P., Schmitt, B., Douté, S., Gondet, B., 2005. Summer evolution of the north polar cap of Mars as observed by OMEGA/Mars Express. Science 307, 1581–1584.

Marion, G.M., Kargel, J.S., 2005. Stability of magnesium sulfate minerals in martian environments. Lunar Planet. Sci. 36. Abstract 2290 [CD-ROM].

Marion, G.M., Catling, D.C., Kargel, J.S., 2003. Modeling aqueous ferrous iron chemistry at low temperatures with applications to Mars. Geochim. Cosmochim. Acta 67, 4251–4266.

McCord, T.B., Hansen, G.B., Matson, D.L., Johnson, T.V., Crowley, J.K., Fanale, F.P., Carlson, R.W., Smythe, D.W., Martin, P.D., Hibbitts, C.A., Granahan, J.C., Ocampo, A., 1999. Hydrated salt minerals on Europa's surface from the Galileo near-infrared mapping spectrometer (NIMS) investigation. J. Geophys. Res. 104, 11827–11851.

McCord, T.B., Orlando, T.M., Teeter, G., Hansen, G.B., Sieger, M.T., Petrik, N.G., Van Keulen, L., 2001. Thermal and radiation stability of the hydrated salt minerals epsomite, mirabilite, and natron under Europa environmental conditions. J. Geophys. Res. 106, 3311–3319.

McSween Jr., H.Y., Keil, K., 2000. Mixing relationships in the martian regolith and the composition of globally homogeneous dust. Geochim. Cosmochim. Acta 64, 2155–2166.

McSween Jr., H.Y., Murchie, S.L., Crisp, J.A., Bridges, N.T., Anderson, R.C., Bell III, J.F., Britt, D.T., Brückner, J., Dreibus, G., Economou, T., Ghosh, A., Golombek, M.P., Greenwood, J.P., Johnson, J.R., Moore, H.J., Morris, R.V., Parker, T.J., Rieder, R., Singer, R., Wänke, H., 1999. Chemical, multispectral, and textural constraints on the composition and origin of rocks at the Mars Pathfinder landing site. J. Geophys. Res. 104, 8679–8715.

Mertzman, S.A., 2000. K–Ar results from the southern Oregon–northern California cascade range. Oregon Geol. 62, 99–122.

Milliken, R.E., Mustard, J.F., 2004. Determining water content of geologic materials using reflectance spectroscopy. Lunar Planet. Sci. 35. Abstract 1620 [CD-ROM].

Milliken, R.E., Mustard, J.F., 2005. A laboratory-based model for estimating absolute H_2O content of minerals using vis–NIR spectroscopy. Lunar Planet. Sci. 36. Abstract 1368 [CD-ROM].

Minenyi, S.C.B., 2000. X-ray and vibrational spectroscopy of sulfate in Earth materials. In: Alpers, C.N., Jambor, J.L., Nordstrom, D.K. (Eds.), Sulfate Minerals: Crystallography, Geochemistry, and Environmental Significance. In: Reviews in Mineralogy, vol. 40. Mineralogical Society of America, Washington, DC, pp. 113–172.

Moenke, H., 1962. Mineralspektren. Akademie-Verlag, Berlin.

Moenke, H.H.W., 1974. Vibrational spectra and the crystal-chemical classification of minerals. In: Farmer, V.C. (Ed.), The Infrared Spectra of Minerals. Mineralogical Society, London, pp. 111–118.

Moore, J.M., Bullock, M.A., 1999. Experimental studies of Mars-analog brines. J. Geophys. Res. 104, 21925–21934.

Moore, J.M., Bullock, M.A., Sharp, T.G., Quinn, R., 2005. Mars-analog evaporite experiment: Initial results. Lunar Planet. Sci. 36. Abstract 2246 [CD-ROM].

Morris Jr., R.J., 1963. Infrared spectrophotometric analysis of calcium sulfate hydrates using internally standardized mineral oil mulls. Anal. Chem. 35, 1489–1492.

Morris, R.V., Lauer Jr., H.V., Lawson, C.A., Gibson Jr., E.K., Nace, G.A., Stewart, C., 1985. Spectral and other physicochemical properties of submicron powders of hematite (a-Fe_2O_3), maghemite (γ-Fe_2O_3), magnetite (Fe_3O_4), goethite (α-FeOOH), and lepidocrocite (γ-FeOOH). J. Geophys. Res. 90, 3126–3144.

Morris, R.V., Golden, D.C., Bell III, J.F., Shelfer, T.D., Scheinost, A.C., Hinman, N.W., Furniss, G., Mertzman, S.A., Bishop, J.L., Ming, D.W., Allen, C.C., Britt, D.T., 2000. Mineralogy, composition, and alteration of Mars Pathfinder rocks and soils: Evidence from multispectral, elemental, and magnetic data on terrestrial analogue, SNC meteorite, and Pathfinder samples. J. Geophys. Res. 105, 1757–1817.

Morris, R.V., Squyres, S., Arvidson, R.E., Bell III, J.F., Christensen, P.C., Gorevan, S., Herkenhoff, H., Klingelhöfer, G., Rieder, R., Farrand, W., Ghosh, A., Glotch, T., Johnson, J.R., Lemmon, M., McSween, H.Y., Ming, D.W., Schroeder, C., de Souza, P., Wyatt, M., and the Athena Science Team, 2004. A first look at the mineralogy and geochemistry of the MER-B landing site in Meridiani Planum. Lunar Planet. Sci. 35. Abstract 2179 [CD-ROM].

Mukhin, L.M., Koscheev, A.P., Dikov, Y.P., Huth, J., Wänke, H., 1996. Experimental simulations of the photodecomposition of carbonates and sulfates on Mars. Nature 379, 141–143.

Murad, E., Rojík, P., 2003. Iron-rich precipitates in a mine drainage environment: Influence of pH on mineralogy. Am. Mineral. 88, 1915–1918.

Mustard, J.F., Hays, J.E., 1997. Effects of hyperfine particles on reflectance spectra from 0.3 to 25 μm. Icarus 125, 145–163.

Navrotsky, A., Forray, F.L., Drouet, C., 2005. Jarosite stability on Mars. Icarus 176, 250–253.

Newsom, H.E., Hagerty, J.J., Goff, F., 1999. Mixed hydrothermal fluids and the origin of the martian soil. J. Geophys. Res. 104, 8717–8728.

Nickel, E.H., Daniels, J.L., 1985. Gossans. In: Wolf, K.H. (Ed.), Handbook of Strata-Bound and Stratiform Ore Deposits. In: Regional Studies and Specific Deposits, vol. 13. Elsevier, Amsterdam, pp. 261–389.

Nordstrom, D.K., Alpers, C.N., Ptacek, C.J., Blowes, D.W., 2000. Negative pH and extremely acidic mine waters from Iron Mountain, California. Environ. Sci. Technol. 34, 254–258.

Omori, K., Kerr, P.F., 1963. Infrared studies of saline sulfate minerals. Bull. Geol. Soc. Am. 74, 709–734.

Pauli, E., Vicenzi, E.P., 2004. Sulfate mineralization in Nakhla: A cathodoluminescence and full-spectrum X-ray imaging study. Meteorit. Planet. Sci. Suppl. A 39, 82. Abstract.

Pieters, C.M., 1983. Strength of mineral absorption features in the transmitted component of near-infrared light: First results from RELAB. J. Geophys. Res. 88, 9534–9544.

Pollack, J.B., Roush, T., Witteborn, F., Bregman, J., Wooden, D., Stoker, C., Toon, O.B., Rank, D., Dalton, B., Freedman, R., 1990. Thermal emission spectra of Mars (5.4–10.5 μm): Evidence for sulfates, carbonates, and hydrates. J. Geophys. Res. 95, 14595–14627.

Powers, D.A., Rossman, G.R., Schugar, H.J., Gray, H.B., 1975. Magnetic behavior and infrared spectra of jarosite, basic iron sulfate, and their chromate analogs. J. Solid State Chem. 13, 1–13.

Rao, M.N., Wentworth, S.J., McKay, D.S., 2004. Chemical weathering records of martian soils preserved in the martian meteorite EET79001. Lunar Planet. Sci. 35. Abstract 1501 [CD-ROM].

Reichen, L.E., Fahey, J.J., 1962. An improve method for the determination of FeO in rocks and minerals including garnet. U.S. Geol. Surv. Bull. B 1144, 1–5.

Ross, S.D., 1974. Sulfates and other oxy-anions of Group VI. In: Farmer, V.C. (Ed.), The Infrared Spectra of Minerals. Mineralogical Society, London, pp. 423–444.

Rossman, G.R., 1975. Spectroscopic and magnetic studies of ferric iron hydroxy sulfates: Intensification of color in ferric iron clusters bridged by a single hydroxide ion. Am. Mineral. 60, 698–704.

Rossman, G.R., 1976a. Spectroscopic and magnetic studies of ferric iron hydroxy sulfates: The series $Fe(OH)SO_4 \cdot nH_2O$ and the jarosites. Am. Mineral. 61, 398–404.

Rossman, G.R., 1976b. The optical spectroscopic comparison of the ferric iron tetrameric clusters in amarantite and leucophosphite. Am. Mineral. 61, 933–938.

Rossman, G.R., 1996. Why hematite is red: Correlation of optical absorption intensities and magnetic moments of Fe^{3+} minerals. In: Dyar, M.D., McCammon, C., Schaefer, M.W. (Eds.), Mineral Spectroscopy: A Tribute to Roger G. Burns. Geochemical Society, London, pp. 23–27. Special Publication No. 5.

Roush, T.L., 1996. Mid-infrared (5.0–25 μm, 2000–400 cm^{-1}) optical constants of hydrous carbonate, sulfate, and nitrate. J. Geophys. Res. 101, 2215–2224.

Ryskin, Y.I., 1974. The vibrations of protons in minerals: Hydroxyl, water and ammonium. In: Farmer, V.C. (Ed.), The Infrared Spectra of Minerals. Mineralogical Society, London, pp. 137–181.

Salisbury, J.W., 1993. Mid-infrared spectroscopy: Laboratory data. In: Pieters, C.M., Englert, P.A.J. (Eds.), Remote Geochemical Analysis: Elemental and Mineralogical Composition. Cambridge Univ. Press, Cambridge, UK, pp. 79–97.

Salisbury, J.W., Walter, L.S., 1989. Thermal infrared (2.5–13.5 μm) spectroscopic remote sensing of igneous rock types on particulate planetary surfaces. J. Geophys. Res. 94, 9192–9202.

Salisbury, J.W., Walter, L.S., Vergo, N., 1987. Mid-Infrared (2.1–25 μm) Spectra of Minerals, first ed. Rep. 87-263, U.S. Geol. Surv., Reston, VA.

Sasaki, K., Taniake, O., Konno, H., 1998. Distinction of jarosite-group compounds by Raman spectroscopy. Can. Mineral. 36, 1225–1235.

Sawyer, D.J., McGehee, M.D., Canepa, J., Moore, C.B., 2000. Water soluble ions in the Nakhla martian meteorite. Meteorit. Planet. Sci. 35, 743–747.

Schubert, K.D., 1967. IR absorption of kieserite and related compounds. Bergakademia 19, 291–294.

Schugar, H.J., Rossman, G.R., Barraclough, C.G., Gray, H.B., 1972. Electronic structure of oxo-bridged iron(III) dimers. J. Am. Chem. Soc. 94, 2683–2690.

Serna, C.J., Cortina, C.P., Garcia Ramos, J.V., 1986. Infrared and Raman study of alunite–jarosite compounds. Spectrochim. Acta A 42, 729–734.

Settle, M., 1979. Formation and deposition of volcanic sulfate aerosols on Mars. J. Geophys. Res. 84, 8343–8354.

Sherman, D.M., 1985. SCF-$X\alpha$-SW MO study of Fe–O and Fe–OH chemical bonds; applications to the Mössbauer spectra and magnetochemistry of hydroxyl-bearing Fe^{3+} oxides and silicates. Phys. Chem. Miner. 12, 311–314.

Sherman, D.M., Waite, T.D., 1985. Electronic spectra of Fe^{3+} oxides and oxide hydroxides in the near IR to near UV. Am. Mineral. 70, 1262–1269.

Sherman, D.M., Burns, R.G., Burns, V.M., 1982. Spectral characteristics of the iron oxides with application to the martian bright region mineralogy. J. Geophys. Res. 87, 10169–10180.

Singh, B., Wilson, M.J., McHardy, W.J., Fraser, A.R., Merrington, G., 1999. Mineralogy and chemistry of ochre sediments from an acid mine drainage near a disused mine in Cornwall, UK. Clay Miner. 34, 301–317.

Stoffregen, R.E., Alpers, C.N., Jambor, J.L., 2000. Alunite–jarosite crystallography, thermodynamics, and geochronology. In: Alpers, C.N., Jambor, J.L., Nordstrom, D.K. (Eds.), Sulfate Minerals: Crystallography, Geochemistry, and Environmental Significance. In: Reviews in Mineralogy, vol. 40. Mineralogical Society of America, Washington, DC, pp. 454–479.

Thomas, M.R., Scheraga, H.A., Schrier, E.E., 1965. A near-infrared study of hydrogen bonding in water and deuterium oxide. J. Phys. Chem. 69, 3722–3726.

Thompson, J.B., Ferris, F.G., 1990. Cyanobacterial precipitation of gypsum, calcite, and magnesite from natural alkaline lake water. Geology 18, 995–998.

Tosca, N.J., McLennan, S.M., Lindsley, D.H., Schoonen, M.A.A., 2004. Acid–sulfate weathering of synthetic martian basalt: The acid fog model revisited. J. Geophys. Res. 109, doi:10.1029/2003JE002218.

Tosca, N.J., McLennan, S.M., Clark, B.C., Grotzinger, J.P., Hurowitz, J.A., Joliff, B.L., Knoll, A.H., Schroder, C., Squyres, S.W., and the Athena Science Team, 2005. Geochemical modeling of evaporites on Mars: Insights from Meridiani Planum. Lunar Planet. Sci. 36. Abstract 1724 [CD-ROM].

Townsend, T.E., 1987. Discrimination of iron alteration minerals in visible and near-infrared reflectance data. J. Geophys. Res. 92, 1441–1454.

Vaniman, D.T., Chipera, S.J., Bish, D.L., Carey, J.W., Fialips, C.I., Feldman, W.C., 2004a. Sulfate salts, regolith interactions, and water storage in equatorial martian regolith. Lunar Planet. Sci. 35. Abstract 1690 [CD-ROM].

Vaniman, D.T., Bish, D.L., Chipera, S.J., Fialips, C.I., Carey, J.W., Feldman, W.C., 2004b. Magnesium sulfate salts and the history of water on Mars. Nature 431, 663–665.

Vaniman, D.T., Chipera, J.S., Bish, D.L., Carey, J.W., Feldman, W.C., 2005. Martian relevance of dehydration and rehydration in the Mg-sulfate system. Lunar Planet. Sci. 36. Abstract 1486 [CD-ROM].

Vassallo, A.M., Finnie, K.S., 1992. Infrared emission spectroscopy of some sulfate minerals. Appl. Spectrosc. 46, 1477–1482.

Vilas, F., Hatch, E.C., Larson, S.M., Sawyer, S.R., Gaffey, M.J., 1993. Ferric iron in primitive asteroids: A 0.43-μm absorption feature. Icarus 102, 225–231.

Wentworth, S.J., Thomas-Keprta, K.L., McKay, D.S., 2002. Water on Mars: Petrographic evidence. Lunar Planet. Sci. 33. Abstract 1932 [CD-ROM].

Yamatera, H., Fitzpatrick, B., Gordon, G., 1964. Near-infrared spectra of water and aqueous solutions. J. Mol. Spectrosc. 14, 268–278.